ANALYTICAL MODELLING OF LASER REPAIR OF SINGLE CRYSTAL NICKEL BASED SUPERALLOYS

A thesis submitted to
The University of Birmingham
For the degree of
MASTER OF PHILOSOPHY

By

TAO TAO

School of Metallurgy and Materials
The University of Birmingham
October 2012

Table of content

Abstract

Single crystal nickel-base superalloys have been used extensively in gas turbine engines, such as blades and vanes, due to a combination of high-temperature strength, ductility and creep resistance. Even though modern gas turbines are extremely reliable, it is unavoidable to see wear and some types of damage, in particular under severe thermal and corrosive conditions. Replacement costs of gas turbine engine components are so high that it makes the repair of damaged components extremely desirable. However, experimental understanding is considered to be time and cost consuming. It follows that developing simulation methods is of necessity to aid in repairing and/or reshaping damaged gas turbine engines. In this project, models have been developed for the repair of commercial single crystal superalloys, *i.e.* CMSX-4, the main concern is put on the simulation process of heat and mass transfer, so that the relationship of laser, powder injection and substrate has been studied and predicted; moreover, the processing parameters and the correlation between solidification conditions and microstructure have been established using a columnar to epitaxial transition model so that it can be optimized for the operating conditions to generate epitaxial growth onto the single crystal substrate; these are potentially useful for further experimental validation. Additional objectives of the research were to characterize the effect of the processing parameters on (1) the thermal behaviors, (2) the mass transfer process, and (3) the complicated interaction between them.

Declaration

I hereby declare that this thesis has been composed by myself, and has not been accepted, in full or part, in any previous application for a higher degree. The work of this thesis is a record of my own work; any collaborative work has been specifically acknowledged, as have all sources of information.

Tao Tao

Acknowledgements

Firstly, I would like to express my sincere gratitude to my project supervisors, Prof. Paul. Bowen and Prof. Roger. C. Reed, for providing me with the funding and opportunity to carry out this research work. I am also very grateful for their invaluable comments, advice and guidance throughout this whole research project.

I would like to extend my deepest appreciation to my project co-supervisor, Prof. Xinhua. Wu, Dr. Daniel Clark, and Dr. Mark Ward for their valuable advice, guidance and discussion throughout the entire project.

I would also like to specially thank Dr. Jean-Christophe Gebelin who contributes quite a lot in the initial plan and analytical simulation of this project.

I would like to gratefully acknowledge, Dr. Ravi Aswathanarayana Swamy, Dr. Nils Warnken, Dr. Nick Wain, Dr.Yu-Pei Lin, Mrs Lakshmi Lavanya Parimi, Mr Jianglin Huang, Mr Libin Yang, Mr Hang Wang, Mr Chinnapat Panwisawas, Mr Zhailing Zhu, Mr Edvardo Trejo and all the other laboratory researchers and staffs of PRISM^2 for all their help and friendship.

Finally, I am also grateful to my colleagues and friends in the School of Metallurgy and Materials and Interdisciplinary Research Centre (IRC) in Materials Processing, who made my postgraduate study memorable and enjoyable.

Last, but not least, I simply could not have come this far without love, understanding, patience and inspiration from my parents, Aimei Zhang and Chuanbo Tao.

Chapter 1 Introduction

1.1 The Gas turbine engine

Gas turbines are specifically designed to convert chemical energy to mechanical energy, of which a number of applications have been found such as in aeroengine and power generation industry. The modern gas turbine engine is essentially made up of three main sections: the compressor, the combustion chamber and the turbine, see in Figure 1. The compressor is used to drive air into the combustion chamber of the engine where the temperature can reach up to 700 ℃ after the air is mechanically compressed. Following this, the air is mixed with fuel and burnt in the combustion chamber at temperature of >2000 ℃ [1].

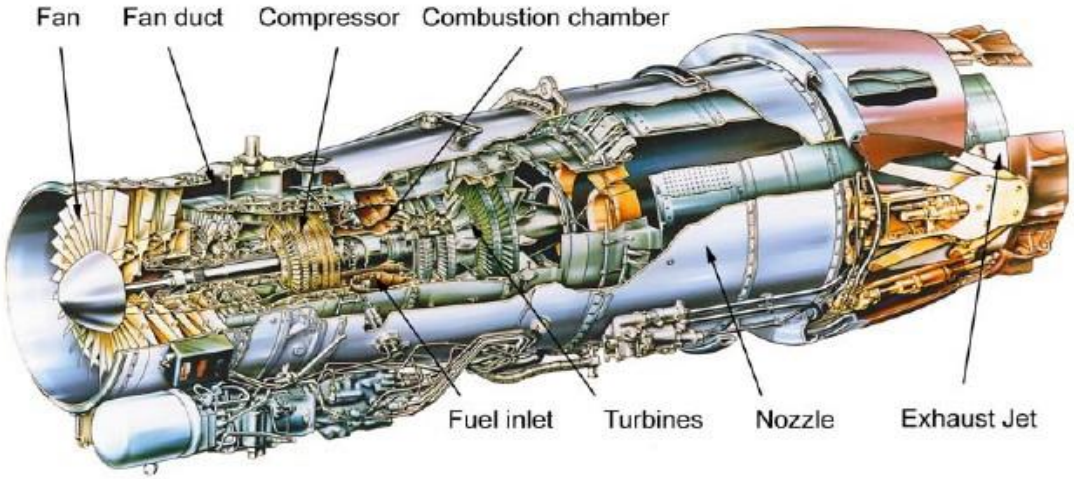

Figure 1 – A cross-sectional view of RB199 Rolls-Royce Jet engine, which powers the Tornado. The location of the compressors, the combustion system and the turbines is shown.

The heat produced by the internal combustion expands the air and spins the turbine, which extracts the power to drive the rotating turbine blades in the hottest section of engine to turn the turbine discs and hence the shaft in order to produce thrust. And for large commercial aircraft, *e.g.* Boeing 777, the latest generation of turbine engines (RR Trent 800, GE 90) have to provide thrusts of more than 100 000lb leading to the operating temperatures of up to 800◦C; under these severe working conditions, a number of factors need to be considered for the material selection, including

mechanical strength, resistance to creep, fatigue, oxidation and corrosion, in order to maintain the service life of the turbine engine. Nowadays nickel-based superalloys are extensively used in hot section components of the aeroengine, due to their unique properties and excellent performance under elevated temperature. However, the requirements for these components are very different and therefore different chemical compositions and processing routes are required. For instance, as the turbine blades, as shown in Figure 2, are located in the hottest part of the engine, and can rotate at speeds of up to 15000 rpm, they need to be creep resistant. This has been achieved by the advances in single crystal technology, where a blade can be grown with no grain boundaries [2]. This is accomplished by the use of a grain selector at the base of the casting mound of the blade. Discs, on the other hand, need to be resistant to high temperature fatigue, requiring a fine grain structure; these alloys are, therefore, processed via a wrought route [3]. Nevertheless, superalloy technology has become more advanced over the last 20 years, but the efforts to explore and develop new generation of superalloy and processes will never stop, as demand for materials to make aeroengines more efficient has always increased.

Figure 2 – Blade used in modern turbine engines using single crystal technology.

1.2 Nickel-based Superalloys

1.2.1 Alloy development

Nickel-based superalloys have been extensively used in various industrial applications since the beginning of the 1920s. Their emergence can be dated back to the development of austenitic stainless steel for high temperature usage [3]. In 1929, the development of a structural strengthening mechanism was mentioned based on aluminium and titanium for the first time. The understanding of the precise mechanism responsible for this strengthening due to precipitation hardening was confirmed by Beford and Pilling; thus a new alloy with considerable improvement of creep strength was developed; this is considered to be the beginning of nickel-based superalloys, which experienced a rapid development over the next few years due to the great amount of need from industrial gas turbines [4]. In 1957, Westbrook discovered the highly unusual property of the coherent phase γ' with increasing temperature (under 700 ℃). Further developments were mainly focused on increasing volume fraction of the γ’ phase by adding γ' forming elements, for example Al, Ti and Ta contents together with other strengthening elements. Later, some refractory metal additions, such as Mo, W and Re were also used in superalloys to provide additional strengthening through solid-solution and carbide formation. B and Ca were added to form carbides and borides for grain-boundary strengthening. A breakthrough occurred in the mid-1970s, when single crystal technology appeared by removing grain boundary strengtheners (Br, Zr, C and Hf), instead, Re and Ru gradually take a greater role. This permitted a higher solution temperature and the development of heat treatments leading to increased contents of γ’ (as high as 70%). This major chemical modification compared with polycrystalline materials led to the optimisation of the mechanical properties, especially creep resistance. In the meantime, the Fe content was progressively decreased. On the other hand, the processing techniques for superalloys also made great progress with the development of chemical composition[5], since modifications of the composition greatly influenced the

manufacturing processes and hence furthered the development of new production using new and innovative processing techniques. In the early days, superalloy parts were always made with the conventional cast and wrought routes, which were widely used for other alloy systems. Later, the investment casting technique was developed and gradually used to fabricate complicated parts of superalloys. In the 1950s, vacuum melting technology including vacuum induction melting (VIM) and vacuum arc remelting (VAR) became commercially available to manufacturers which was considered to be a great breakthrough for producing high strength superalloys since these techniques enable the elimination of detrimental elements and the addition of the reactive elements used for precipitation strengthening of alloys. Another major step was realized in the 1960s, when Versnyder and Guard, from Pratt and Whitney, developed a directional solidification casting method and demonstrated the possibility of casting complex designs consisting of a single grain. However, the first single-crystal superalloys using this technique, MAR-M200 and MAR-M247, did not show significant improvement compared with columnar grains materials obtained using directional solidification. Almost at the same time as the beginning of directional solidification, for those superalloys used in a microstructure of polycrystalline form, *e.g.* turbine discs in aeroengines, oxide dispersion strengthening (ODS) was introduced in production, which led to a change in the processing route for some high performance superalloys, *i.e.* the conventional cast and wrought -route, to powder metallurgy. Therefore the development created between advanced casting techniques and new alloy design has led to tremendous improvements in terms of the performance of gas turbine blades and vanes. Nowadays, single crystal superalloys are extensively applied in high-temperature turbine engines owing to their excellent creep resistance and thermal fatigue resistant performance. However, in spite of the cost, directionally solidified (DS) and single crystal (SX) cast turbine blades and vanes are preferred to equiaxed components. Figure 3 gives a historical view of the advancements of alloys and process for turbine blades over the last 60 years. The data describe the highest temperature for each alloy at which rupture occurs in no less than 1000h under a stress of 137 MPa; and obviously directional solidification of

single-crystal superalloys is preferred in this application in recent years. Another active direction in the processing of superalloys is in the coating techniques. In fact, the means to ensure coatings having proper and stable performance during service is a critical issue in the modern gas turbine field. Without the protection of these coatings, the components in the combustor and turbine sections would degrade very quickly due to the extreme operation conditions there. There are several coating techniques available for superalloys: diffusion coating overlay coating, thermal barrier coating [6].

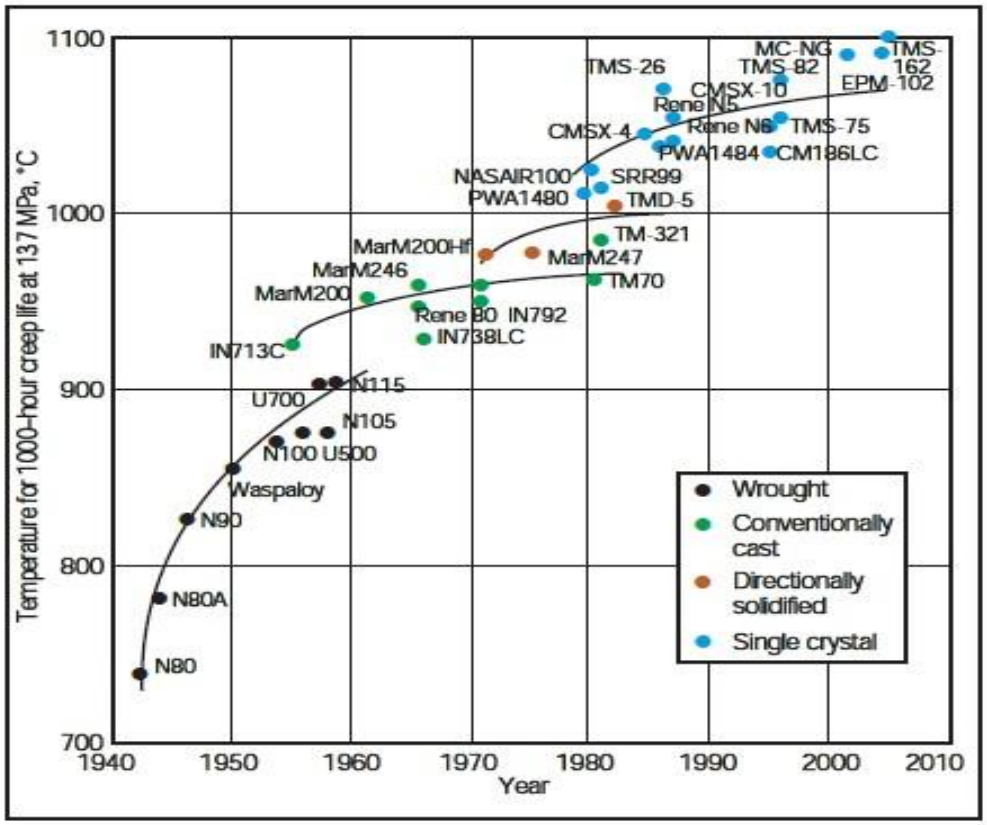

Figure 3 – Evolution of the high-temperature performance of superalloys during the past 60 years since their emergence in the 1940s [3].

1.2.2 Chemical composition

A wide range of nickel-based superalloys exist today containing up to 10 or more alloying elements. The chemical compositions used in the first generation and second generation are listed in Table 1 and Table 2 respectively. Obviously a number of elements are added to nickel and can play a different role, for example, γ' formers (Al,

Ti, Ta, Nb and V) impart strengthening *via* the Ni_3(Al, Ti, Ta) phase which is regarded as γ', the solid solution strengthening elements (Re, W, Mo, Co, Cr, Ta) enhance creep resistance, and Al, Cr and Co improve resistance to oxidation and corrosion by forming a stable oxide layer [7]. The development of second generation alloys is characterized by increasing the W content and adding Re, *i.e.* refractory metal content, which are used to provide solution strengthening and decrease the diffusion rate of the other alloying elements. Among all the second generation nickel-based single crystal superalloys, CMSX-4 is considered to be one of the most successful and is widely used in aeroengines, for the hottest section, to provide high temperature performance, improved hot section stability and lower life cycle costs. The composition of CMSX-4 can be found in Table 2. Its solidus and liquidus temperatures are 1386 ℃ and 1455 ℃ respectively. According to some previous industrial gas turbine airfoil application experience, CMSX-4 is mainly characterised by ultra-high strength, creep resistance at elevated temperature, improved hot corrosion resistance, good single crystal castability - similar to CMSX-2 and CMSX-3, as well as excellent phase stability.

Alloy	Cr	Co	Mo	W	Al	Ti	Ta	Nb	V	**Ni**	Density (g/cm^3)
CMSX-2	8	4.6	0.6	8	5.6	1	6	-	-	**bal**	8.6
PWA 1480	10	5	-	4	5	1.5	12	-	-	**bal**	8.7
RR 2000	10	15	3	-	5.5	4	-	-	1	**bal**	7.8
René N4	9	5	2	6	3.7	4.2	4	0.5	-	**bal**	8.5

Table 1 - Chemical compositions (wt. %) of first generation Ni-based superalloys for single crystal blades.

Alloy	Cr	Co	Mo	Re	W	Al	Ti	Ta	Hf	**Ni**	Density (g/cm^3)
CMSX-4	6.5	9	0.6	3	6	5.6	1	6.5	0.1	**bal**	8.70
PWA 1484	5	10	2	3	6	5.6	-	8.7	0.1	**bal**	8.95
René N5	7	8	2	3	5	6.2	-	7	0.2	**bal**	8.70
MC2	8	5	2	-	8	5	1.5	6	-	**bal**	8.63

Table 2 - Chemical compositions (wt. %) of second generation Ni-based superalloys for single crystal blades.

1.2.3 Microstructure and properties

The high temperature properties of Ni-based superalloys are closely related with the characteristics in their microstructures. The γ matrix of nickel-based superalloys, an austenite *fcc* phase, contains a high fraction of solid solution elements (mostly Co, Cr, Mo and W). The precipitate, γ' is a stable intermetallic compound formed by an ordering reaction from the γ matrix, which makes it coherent with the γ matrix. This coherence between the matrix and precipitate is generally believed to be responsible for their obvious strengthening effects in superalloys. The γ' phase possesses a *L12* structure, which is similar to the *fcc* matrix, but has Al or Ti substituting for the nickel atoms at the cube corners, see Figure 4. Its dramatic improvement of strength at elevated temperature is the most important reason for superalloys to maintain their strength under high temperature [8]. Even though it may not be possible to explain the properties of the nickel-based superalloys by just one mechanism, precipitate hardening (mainly by γ') plays an important role in terms of strengthening the nickel-based superalloys; moreover, the existence of the grains and the orientation of these grains, as well as the presence of the solid solution strengthening elements and other precipitates such as carbides and borides also have effects. In addition, other factors such as coherence with the γ matrix, antiphase boundary energy, volume fraction, size and distribution all have a role [3]. Since there is large number of alloying elements present in nickel-based superalloys, they are hardly thermodynamically stable. Therefore, in the long term, topologically close packed (TCP) phases can form; these phases tend to be both hard and brittle, and are generally undesirable as they promote crack initiation and growth. Cr and Mo as well as refractory elements such as Re can promote the formation of these phases [3,9]; PHACOMP [10] and *Md* electron [11] methods have been proven to have predictive capability to avoid TCP precipitation.

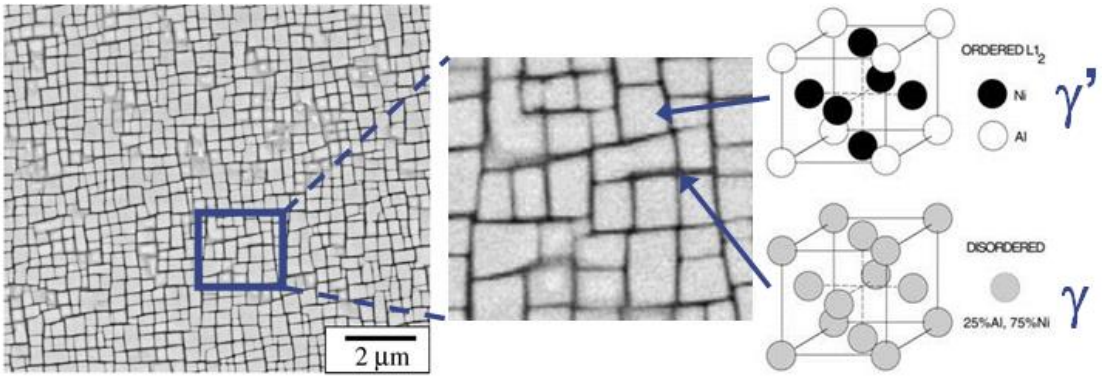

Figure 4 - Scanning electron micrograph of the γ/ γ' microstructure of the CMSX-4 superalloy [3].

1.2.4 Summary

The previous discussion in this study confirms that, since the 1920s when the age of nickel-based superalloys began, superalloy technology has made great progress, due to the increased demand of material to make the turbine engine more efficient; these are represented by the huge improvement of the physical and chemical factors which govern their performance. Blades and discs for turbine engines are two typical applications for nickel-based superalloys. In terms of turbine blades, the new generation single-crystal nickel-based superalloys have been designed to be more creep resistant with the addition of Re and Ru, as well as the development of more advanced processing routes, particularly vacuum melting, directional solidification and investment casting. On the other hand, turbine discs, in the form of polycrystalline superalloy, are always processed through a wrought route. Furthermore, it is more common for coating technologies to be adopted to protect the turbine sections from degradation under extreme operation conditions. Even though remarkable success of this class of the material has been achieved, it seems to be the case that the nickel-based superalloys are not fully mature, particularly the critical questions about the metallurgical factors, *e.g.* the effect of Ru in imparting performance. Thus, metallurgists still face significant challenges for the physical and chemical development of nickel-based superalloys.

1.3 Repair engineering

In spite of the extreme reliability of modern gas turbines, wear and some other types of damage, such as blade tip erosion and thermal fatigue cracks to components, are unavoidable. In addition, it is extremely desirable to repair and reshape damaged components due to the expensive replacement costs of gas turbine engine components. As no grain boundary strengtheners are present in the single crystal superalloys, the repair and reshaping technique must ensure a single crystal microstructure of the deposited material. Several welding techniques [12], *e.g.* electron beam and pulsed laser beam welding, are traditionally used for repair applications. However, it has been found in the investigations of David *et al.* [13] that fusion welding processes are not necessarily appropriate for the repair of single crystal superalloys due to the proneness to stray grain formation. Following this, high intensity laser beams started to be used to fabricate three-dimensional near net shape components *via* metallic powder injection in 1979 by the United Technology Research Centre [14], followed by a number of further developments [15-24]. This technique was first introduced for the repair of gas turbine blade in the aeroengine industry in late 1990s, and it has been recently shown that single crystal deposition is possible by an Epitaxial Laser Metal Forming (E-LMF) technique [25], in which process a stream of powders is injected into a laser induced molten pool generating epitaxially a single crystal part onto the damaged component by careful processing control. Nowadays efforts are made by a number of researchers and organizations for the improvement of LMF, and it can be expected that there will be widespread use of this technique for the industrial repair engineering in the near future.

1.4 Project objectives

Our current understanding is considered to be insufficient for the optimisation of processing control for the E-LMF process which includes a number of parameters which strongly influence the quality of the repaired part. For better understanding of the characteristics of the repaired products, the processing parameters need to be optimized. Experimental work is always considered as an effective way, but most of the time it is still cost consuming. Consequently, developing theoretical methods is of necessity to aid better understanding. Therefore the main objective of this project is to build up fundamental analytical models for the laser repair process of the extensively used single crystal superalloy CMSX-4. Firstly, some concern will be put on characterization of mass transfer, which involves absorption of powder particles, power attenuation as well as laser-powder interaction. In the meantime, the main emphasis will be to quantify the heat transfer so that a heat source model can be derived to accurately describe the temperature evolution, distribution within the substrate and ultimately the dimensions of melt pool. Then coupled with the microstructure modeling, the solidification conditions will be determined for the prediction of the generated material microstructure to see if a successful repair can be achieved; thus the processing parameters and the ultimate microstructure can be connected which is of great use for experimental validation and in return optimizing and developing the model. In addition, the influence of the processing parameters during the process will be demonstrated and discussed analytically so that the models proposed in this work should aid better understanding of laser repair processes and have the potential for optimising the process parameters. Ultimately following this work, a fundamental model should be able to predict layer geometries, thermal fields involved as well as the microstructure produced during the repair process.

Chapter 2 Background

2.1 Laser processing

2.1.1 Overview

Laser metal forming (LMF), also known as direct metal deposition (DMD) or laser manufacturing process (LMP) or sometimes laser engineered net shaping (LENS), is a laser cladding-based technique which has been used extensively during the last decade for surface coating, rapid prototyping and innovative alloying in industrial manufacturing [26-28]. This method can be used to fabricate and restore 3D near net shape components via metal powder injection, see Figure 7. Some unique advantages are found for the components fabricated using this technique, such as a high precision, small heat affected zone, good surface quality, the generation of a dense microstructure which is free of pores, as well as significant time and cost savings [29]. This technique is being introduced for commercial manufacturing of superalloys due to its potential for repair and reshaping of locally damaged or worn parts in gas turbine components. Since these components, *i.e.* typically turbine blades and vanes, are exposed to the most severe mechanical and thermal loading, the single crystal microstructure of the repaired part must be maintained epitaxially during the process; this is Epitaxial Laser Metal Forming [30]. This method is potentially feasible due to the very localised laser heating resulting in large temperature gradients. On the one hand, this gives rise to high residual stresses and deformations; this may potentially influence the service behavior of the substrate; on the other hand, the thermal gradient needs to be steep enough for the avoidance of the columnar-to-equiaxed transition (CET) so that epitaxial single crystal repair can be achieved [31].

2.1.2 Repair process

During the LMF process, a melt pool, induced by a laser beam with high intensity, is locally formed on the substrate and at the same time a stream of powder particles is injected into the laser-induced molten pool. After a certain interaction time, the molten pool solidifies and hence generates a deposit on the damaged component; subsequent layers are then built on top of the previous one leading to a three-dimensional build-up. As a thin layer of the substrate is sufficiently remelted, a well-bonded boundary is achieved. If the nucleation and growth of equiaxed grains is completely avoided by a precise control, there is an epitaxial growth for the repaired part onto the substrate in a columnar growth regime, *i.e.* a deposit is produced epitaxially onto a single crystal substrate, so that the damaged components can be repaired [32]; Figure 6 presents the 2D repair process considered in this study. E-LMF is essentially a very complicated fusion and solidification process due to the number of process variables: laser power, beam velocity, powder feeding rate, beam diameter and energy density distribution of laser beam, amount and sort of shielding and carrier gas, material properties, height increment per layer, as well as characteristics of powder particles (distribution of particle size and particle shape [33]. These produce a number of interactions between each other (laser beam, powder stream, the substrate and molten pool) and physical phenomena (laser-powder interaction, heat transfer, fusion, fluid flow and solidification). It follows that theoretical study and understanding of the relationship between the processing parameters and the ultimate geometric sizes of layers and the resulting material microstructure are key to achieving a high-quality repaired part with the desired microstructure, dimensional accuracy and to optimise the process in return [34,35].

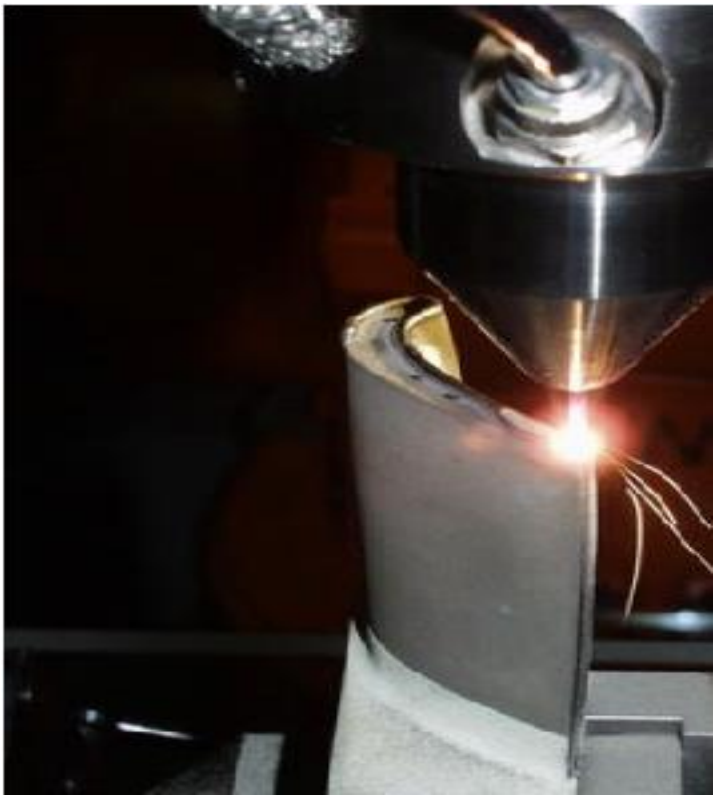

Figure 5 – Illustration of laser repair of blade tip.

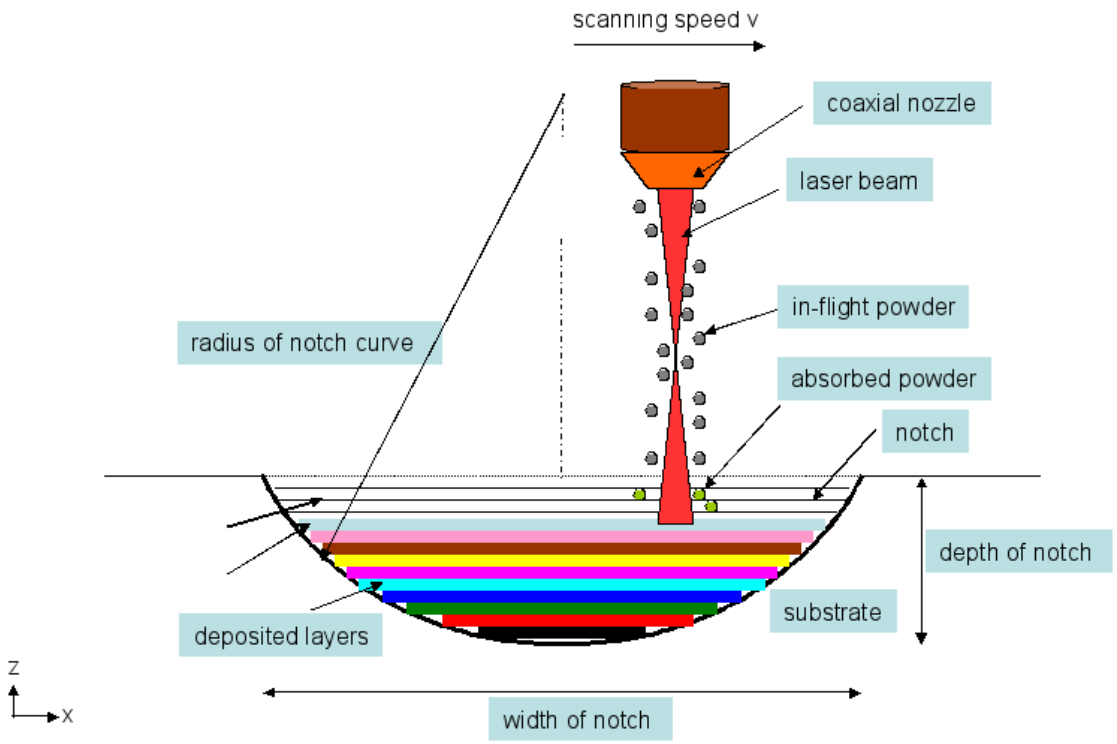

Figure 6 – Schematic illustration of 2D laser repair process considered in this study.

2.2 Process models

2.2.1 Overview

Given the great number of parameters present in the LMF process, a comprehensive experimental investigation is regarded as an inefficient method for improvement of processing control. Therefore, modelling tools in many cases are the best way to obtain the necessary information on the laser treatment process. Since the solidification conditions within the melt pool mainly determine the nature of the solidified region, simulation of the interaction between laser beam and the substrate is useful to provide information concerning parameters such as the melt pool cooling rate, temperature gradient and growth rate. And a number of authors [36-38] make some contributions for the understanding of process control of laser processing in the liquid state through the evaluation and the impact of operating conditions on the pool shape, temperature, and fluid flow. For example, Hoadley and Rappaz presented a 2D steady state thermal analysis for the calculation of the molten pool shape and for the evaluation of the influence of processing parameters on the clad thickness [39]. Ollier *et al.* annalysed melt pool convection and angle dependence on power absorption, using 2D heat flux calculations [40]. Despite considerable development in the understanding of phenomena encountered during the process, it is still worth noting that in many instances complex numerical calculations are of little help for subsequent process optimization [41]. To further optimise modelling results, experimental work was carried out by various authors, including the influence of the operating conditions on the characteristics of the clad, process monitoring, metallurgical and microstructure analyses and characterization. In terms of the impact of the processing parameters on the clad characteristics, the following studies should be mentioned. Ro ósz [42] measured the interface velocity as a function of the size of the melt pool and studied how the structure of the resolidified region varies with beam velocity. El-Batahgy [43] analysed the way that welding parameters influence the fusion zone shape. Kim [44] modelled the melt pool obtained during laser cladding by a time

dependent Finite Element Method (FEM). In this study, molten pool shapes at different cladding stages were estimated and further assessed through experiments on laser deposition process with wire feeding. The influences of deposition time and deposition speed on molten pool shape were investigated. Moreover, a number of authors have examined process control through the development and study of methods for in-situ measurment and process monitoring. Shanwald [45] used an optical method for the mass feed rate measurement. Griffith [46] showed that the understanding of the temperature variation is key for producing dependable and repeatable deposits during the LMF process and demonstrated that it was possible for feedback control using these thermal analyses. Also there is some previous work dealing with microstructure analysis for process control. For instance, Lim [47] observed the microstructures of the clad layers as a function of the powder feed rate and the beam velocity. Mohanty [48] analysed the way that flow instability affects the ultimate microstructure during laser beam interaction. Further detailed background investigation regarding the models of the major physical phenomena encountered during the LMF process is presented in the following section.

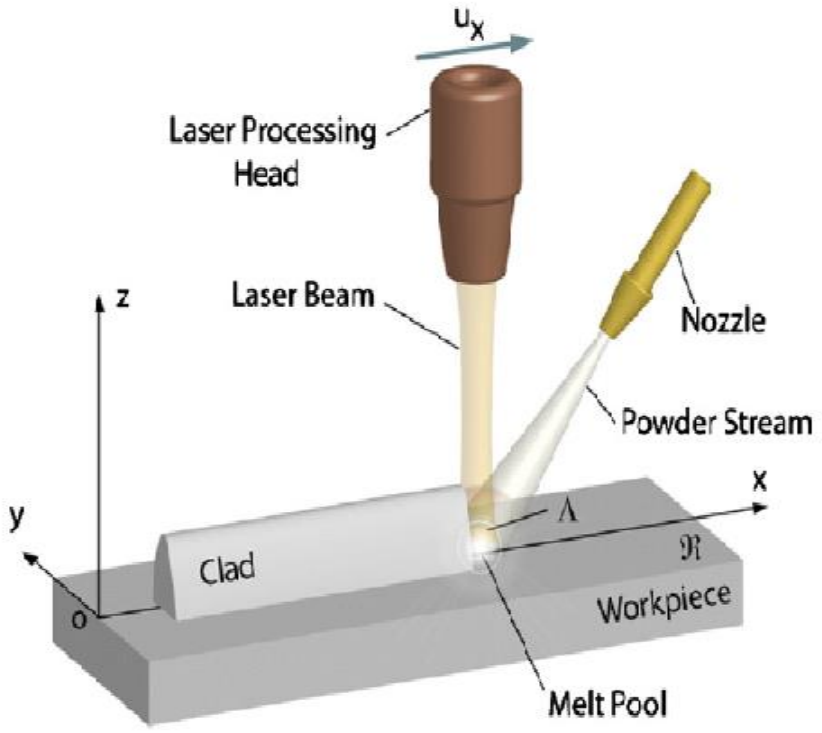

Figure 7 – 3D illustration of laser metal forming process.

2.2.2 Solidification and microstructure

Liu *et al* [49] carried out interesting work on the fabricability of single crystal superalloys. Their results indicated that the processing parameters had a strong influence on the formation of equiaxed grains and the solidification cracks. Therefore the processing parameters should be derived quantitively for generating single crystal deposits which are free of equiaxed grains and cracks. Mokadem *et al* [50] mentioned that specific solidification conditions are necessary for the reshaping of gas turbine blades in order for the prevention of the generation of new grains in front of the epitaxial columnar dendrites. The conditions for nucleation and growth of equiaxed grains ahead of the onward solidification front have been solved analytically by Hunt *et al* [51] and Gaumann *et al* [52], according to whom, a parameter $\emptyset$ is defined as a fraction of newly nucleated grains. It follows that critical conditions are estimated referring to fully equiaxed growth with the single crystal structure of the base body being entirely substituted and the fully columnar condition respectively. On the basis of this work, Gaumann *et al* [53] derived a standard for the CET (columnar to equiaxed transition), where $\emptyset$ was plotted as a function of temperature gradient G and solidification velocity V. It was proven that a fully columnar epitaxial growth structure is achieved as long as the requirement of critical CET conditions is achieved; see the CET curve in Figure 8. However, since these analytical models neglect the effects on the growth morphology of the crystallographic orientation of the grains relating to the local heat-flow direction, the phenomenon of grain selection cannot be analysed using these models. Therefore some numerical models have been developed to predict grain growth and microstructure transitions, which allow the nucleation and growth of each grain to be simulated. And one of the most representative jobs was done by Rappaz and Gandin [54], who developed a new model with the cellular automaton (*CA*) technique. This model was further developed and coupled with finite element modeling (*FEM*) for the solution of the energy conservation equation, known as *CAFE* model. This allows a direct 2D macrograph of the grain structure to be made, which was used to simulate the CET. On the basis of experimental observations,

nucleation parameters were finely tuned to fit the position of the CET, with good agreement. Vandyoussefi and Greer [55] used the *CAFE* model to study grain refinement in the directional solidification of Al-Mg alloys. The *CAFE* model successfully simulated the formation of equiaxed grain structures and confirmed the essential features of the Hunt model for the CET. Moreover, this work showed the influence of refiner addition levels, solidification velocity and thermal gradient on the grain size.

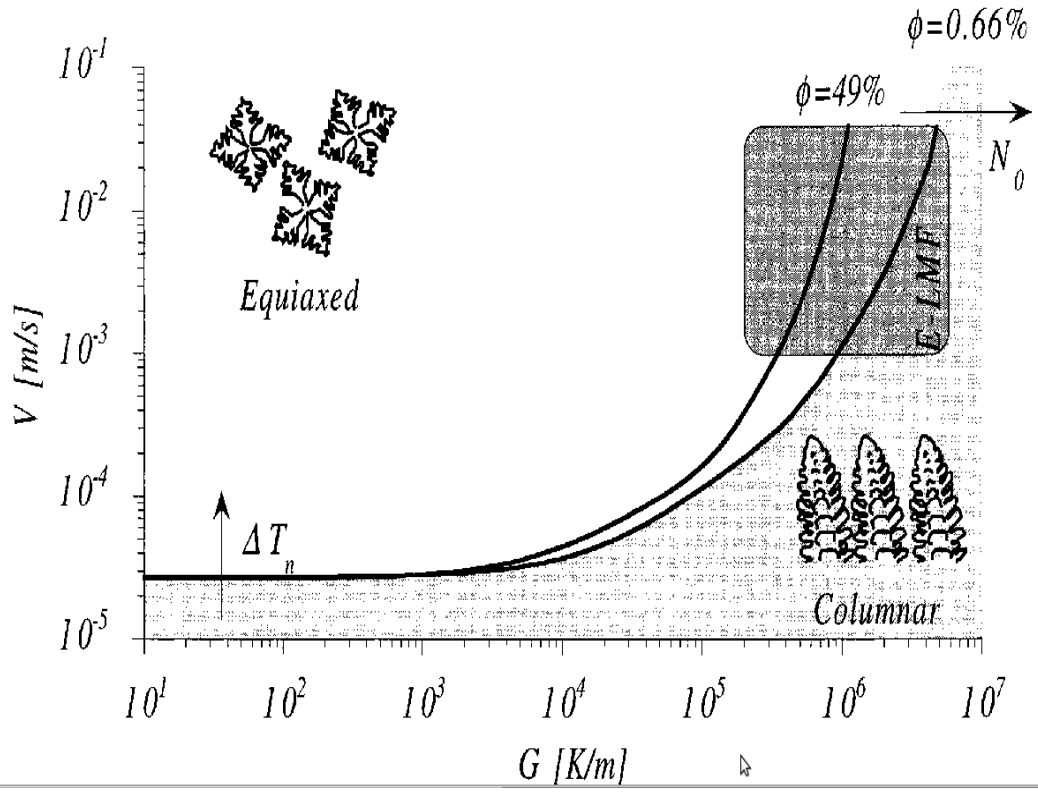

Figure 8 – Microstructure selection map showing the region of columnar dendrites and the equiaxed dendrites as a function of solidification parameters [52].

2.2.3 Power-Powder interaction

In terms of mass transfer, the beam- powder interaction needs be considered in more detail because the powder particles can absorb the laser energy and preheat themselves and consequently go through a temperature rise [56]. Even though there may be the same initial temperature for the powder particles, different ultimate temperatures can be seen owing to their different paths to reach the molten pool, leading to a substantial influence on the temperature field within the melt pool [57]. However, in the early study, the powder particles were presumed to reach the surface of the molten pool with the same temperature[58]. In reality, when the laser beam goes through the powder stream, a part of the laser energy is lost due to the absorption by and reflection from powder particles, and hence its intensity and distribution can be changed. Furthermore, powder will be blown onto the melt pool that the laser creates at the surface of the part being repaired. A fraction of the powder particles will be ejected outside the molten pool, *i.e.* blown away by the gas flow during the laser metal forming process; depending on the processing parameter, a variable fraction of the blown powder will be dissolved into the molten pool, which makes a contribution to the deposition process. This fraction needs to be characterised so as to get the actual mass flow rate in the pool. Considering the previous work in the measurement and model of beam–powder relationship: Gremaud *et al.* [59] did a quantitative study for better understanding of the laser deposition process and found that the powder efficiency appeared to be regulated for geometrical reasons by the process, leading to stable plate buildup. Picasso *et al* developed a 2D model for LMF [60], indicating that the powder particles affect laser power density by absorbing laser energy while traversing the laser beam. Weerasinghe *et al.* [61] proposed a finite difference model of laser cladding by powder injection taking into account the preheating of the powder by the laser beam. Lin *et al* [62] carried out a study on the numerical modelling for calculating the powder temperatures in a laser deposition process but the attenuation of laser power was not taken into account. Hu *et al* [63] quantitively investigated how the powder particles in the powder stream and the laser intensity influence each other

on the surface of substrate. Ludmila [64] and Ashish [65] made some effort to estimate the thermal field of a spherical particle irradiated by a laser beam by solving the heat conduction equation. Zhang *et al* [66] carried out some research with regard to the laser efficiency by optimsing the modeling results coupled with experimental validation and then developed a laser efficiency model. Pinkerton [67] and Li [68] established a model for simulating the powder-laser interaction and the subsequent attenuation by means of the Lambert–Beer law. Results show that the attenuation increases with the distance from the nozzle but the main limitation of the model is that the influence of the nozzle angle against the laser beam was not taken into account.

2.2.4 Heat transfer and fluid flow

Heat transfer must be studied in more detail to determine the thermal cycles experienced by the substrate and hence the solidification conditions. Therefore a heat source model must be adopted to give an appropriate description of the temperature distribution and evolution in the workpiece during the laser repair process. Initial models for heat flow during welding are analytical solutions or semi-empirical expressions. Rosenthal developed a solution for a moving point heat source travelling along a surface of a semi-infinite body [69]. This early study, neglecting the temperature dependence of properties, allowed the determination of the melt pool size through the calculation of the thermal field in reasonable agreement with experiments. Further developed by several authors [70，71], these analytical solutions were considered to be limited as mass and fluid flow was not taken into account, which, in some experimental results, were found to be related to the shape of weld pool. Then attempts and further improvements were made by taking into account the heat source motion effects on heat, mass and fluid flow for both two-dimensional and three-dimensional cases [72-75], which promotes the development of numerical methods for solving the mass, momentum and energy conservation equations in order to solve problems in fluid flow, phase changes and heat transfer. However, due to the presence of a number of variables, numerical calculation requires considerable

computation time. Moreover, the temperature dependent material properties have to be known, which, however, are not always readily available, making modeling results unreliable. Therefore, developing analytical methods coupled with experimental validation is more efficient for the optimisation of processing parameters. Fluid convection, also called Marangoni convection or thermocapillary convection, is actually a liquid flow pattern produced by the surface tension and this can lead to a strong influence on the size of the resulting melt pool [76]. As illustrated in Figure 9 (right hand side), if the temperature coefficient of surface tension is positive, fluid flow is generated by inward-pointing shear stresses resulting from the surface-tension gradients along the pool surface. Thereby the fluid is produced along the surface from the edge where there are high temperature and the surface tension, to the centre where temperature and surface tension are low. And obviously it can be found that fluid flow can either give rise to a flatter melt pool with a negative temperature coefficient of surface tension, or can lead to a deeper melt pool in the contrary situation when the surface energy increases with temperature [77], as shown in Figure 9. Some efforts [78-81] have been made to understand the influence of fluid flow and its effect on weld pool, as it can have an adverse impact on the resulting microstructure in most of the solidification processes [82-85]. An interesting study carried out by Jean-Marie *et al* [86] shows that the development of fluid convection in the liquid flow can indeed change the thermal field within the substrate and ultimately the molten pool shape during the E-LMF process, but the influence is not as obvious as that of powder feed and heat flow, so the main concern will be on mass and heat transfer without including Marangoni convection for the purpose of simplicity in the study which follows.

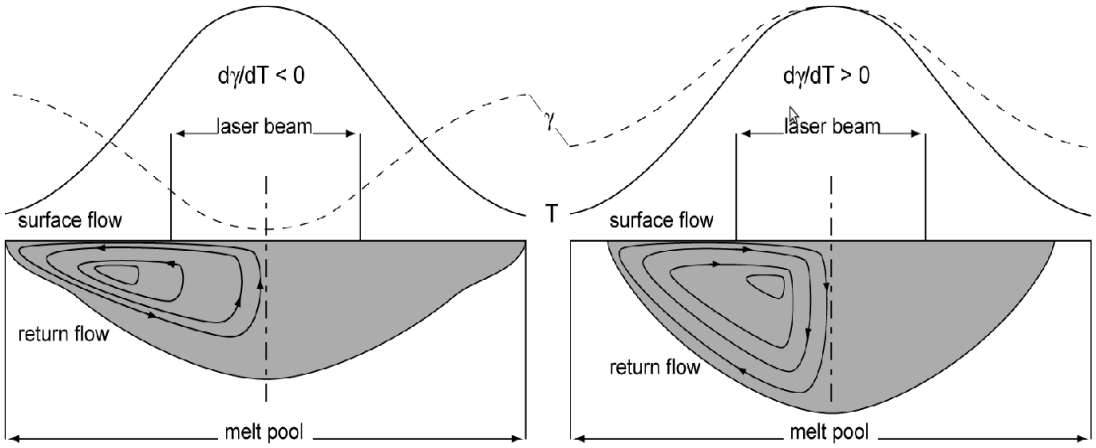

Figure 9 – Schematic representation of Marangoni convection cells in a melt pool and of their influence on the geometry [77].

2.3 Overview of thesis

In chapter 3, a simplified analytical model for the investigation of power-powder interaction is proposed. Some equations and related assumptions are given and discussed. Powder preheating temperature and power efficiency are presented on the basis of modeling results. A description of an analytical thermal model coupled with geometrical model during laser deposition process is provided in chapter 4. The temperature distribution and evaluation within the workpiece are presented and discussed for thermal analysis. The geometry of melt pool and deposition layer is predicted based on the results. The fraction of columnar and equiaxed grain is calculated using the CET model; the effect of the processing parameters is studied for the purpose of producing sufficient remelting and desired microstructure. Finally, Chapter 5 provides the general conclusions drawn from this work as well as some suggestions for future work.

Chapter 3 Powder-power interaction

In this section, a simplified analytical model of power-powder interaction is proposed. The aim of developing this model is to compute the attenuation of laser power by a power stream on the basis of classic physical theories; in addition, powder preheating temperature arising from the absorbed energy can be calculated when the powder particles arrive at the surface of the melt pool by using heat equilibrium equation. The influence of relative processing parameters on power efficiency and temperature distribution is studied under given practical processing conditions.

3.1 Analytical model of Powder-Power interaction

Figure 10 gives a 2D schematic illustration of the interaction between laser beams and powder streams during the LMF process. The coaxial nozzle has a tilt angle θ against the horizontal surface so that different feeding angles can be given. In addition the head of the nozzle is at a vertical distance of l_w from the workpiece. For the purpose of simplicity, some assumptions are made for the development of a model of the interaction between the laser beam and the powder stream:

- The powder particles are considered to be spherical.
- There is no heat loss by convection and radiation from powder particles in the stream owing to the short interaction time in the contact area.
- The influence of gravity is neglected and the flow is regarded as a steady state with constant travelling speed for both powder stream and covering gas.
- The power attenuation is dependent on the proportion of area of powder particles within the nozzle in a horizontal plane.
- There is a uniform distribution for the particle concentration in the powder stream across the nozzle centerline.
- The laser beam is neither convergent nor divergent in the interaction area with respect to the powder stream.

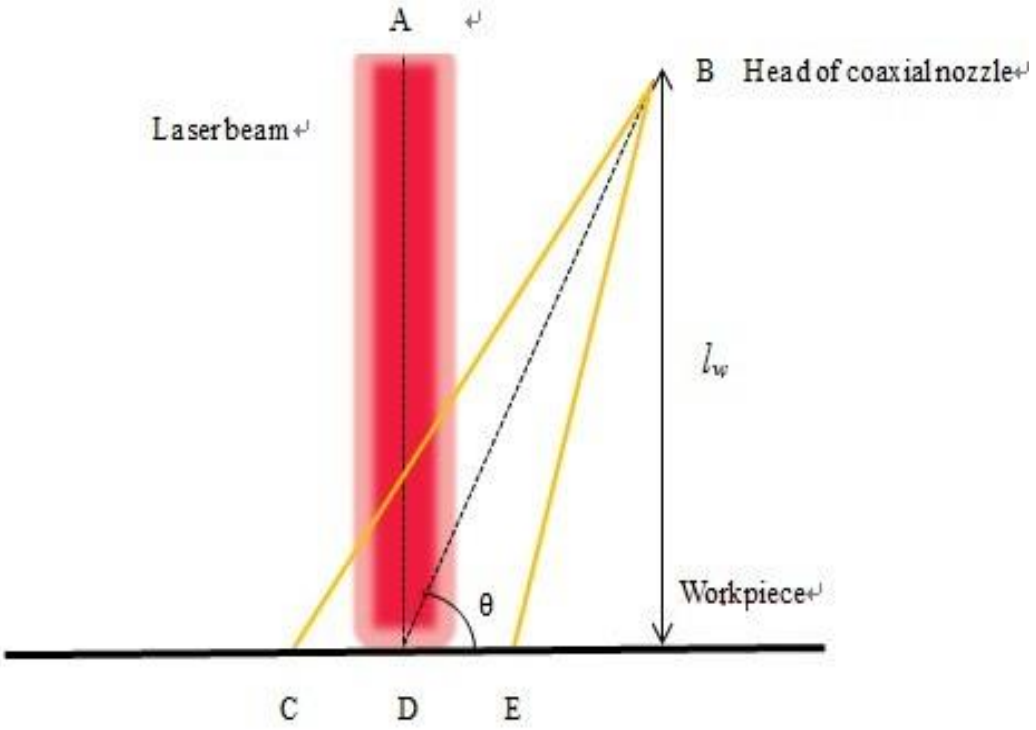

Figure 10 - Schematic illustration of the powder stream from a coaxial laser deposition nozzle.

3.1.1 Gaussian distributed laser beam

The incident laser intensity, $I_{inc}(x, y)$, has a Gaussian distribution which can be written as:

$$I_{inc}(x,y) = \frac{P}{\pi r^2} \times exp\left[\frac{-(x^2+y^2)}{r^2}\right] \quad (1)$$

where $I_{inc}(x, y)$ is the original laser intensity distribution, P is the original laser power and r is the radius of the laser beam. Figure 11 gives a 2 D calculation of the incident laser power intensity profile using a laser power of 500 W and spot diameter of 0.76 mm without considering powder injection.

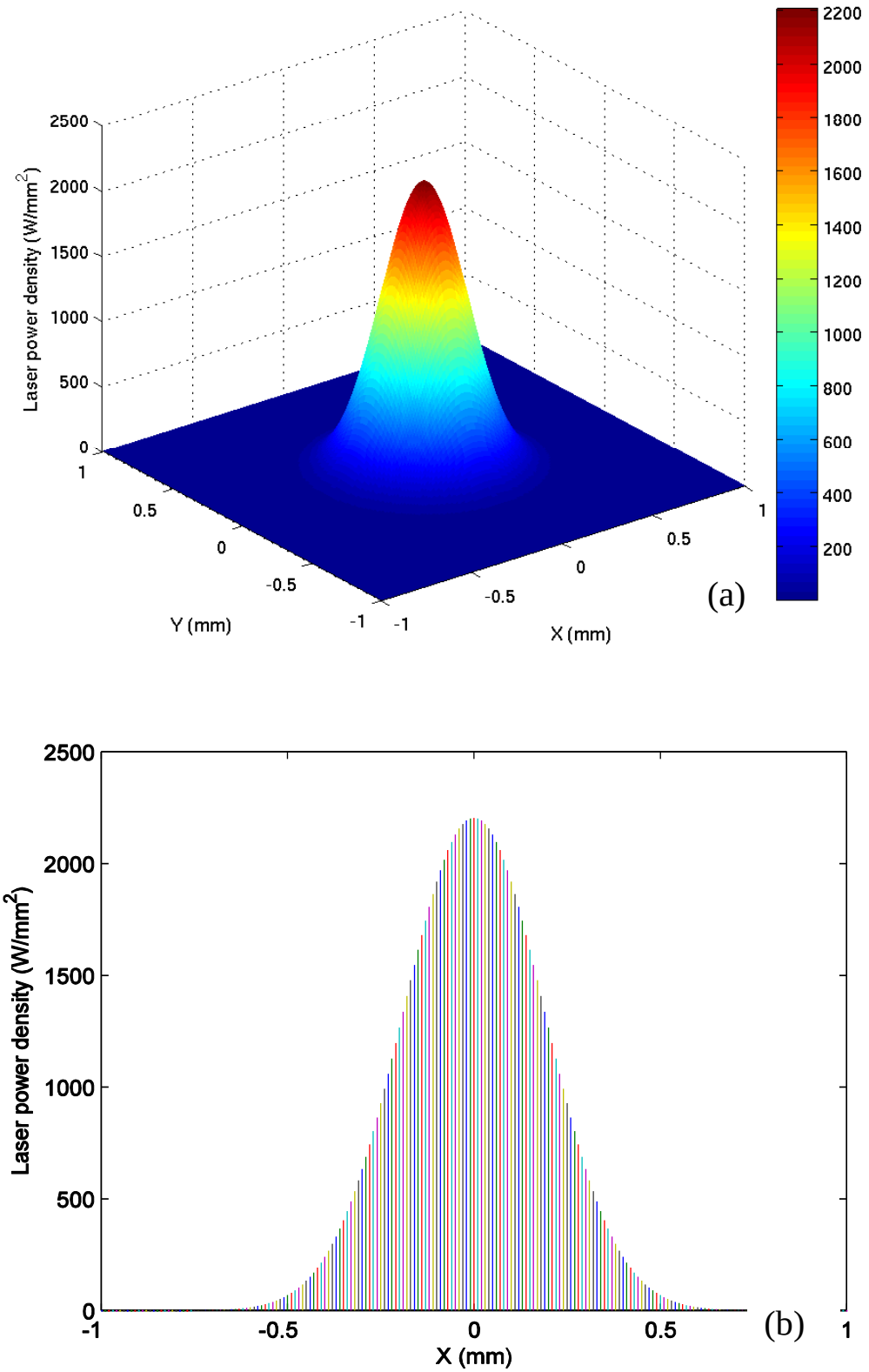

Figure 11 – A calculated profile of Gaussian distribution of laser beam on the surface of substrate, (a) three dimensional, (b) cross sectional.

3.1.2 The attenuation of laser power by the powder stream

In order to understand how powder cloud impacts power efficiency, the attenuation of laser power needs to be investigated and a model has been established in which a coefficient of laser fully blocked by powder particles is introduced. Considering the powder grains prior to the injection out of the nozzle, moving at a speed covering with the inert gas, they can influence the laser intensity distribution in terms of powder density in the laser beam as more powder particles can block more laser beam. And in the calculation which follows, powder density in the laser beam is considered to be the same as that within the nozzle. Therefore the coefficient of laser fully blocked by powder particles can be significantly based upon the ratio of area of powder particles to nozzle in a vertical view, see in Figure 12.

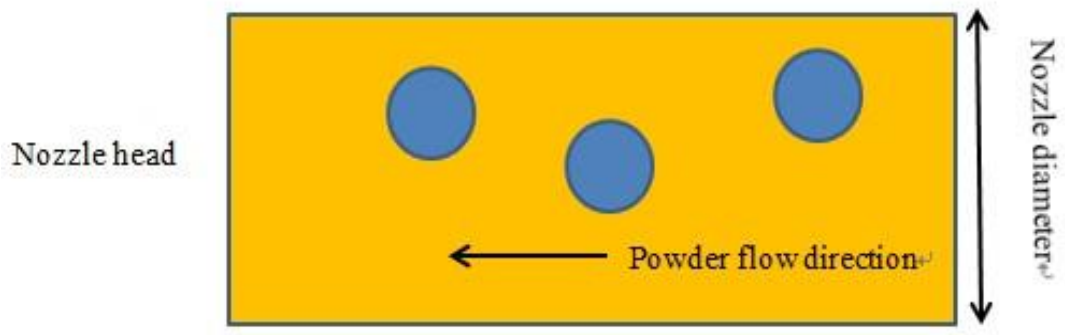

Figure 12 – Schematic illustration of a vertical view of the powder flow with the nozzle.

Apart from that, the nozzle angle with regard to the substrate also plays an important role for the power efficiency. A larger nozzle angle can lead to a closer horizontal distance between powder particles in the laser beam, and hence more laser energy will be blocked by powder particles resulting in declined laser transfer efficiency and increased power absorption by powder particles. Therefore the coefficient of laser power blocked by powder particles can be obtained according to the following equations (2) – (6):

$$S_p = \pi {r_p}^2 \tag{2}$$

$$n_p = \frac{m}{m_p} = \frac{\dot{m} \times \Delta t}{\rho \times \frac{4\pi {r_p}^3}{3}} \tag{3}$$

$$S = n_p \times S_p \tag{4}$$

$$S_n = 2r_n \frac{F}{\pi {r_n}^2} \Delta t \tag{5}$$

$$\kappa = \frac{S}{S_n} \times \frac{1}{\cos\theta} = \frac{3\dot{m} r_n}{8\rho r_p F} \times \frac{1}{\cos\theta} \tag{6}$$

Thus lower value of κ corresponds to higher power efficiency and more power energy absorbed by workpiece.

And as soon as the coefficient is obtained, the attenuated laser intensity distribution can be calculated by equation (7) and the power absorbed by a powder particle can be readily predicted by integrating the absorbed laser power across the travelling path of the powder grain.

$$I_t = I_{inc} \times (1 - \kappa) \tag{7}$$

$$P_{abs} = \pi {r_p}^2 \times \int_0^{l_w/\tan\theta} I_{inc} \times \kappa dx \tag{8}$$

where S_n, S_p and S correspond to the area of the nozzle, a single powder particle, all the powder particles within the nozzle in a vertical view. And r_p is the radius of a powder particle, r_n is the nozzle radius, n_p is the total number of powder particles within the nozzle, ρ is density of powder particles, $\dot{m}$ is powder feed rate, F is gas

flow rate, θ is the nozzle tilt angle (powder feeding angle) with respect to the horizontal surface of the substrate and P_t is the transmitted power absorbed by the substarte.

3.1.3 The temperature distributions of powder particles

According to the heat equilibrium principle and the assumption 2 made previously, there is no heat loss due to the convection or radiation from powder particles because of the short interaction time in the contact area. All the heat absorbed from laser power by the powder particles can be used to preheat the powder particles. Therefore, the heat equilibrium equation can be written as:

$$P_{abs}\alpha_p \frac{l_w}{v_p \sin\theta} = m_p c_p \Delta T \tag{9}$$

As a consequence, the powder preheating temperature is:

$$T_p = P_{abs} \times \frac{\alpha_{p\times} l_w}{v_p m_p c_p \sin\theta} \tag{10}$$

where the term $\frac{l_w}{v_p \sin\theta}$ = the travelling time for powder particles towards the surface of substrate in the contact area, T_p = the particle temperature on the surface of substrate, P_{abs} = the laser power absorbed by the powder stream, C_p = the specific heat of the particles, l_w = the working distance of the nozzle, v_p = the velocity of powder particles, m_p = the mass of a powder grain and α_p = the absorptivity of powder particle (value is assumed to be 0.5).

3.2 Results and discussion

For the purpose of the investigation for the interaction between the laser beam and powder particles, the current model has been tested under various conditions. Table 3 lists the processing parameters used in the calculation. The various parameters are mainly used to test the model and study the influence on power efficiency and subsequent powder preheating.

Processing parameters	
Power (W)	500
Spot size (mm)	0.76
Scanning speed (mm/s)	10
Feed rate (g/s)	0.5, 1, 1.5, 2, 2.5, 3
Gas flow rate (L/s)	0.3, 0.5, 0.7, 0.9, 1.1
Powder character	CMSX-4
Powder size (μm)	15, 20, 25, 30, 35
Nozzle diameter (mm)	2, 2.5, 3
Working distance (mm)	7
Nozzle angle (°)	30, 45, 60

Table 3 – Processing parameters in the used in the example for the calculation of powder heating temperature.

3.2.1 Attenuation of power energy

As is indicated in the above assumptions, there is no power which is reflected by powder particles and hence the total power can be divided into two parts, *i.e.* transmitted laser to workpiece and absorbed laser by powder particles. Figure 13 shows that the absorption of the incident power by the flowing powder particles is predicted to be around 6.5% by using the analytical model with the practical processing condition, see the red curve, whereas the rest (blue line) continues to transmit and ultimately interacts with substrate surface. This result is consistent with previous experimental understanding [26] with regard to the beam-powder interaction that a great part of the incident laser power (above 85%) is absorbed by the substrate.

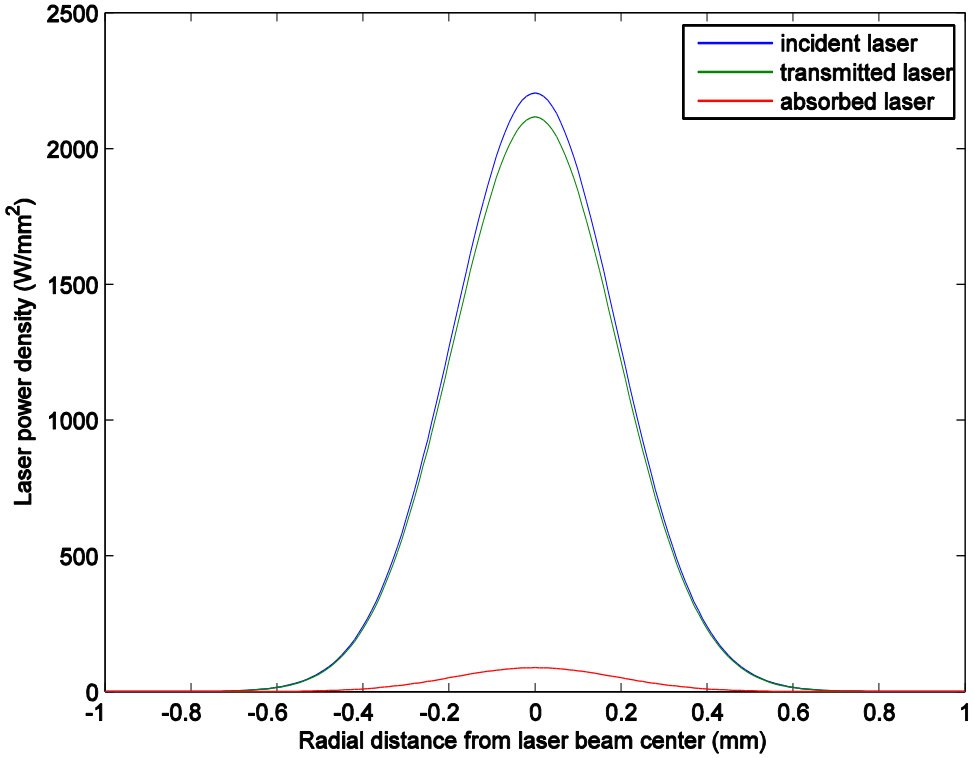

Figure 13 - Laser power (500W) intensity variation before and after passing through powder flow with 0.1 L/s gas flow rate, 0.5 g/s powder feed rate, 0.76 laser beam diameter and 25μm powder particle size. The blue line represents incident laser intensity, the red line shows absorbed laser power intensity, and the green line corresponds to the remaining laser power density.

3.2.2 Influence of relative parameters

Figure 14 shows the laser intensity distribution for various nozzle angles by means of coaxial powder feeding. One can see that the distribution of the laser intensity at large nozzle angle is similar to a Gaussian distribution, but a reduced peak value of the laser intensity is found as the nozzle angles become smaller. In addition it can also be found that approximately 60% more laser power is absorbed by powder using a nozzle angle of 60° than 30°. This means that with increasing the angle between nozzle and substrate, more power is blocked by powder particles leading to decreased laser transfer efficiency. Figure 15 shows a variation of percentage of laser power absorbed

by powder particles as a function of powder feed angle, nozzle size and powder particle radius when the powder feed rate and gas flow rate is set at 0.5 g/s and 0.3 L/s respectively. Obviously one can see that laser efficiency increases with increasing size of powder particles; this occurs because density of powder cloud within the nozzle can reduce at a fixed powder feed rate with increased powder particle size; on the other hand, however, larger size of powder stream nozzle can have an adverse impact on the power efficiency since a wider nozzle means lower gas flow speed at a fixed gas flow rate and powder feed rate resulting in a higher relative powder density in the nozzle within a certain interaction time. It is also worth noting that there is high power absorption rate with small grain size and the rate decreases with the increase of powder particle size; this is because small particles more readily absorb laser energy due to larger contact surface with laser beam. The conclusion shows a good agreement with some previous practical study. Moreover, higher power absorption rate has been found using a larger size of nozzle; this is possibly attributed to the existence of more powder grains at a certain interaction time. In Figure 16, one can see the variation of percentage of laser power blocked by powder particles as a function of powder feed rate, gas flow rate and powder particle feed angle (for 25 μm diameter grains and 2.5mm size nozzle). Obviously it can be seen that laser efficiency increases with decreasing powder feed rate and increasing gas flow rate; this occurs because a low powder feed rate and high gas flow rate can ensure a low powder cloud density within the nozzle and subsequently in the laser beam so that a smaller amount of power grains can interact with the beam. In particular, it has been found that the power absorption rate is significantly dependent upon gas flow rate. In other words, the rate increases when the gas flow rate declines; and this is more obvious at low gas flow rate, since in this case there is sufficient interaction time between laser and powder so that the laser energy attenuates faster. Additionally, in both cases the effect of powder feeding angle has been presented. Results plotted in Figure 15 and Figure 16 indicate that there is no doubt that the feeding angle has a significant influence on the power efficiency and basically more laser energy will attenuate with the increase of nozzle angle as powder particles can become closer on the horizontal plane. On the

other hand, as it is known that a variable fraction of the powder blown is dissolved in the melt pool which contributes to the manufacturing process; however, when the feeding angle is so low to achieve a better power efficiency, more powder particles will be injected outside the molten pool during the deposition process, which is not desirable. Similarly, this constraint needs to be considered for the other parameters so as to balance the efficiency of power and injection of powder grains. Therefore, modeling methods can be a good and efficient way to optimise the process control and the model proposed above has the potential to achieve that as long as it is accurate enough.

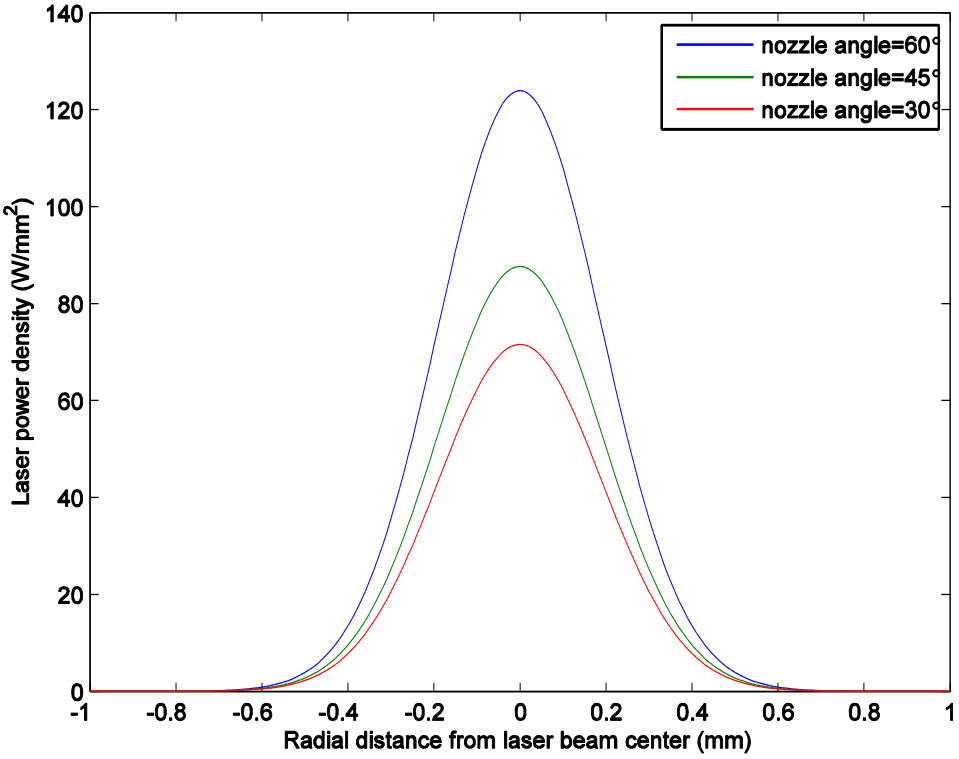

Figure 14 – Predicted intensity distribution of the absorbed laser energy by powder particles along the powder travelling path towards substrate surface as a function of radial distance from laser beam center with varying nozzle angles at a powder feed rate of 0.5g/s and gas flow rate of 0.3L/s. Different color corresponds to different nozzle angle between nozzle and substrate.

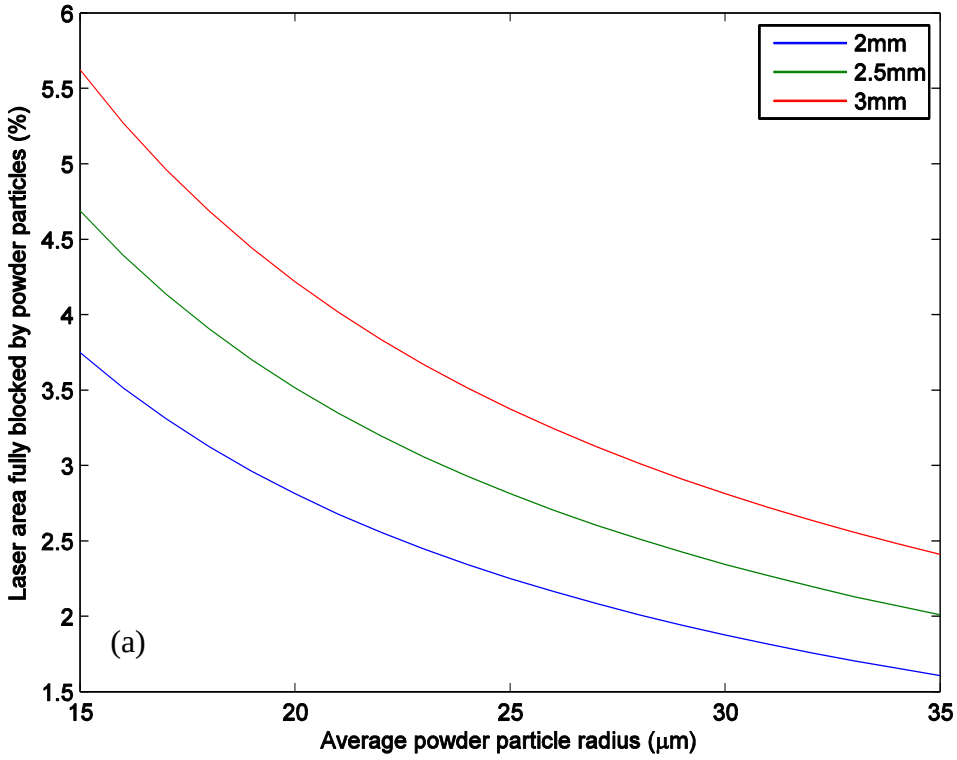
2mm
2.5mm
3mm
Laser area fully blocked by powder particles (%)
Average powder particle radius (μm)
(a)

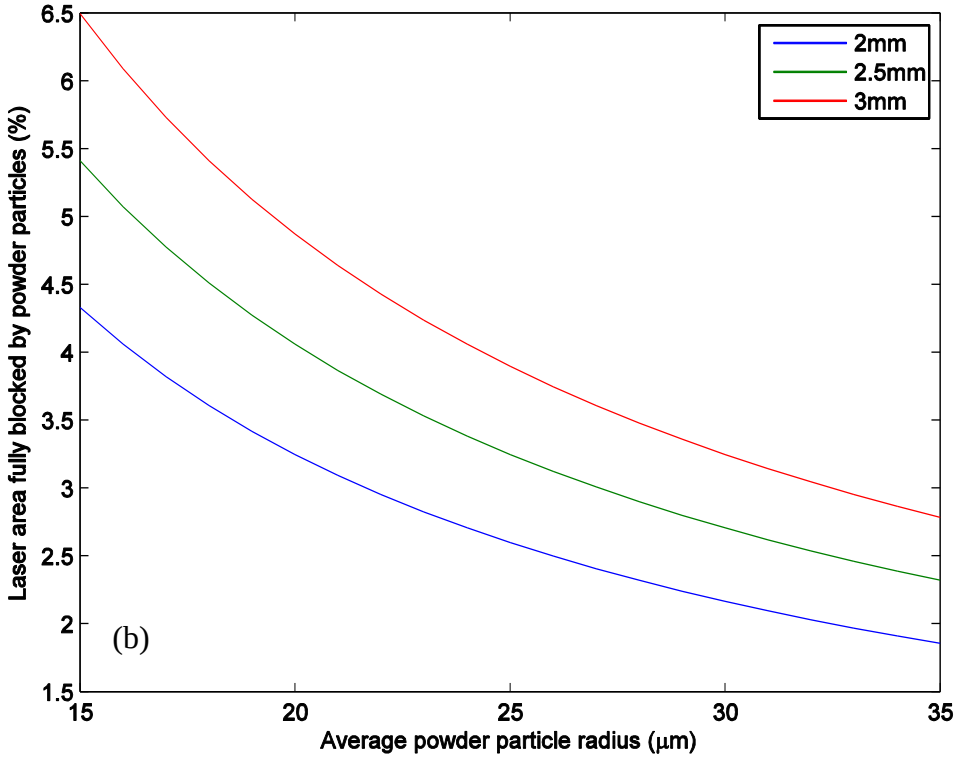
2mm
2.5mm
3mm
Laser area fully blocked by powder particles (%)
Average powder particle radius (μm)
(b)

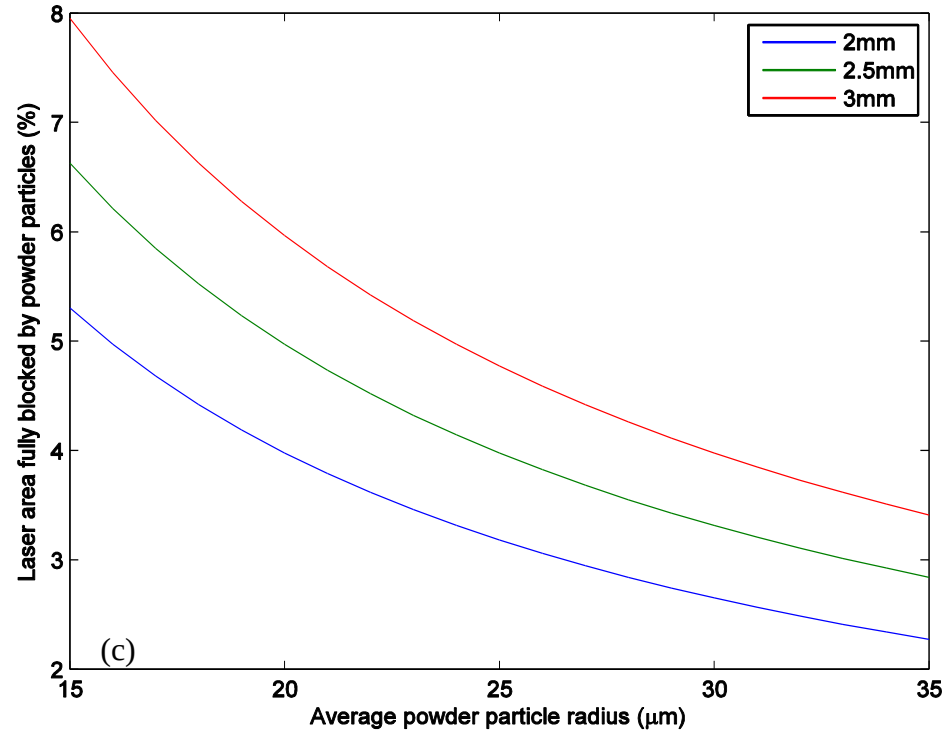

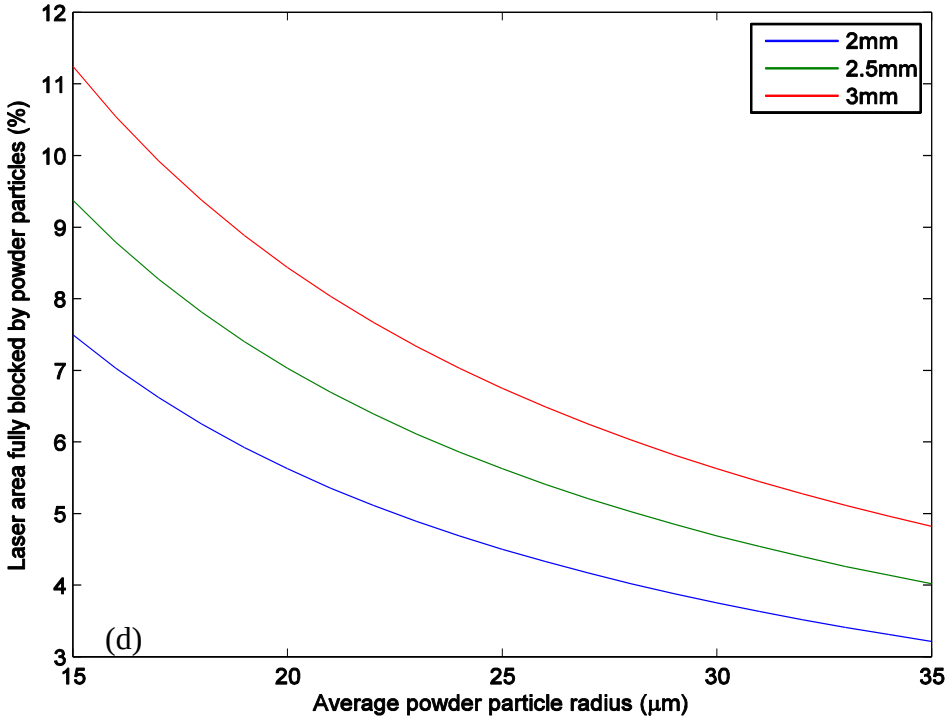

Figure 15 - Effect of nozzle diameter (colored curve corresponds to different nozzle size) and powder particle size on laser efficiency using varying nozzle angle, (a) 30 °, (b) 45 °, (c) 60 °, (d) 75 °.

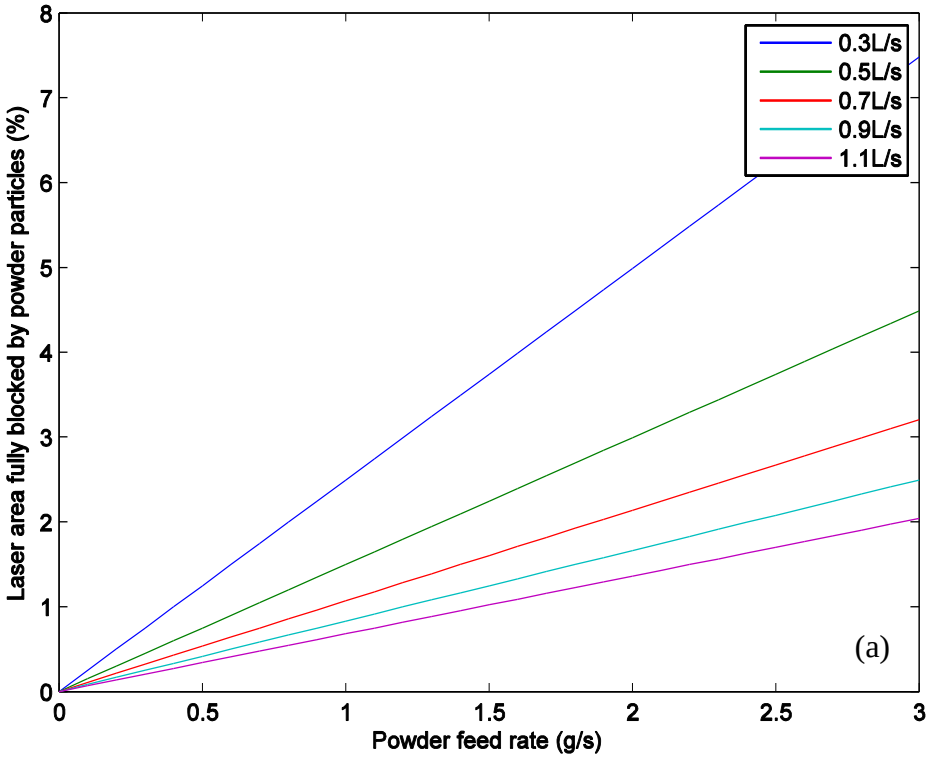
0.3L/s
0.5L/s
0.7L/s
0.9L/s
1.1L/s
Laser area fully blocked by powder particles (%)
Powder feed rate (g/s)
(a)

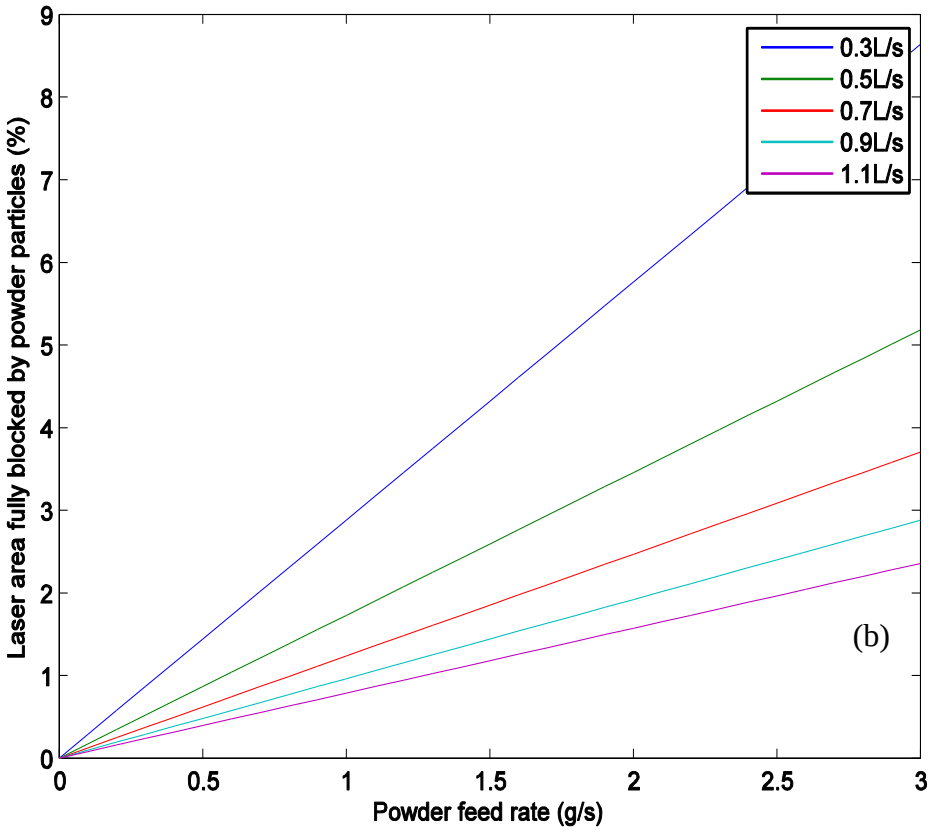
0.3L/s
0.5L/s
0.7L/s
0.9L/s
1.1L/s
Laser area fully blocked by powder particles (%)
Powder feed rate (g/s)
(b)

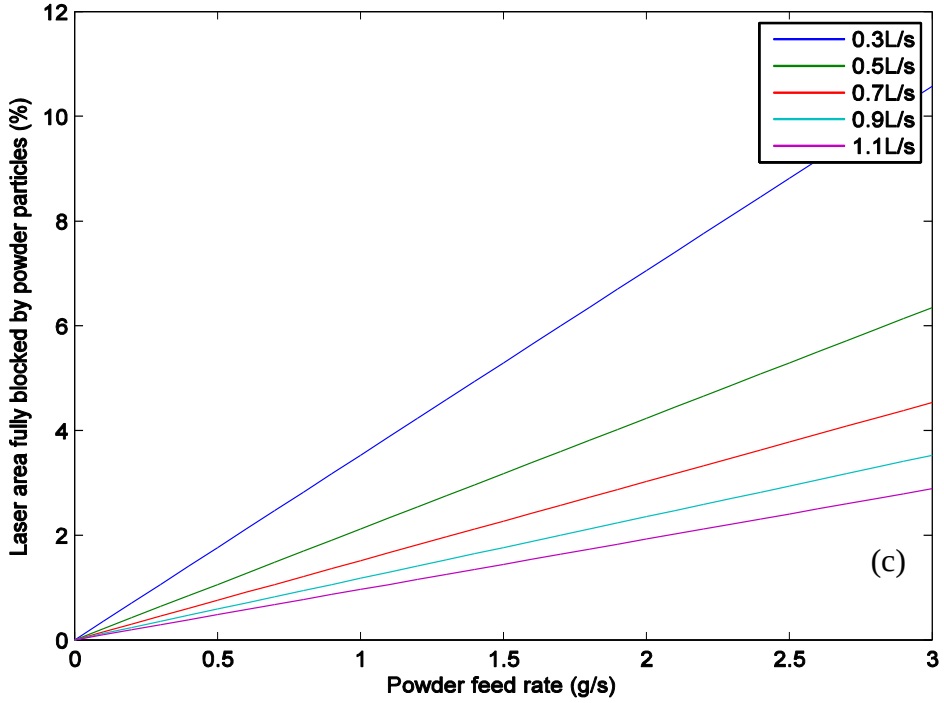

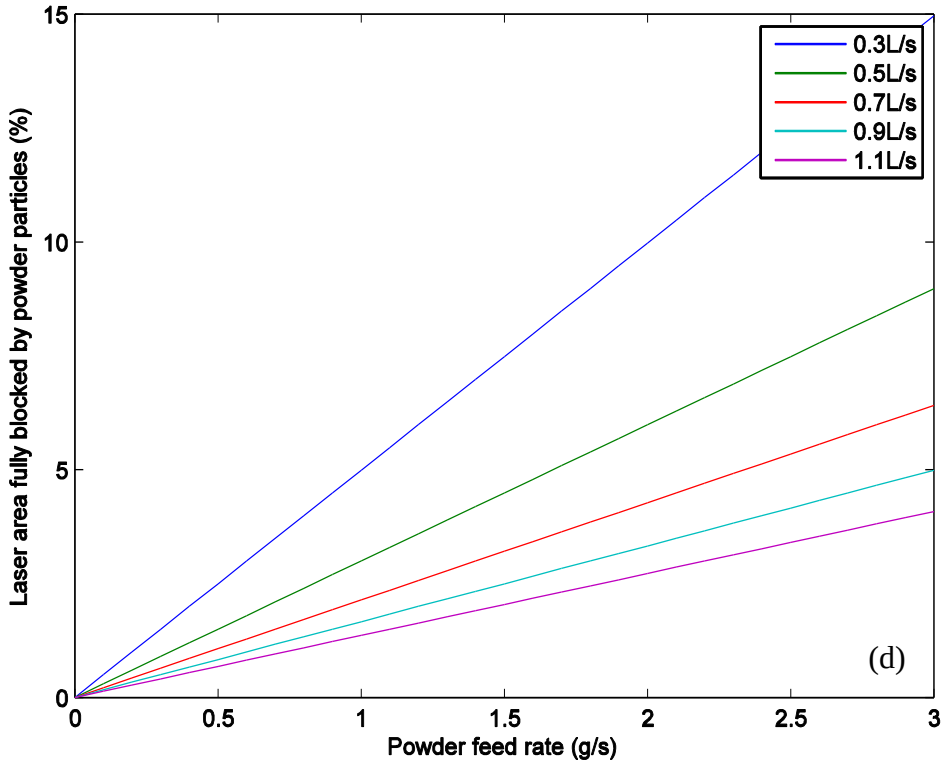

Figure 16 - Effect of gas flow rate (colored curve corresponds to different gas flow rate) and powder feed rate on laser efficiency with varying nozzle angle, (a) 30 °, (b) 45 °, (c) 60 °, (d) 75 °.

3.2.3 Case study - Powder preheating

The powder heating temperature is important due to the significance of evaluating the nature of powder particles just before dissolving into the molten pool. Therefore it is of great necessity to analytically understand the way in which powder heats. The power absorbed by powder particles can be used to calculate powder temperature anywhere during the travelling path before arriving into the molten pool according to equation (10). A variation of powder size is used to study its influence on the heating temperature. By use of the model developed in this study, Figure 17 illustrates temperature distributions of powder particles at different sizes when arriving at the surface of workpiece with a feeding angle of 45 °. Figure 18 and Figure 19 present powder preheating temperature on the surface of the substrate as a function of feeding rate and gas flow rate respectively (45 ° feeding angle and 25μm particle). It can be confirmed from these graphs that the maximum temperature values are between 620 K to 1480 K and most powder particles do not melt when dissolved into the melt pool, particularly those of a large size; the smaller size of the particle, the higher the peak value of temperature that the powder can reach; but the faster the temperature reduces from the laser beam center to the edge; this is because small powder particles are more sensitive to the energy that they absorb. Moreover, the particle temperatures would rise remarkably with increasing powder feeding rate and decreasing gas flow rate; this is consistent with the results of their influence on the laser efficiency in the previous calculation. However, there are still some limitations of this model; for example, in practice there is always a higher temperature for the powder particles reaching the negative part of the x-axis than those at the positive part due to the different travelling distance of the particles in the laser beam, which has not been accounted for in the current model. In addition, there might be a slight movement for the peak values of the reduced laser intensity after the interactions with powder cloud particularly at high powder feeding rate. These limitations are not considered because of the weak influence and the model is good enough to account for all the physical phenomena in the process.

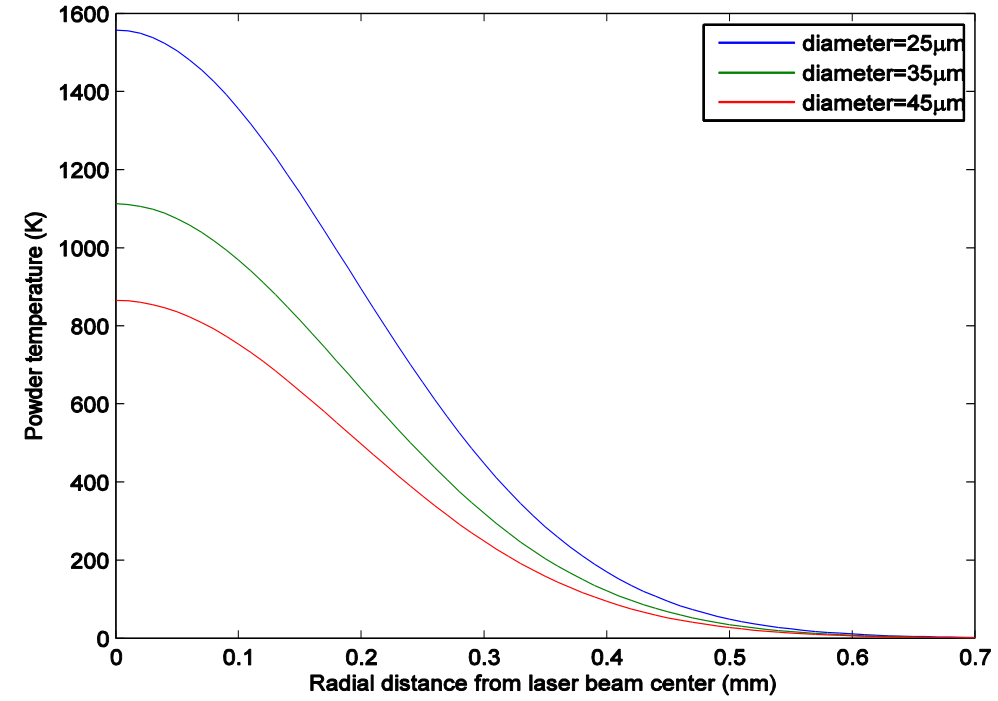

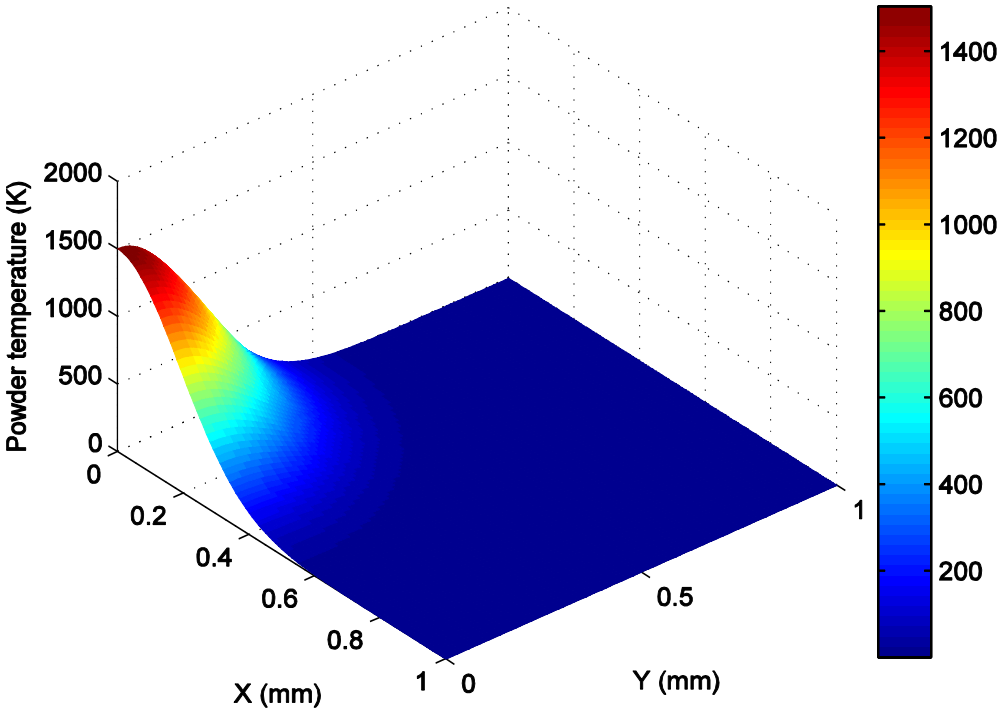

Figure 17 - Thermal distribution of powder particles when arriving at the substrate surface as a function of radial distance from beam centre with powder feed rate of 3 g/s, gas flow rate of 0.3L/s and nozzle size of 2.5 mm, (a) 2D for with varying powder size, and (b) 3D for 25µm grain size.

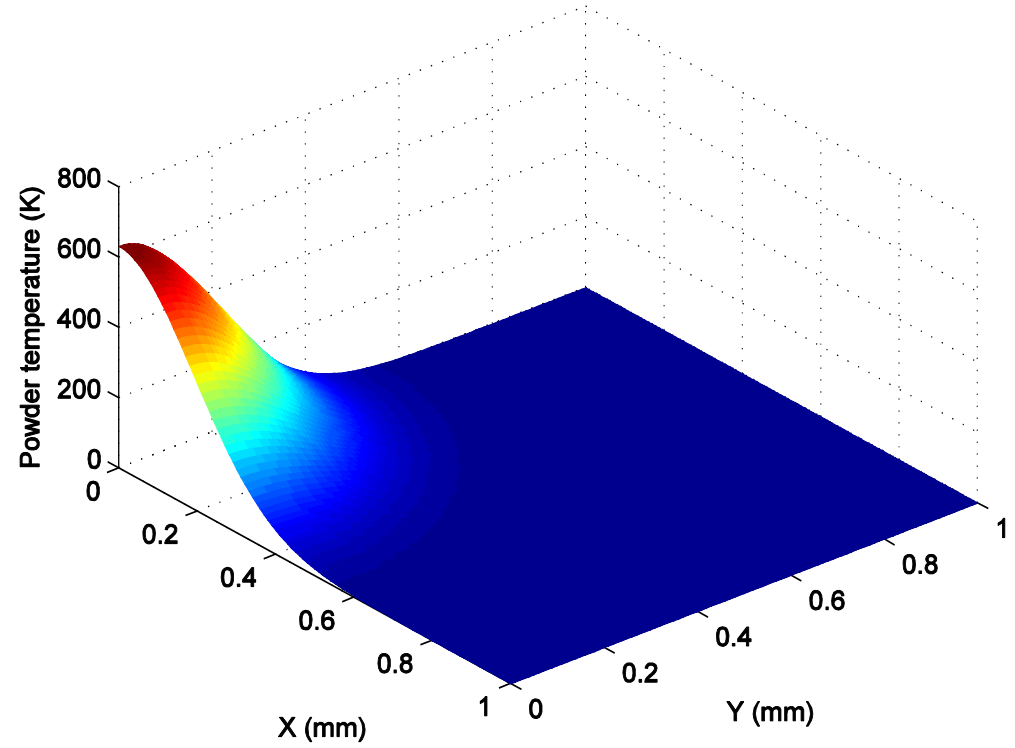
Powder temperature (K)
800
600
400
200
0
0
0.2
0.4
0.6
0.8
1
X (mm)
0
0.2
0.4
0.6
0.8
1
Y (mm)

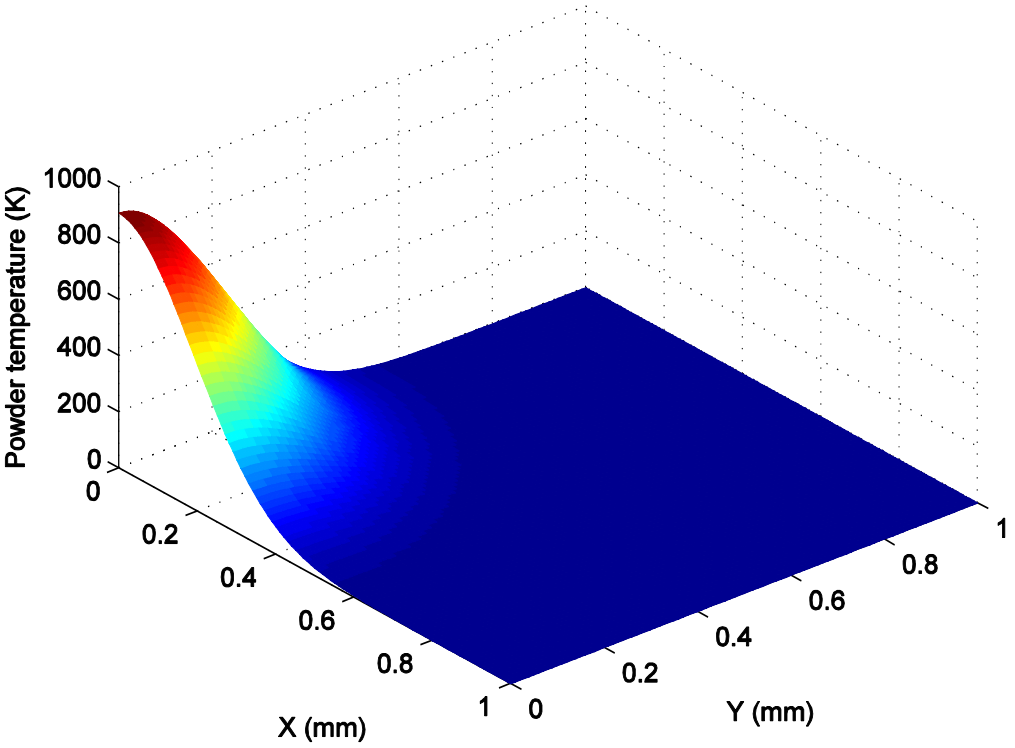
Powder temperature (K)
1000
800
600
400
200
0
0
0.2
0.4
0.6
0.8
1
X (mm)
0
0.2
0.4
0.6
0.8
1
Y (mm)

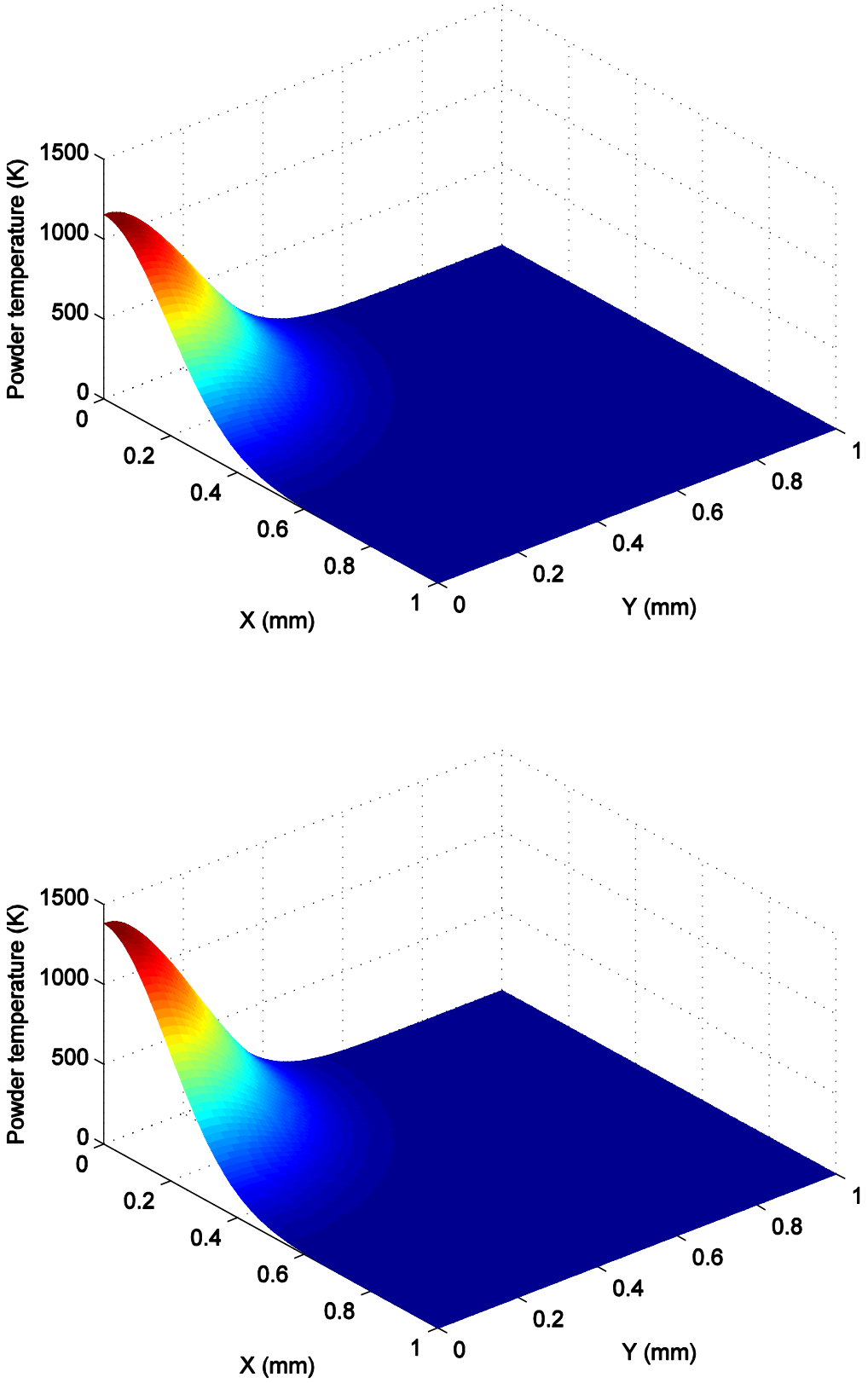

Figure 18 – Temperature distribution of particles on the surface of the workpiece with 0.3 L/s gas flow rate at different feeding rates: (a) 1g/s, (b) 1.5g/s, (c) 2g/s, (d), 2.5g/s.

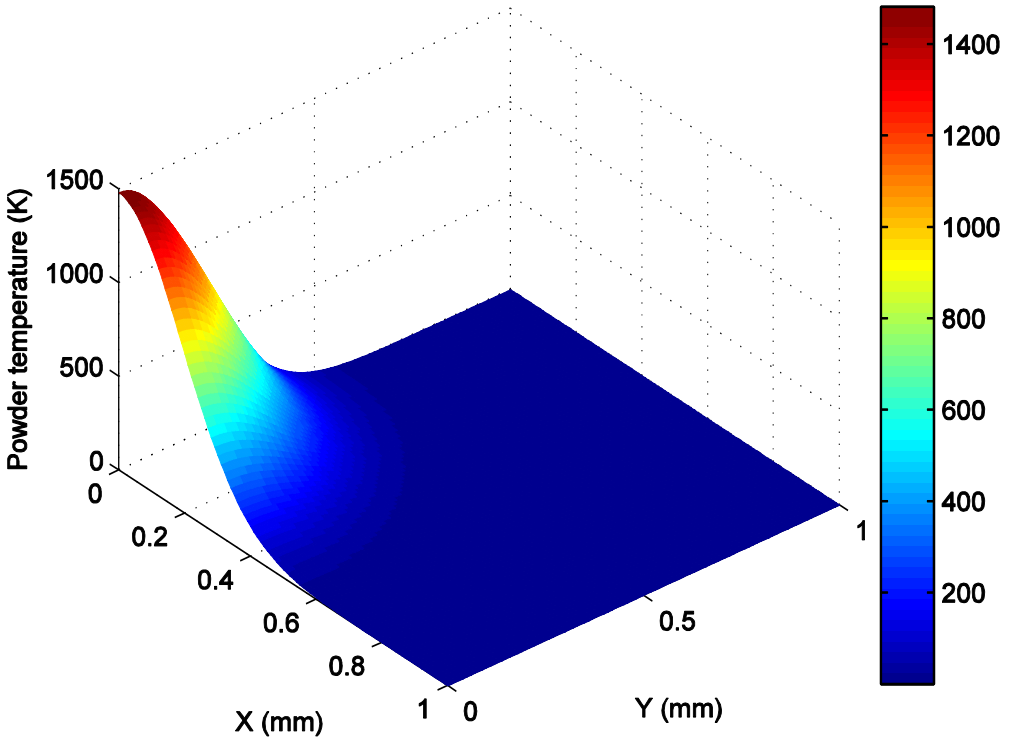
Powder temperature (K)
1500
1000
500
0
0
0.2
0.4
0.6
0.8
1
X (mm)
0
0.5
1
Y (mm)
1400
1200
1000
800
600
400
200

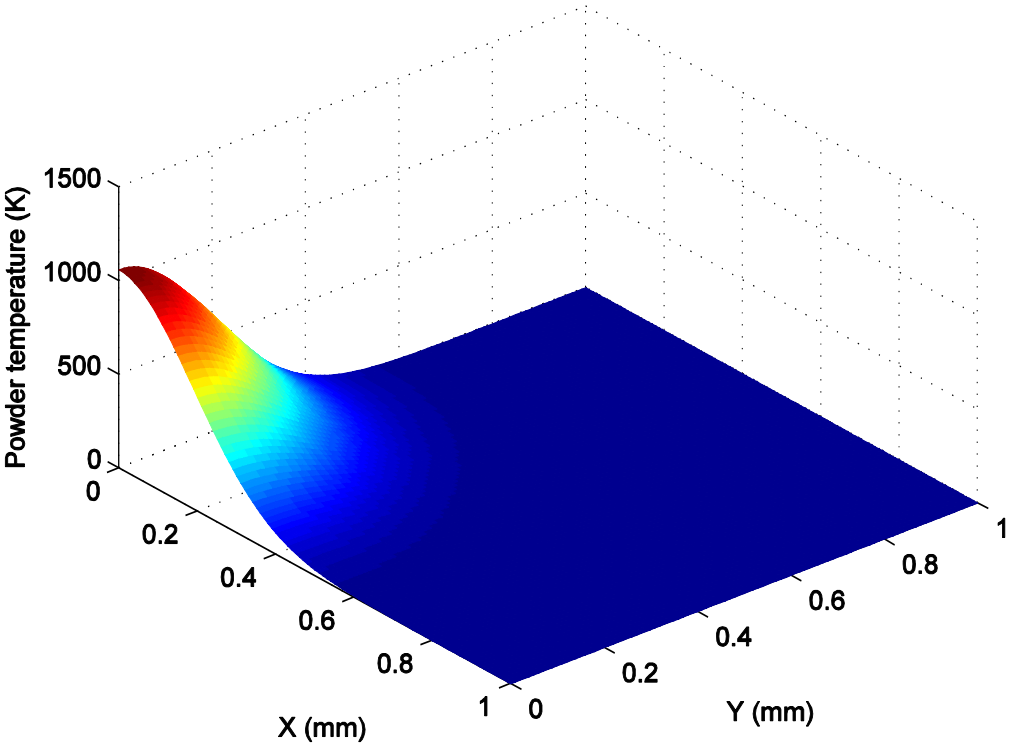
Powder temperature (K)
1500
1000
500
0
0
0.2
0.4
0.6
0.8
1
X (mm)
0
0.2
0.4
0.6
0.8
1
Y (mm)

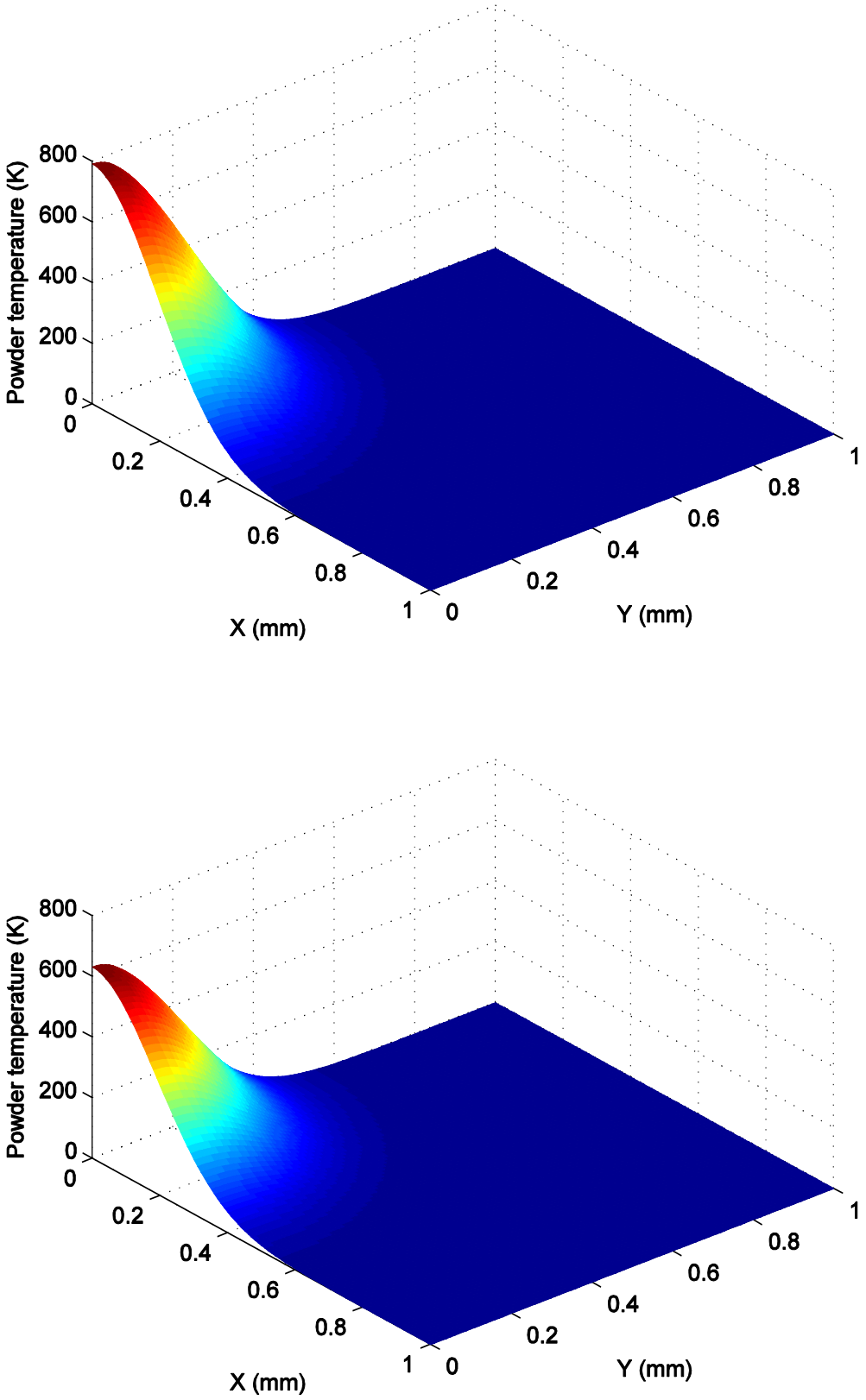

Figure 19 – Powder temperatures on the surface of the workpiece with 3 g/s feeding rate at different gas flow rate: (a) 0.3 L/s, (b) 0.5 L/s, (c) 0.7 L/s and (d) 0.9 L/s.

3.3 Summary

A model has been proposed to understand he complicated relationship between laser beam and powder stream during the LMF process. By means of the current model, the attenuation of the laser beam by a powder stream was estimated and the intensity distributions of the beam on the surface of the substrate both prior to and after the powder delivery was presented. Moreover, the thermal field of the powder particles, when reaching the surface of the substrate, was obtained on the basis of the heat equilibrium principle. In both cases, a sensitivity study was carried out for various processing parameters in order to test the model. The obtained results show that the laser efficiency is to some extent related to the powder feed rate, the feeding angle and gas flow rate; for example, more attenuation of power can be expected with the increase of power feed rate and feeding angle and a decrease of gas flow rate. Large average particle size is desirable for reducing power attenuation. It follows that the powder preheating temperature is influenced accordingly. Furthermore, results also reveal the relationship between the powder absorption rate and relevant processing parameters; for instance, a higher power absorption rate has been found using smaller powder grains and lower gas flow rate. Thereby the model proposed in this study is potentially helpful for the subsequent calculation of heat source and layer geometry. In addition, experimental work can be suggested from these findings. On the one hand, the model is helpful for the design of experimental matrix; on the other hand, future experimental work is desirable to aid in validating and developing the model. Ultimately, the complicated repair process can be optimised based on this theory and hence a better control can be achieved.

Chapter 4 Analytical analysis of laser repair process

In this chapter, an analytical model is set up to simulate the thermal behavior, the layers built-up and the microstructure evolution during the laser repair process. For the purpose of simplifying the thermal analysis, only heat diffusion will be considered; the influence of radiation and convection during the interaction between laser and workpiece is not taken into account as in most cases the process can be completed in a very short time. Moreover, several other factors which can reduce the laser energy are not accounted for in the present model, such as latent heat, partial reflection on the deposited metal, absorption by evaporating metal from the pool, and the temperature dependent material properties. Moreover, some other complicated phenomena occurring within the melt pool, for instance, melting, evaporation and fluid flow are not considered in the following study. In addition, the influence of powder injection will be neglected due to its complexity for the analytical model and relatively weak influence compared with the other parameters and phenomena.

4.1 An analytical model of heat transfer

Based on a modification of Rosenthal's equations [87], Ashby and Easterling have developed an analytical model for the distribution of thermal field produced by a finite heat source [88]. They proposed the replacement of the point source [89], which shows a poor prediction of the melt pool shape for a thick plate, by a circular disc source with radius r_b, travelling with the scanning velocity v_b in the *x* direction across the surface of a sufficiently thick plate. It follows that, at a point *(y, z)* beneath the surface, the thermal cycle *T (y, z, t)* is given by

$$T - T_0 = \frac{\frac{q}{v}}{2\pi\lambda[t(t+t_0)]^{\frac{1}{2}}} \times exp\left\{-\frac{1}{4a}\left(\frac{(z+z_0)^2}{t} + \frac{y^2}{(t+t_0)}\right)\right\} \tag{11}$$

where T is the temperature, T_0 the preheat temperature, λ the thermal conductivity, a the thermal diffusivity, q the laser power and t represents the time. The y and z co-ordinates are the horizontal and vertical distances respectively measured from the center-line of the laser beam track. The term t_0 refers to the heat transfer time over the source half-width r_b, and is defined by

$$t_0 = \frac{{r_b}^2}{4a} \tag{12}$$

where z_0 corresponds to a characteristic length, which is employed for the limitation of the surface temperature to a finite value from

$${z_0}^2 = \left[\frac{r_b}{e}\left(\frac{\pi a r_b}{v}\right)^{1/2}\right] \tag{13}$$

4.2 Results and discussion

4.2.1 Thermal behavior

Firstly, calculation starts from the power-powder interaction model proposed in chapter 3. The initial processing parameters and constant material properties for CMSX-4 are listed in Table 4. By means of the parameters provided below, the power efficiency can be readily determined. As a consequence, around 96% of the power energy is predicted to transmit to the substrate and thereby the peak temperature of powder particles is around 600K when arriving at the surface of the workpiece. Therefore, laser energy of 768W will be regarded as an input value for the calculation of thermal distribution within the workpiece and hence the molten pool size. The influence of powder injection will be neglected due to its complexity for the analytical model and relatively weak influence compared with the other parameters and phenomena. The transmitted laser beam with a Gaussian distribution interacts with the workpiece leading to a temperature variation within the workpiece. Figure 20 (a), (b) and (c) gives a view of temperature contour in different sections. Figure 21 illustrates the calculated temperature distribution experienced by the points along Y axis (in

Figure 19(a)), and Z axis (in Figure 19(c)) as a function of time. Apparently it can be seen that the temperature increases sharply and reaches a peak value at the very beginning of the process, *i.e.* the heating stage, followed by a gradual decline, which is the cooling stage. Therefore the heating behavior is various at different positions within the workpiece. A shorter heating stage can be seen on the position closer to the spot center; for example, it takes around 0.2 seconds to reach the peak temperature on the fusion boundary. However, for the points farther away the laser center, it can take 0.4 s ~ 0.5 s to come to the peak value of temperature. This is due to the fact that the heat flows from the beam center to the edge of the workpiece and the time is related to thermal conductivity coefficient. Additionally, the cooling stages are also found to be distinct at different positions. On the solid-liquid interface, the cooling rate can be as high as 4000 ℃/s, and then decreases gradually with the laser proceeding after reaching the peak temperature. For the positions away from the coordinate center, it may need more time for the workpiece to cool down to the room temperature.

Processing parameters	
Power (W)	800
Spot size (mm)	0.76
Scanning speed (mm/s)	10
Feed rate (g/s)	0.5
Gas flow rate (L/s)	0.3
Substrate and Powder character	CMSX-4
Powder size (μm)	25
Nozzle diameter (mm)	2.5
Working distance (mm)	7
Nozzle angle (°)	45
Initial temperature (℃)	20
Nozzle diameter (mm)	2.5
Thermal diffusivity (m2/s)	3.7×10^{-6}
Thermal conductivity (W/m/K)	22

Table 4- Processing parameters and material properties [25] used in the analytical model.

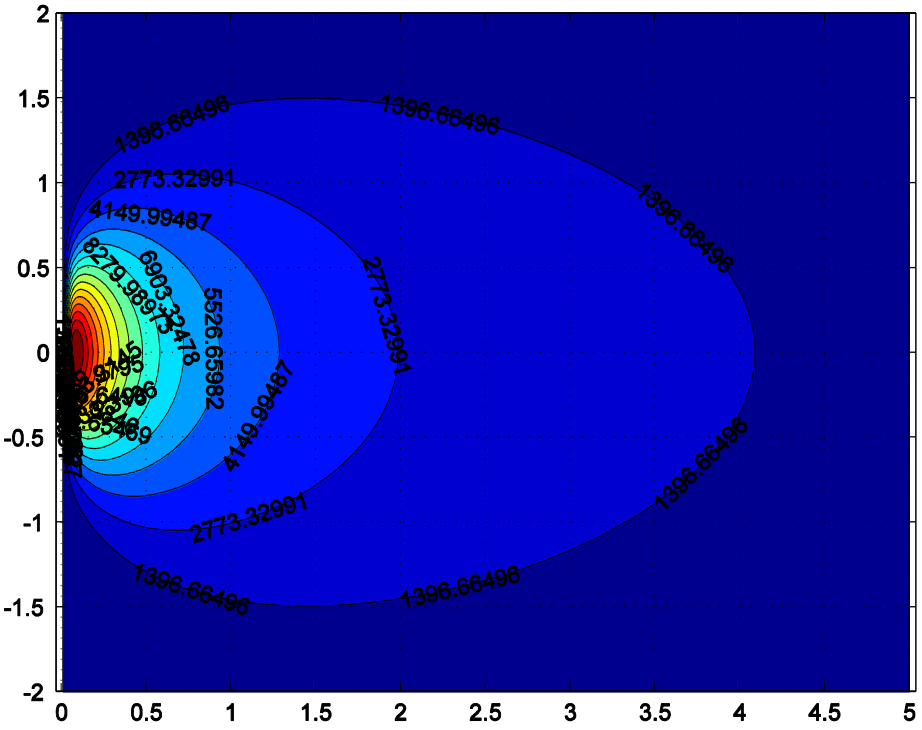
2
1.5
1
0.5
0
-0.5
-1
-1.5
-2
0
0.5
1
1.5
2
2.5
3
3.5
4
4.5
5
1396.66496
2773.32991
4149.99487
8279.98975
6903.32478
5526.65982
1396.66496
2773.32991
4149.99487
2773.32991
1396.66496
1396.66496
1396.66496
1396.66496

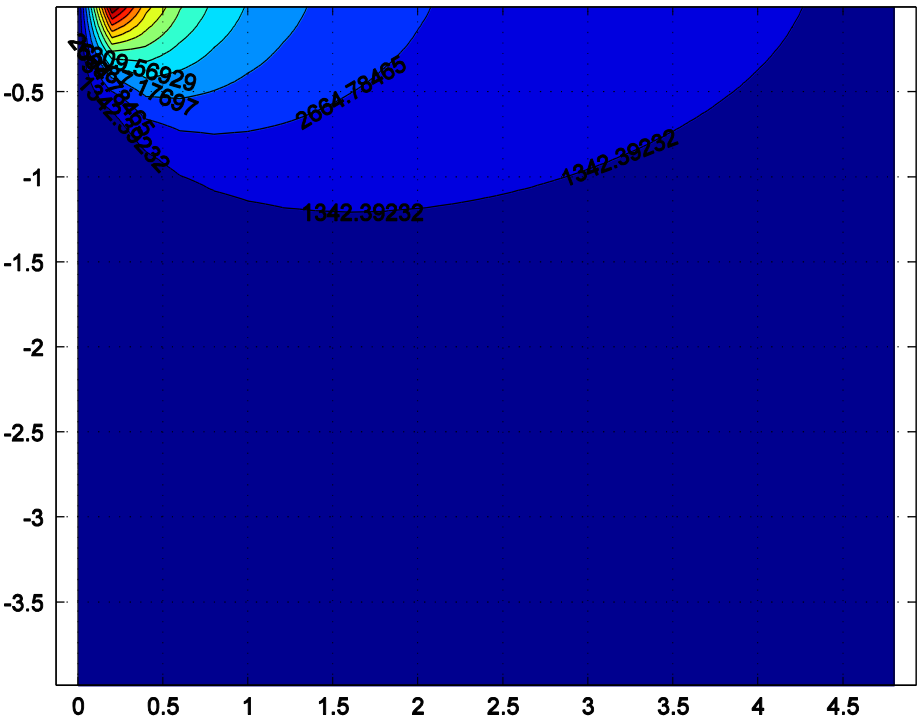
-0.5
-1
-1.5
-2
-2.5
-3
-3.5
0
0.5
1
1.5
2
2.5
3
3.5
4
4.5
2664.78465
1342.39232
1342.39232
1342.39232

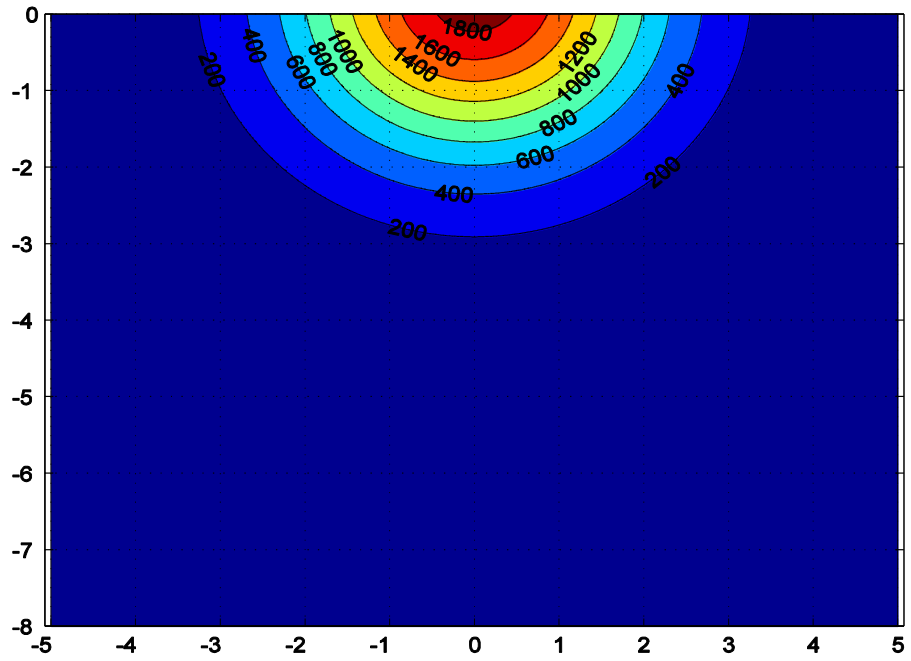

Figure 20 – Temperature contour (℃) (a) on X-Y plane, (b) on X-Z plane, (c) on Z-Y plane at peak time

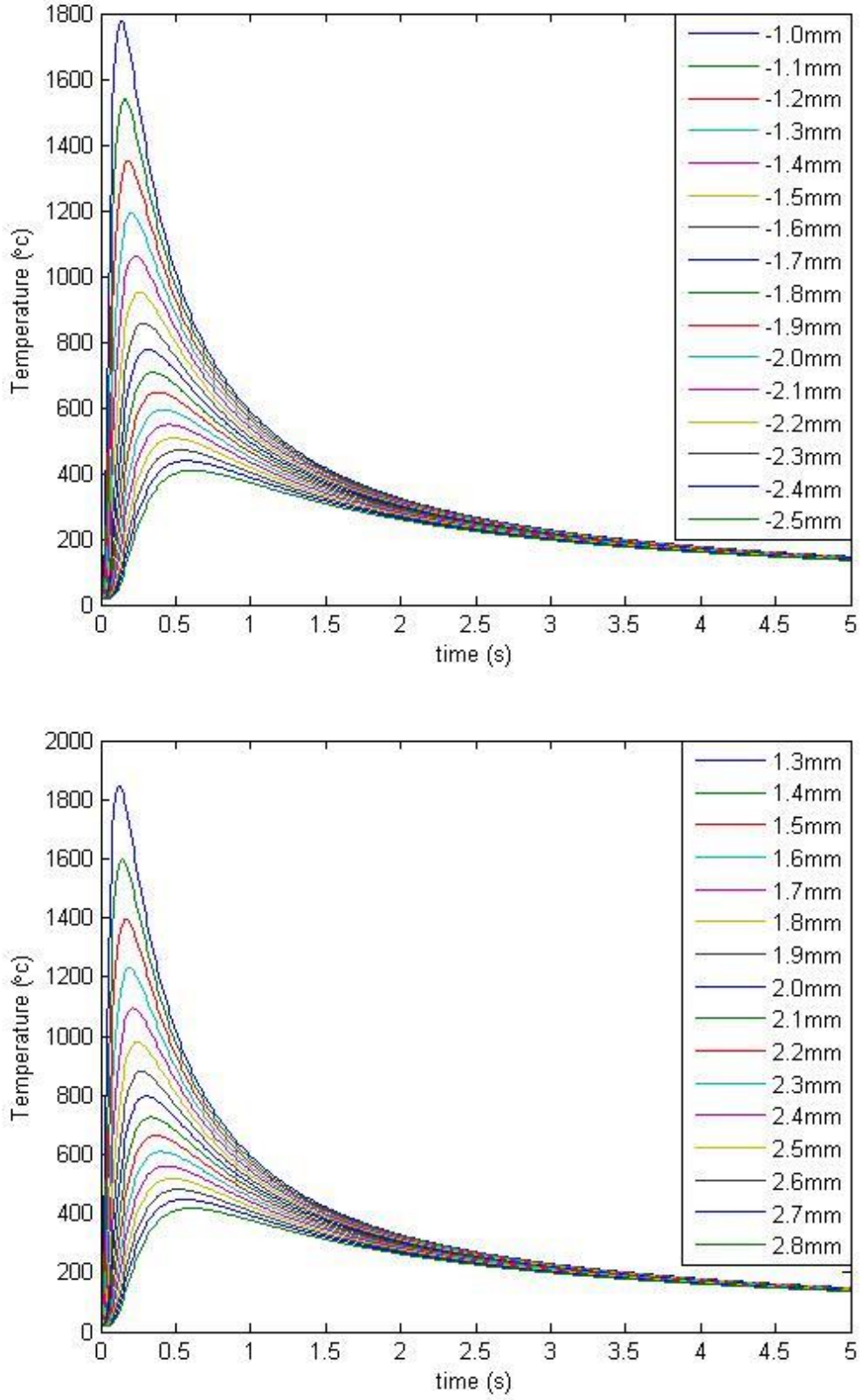

Figure 21 – (a) thermal cycle experienced by the points along z coordinate (y=0), (b) thermal cycle experienced by the points along y coordinate (z=0); the lines with different color show position along z or y for each trace.

4.2.2 Molten pool

As the molten pool is of paramount importance for the determination of the solidification behavior as well as the generation of the subsequent microstructure, the shape and influential factor of molten pool need to be studied in more detail. Following the temperature contours in different sections as shown Figure 19, it can be predicted that the melt pool shape can vary with time within the workpiece and reach the maximum value at the peak temperature; this is considered to be consistent with the characteristics of temperature evolution during the process. Therefore, in order to determine the peak temperature and hence the maximum melt pool shape, it is necessary to differentiate equation (11) to give

$$2at_p\left(2t_p + t_0\right)\left(t_p + t_0\right) = {t_p}^2y^2 + (z + z_0)^2\left(t_p + t_0\right)^2 \qquad (14)$$

where t_p is the peak time. By means of Equation (14), the shape of molten pool can be calculated by the liquidus isotherm of CMSX-4. Given the processing conditions, Table 4 illustrates the calculated 3D shape of the melt pool as well as 2D pool geometry in different sections at the peak temperature; it is predicted that the pool is stationary as the laser proceeds with the depth of 1.21 mm, width of 2.9 mm and length of 4.1 mm. However, this estimation needs to be calibrated in the experimental study, since in the real case there are a number of factors which can make the pool deviate from the modelling prediction. For instance, as mentioned in chapter 2, fluid flow can cause a flatter molten pool under the condition that the surface tension declines with temperature, or can lead to a deeper melt pool in the contrary situations; moreover, it has been proven that powder injection has the capability to tilt the molten pool, producing an influence on the deposition height and the shape of the molten pool. On the other hand, these factors are always studied numerically and considered to be secondary compared with the operating variables, such as laser power, scanning speed and spot diameter. Thus these parameters are focused on in the section which follows.

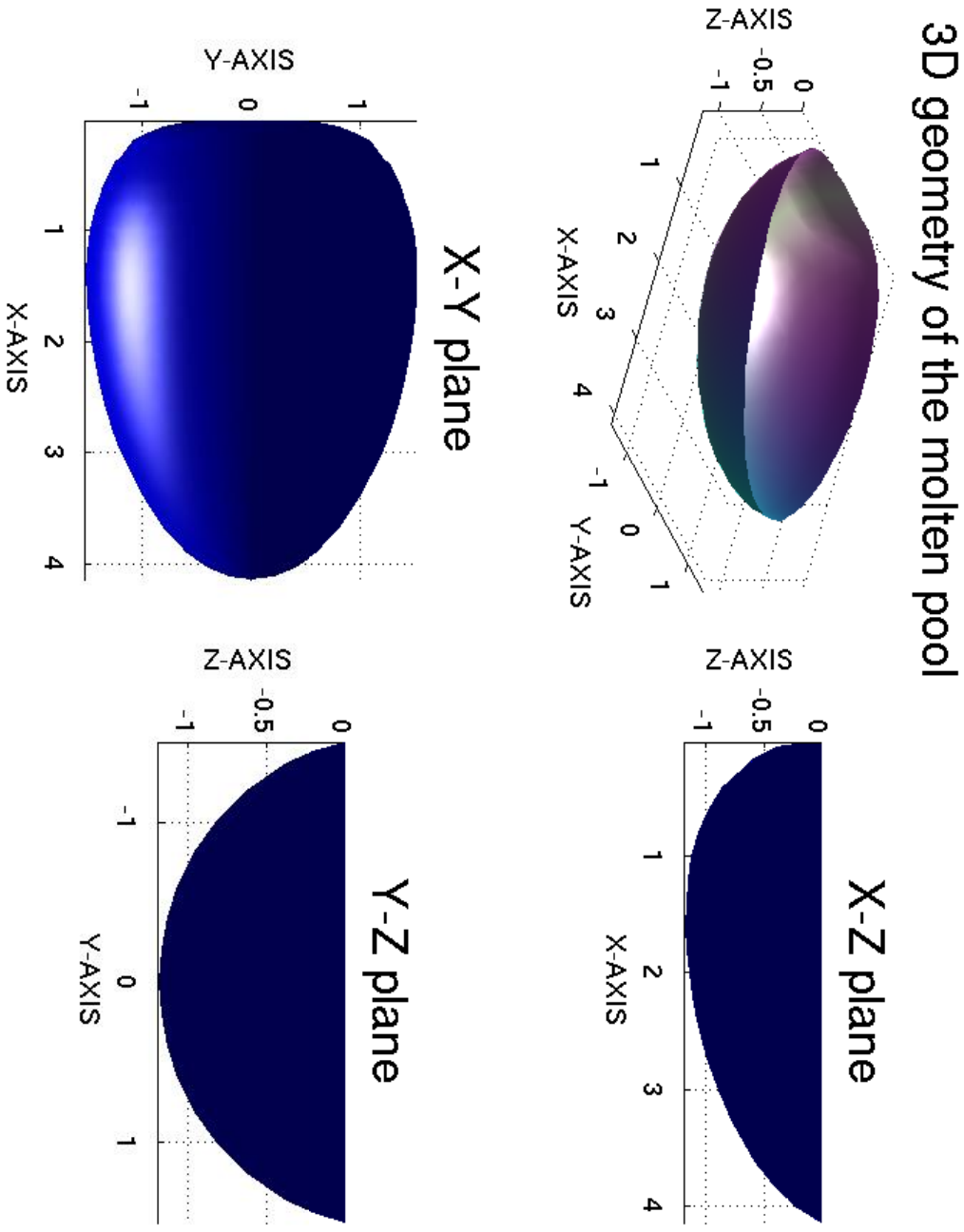

Figure 22 – Prediction of melt pool shape: 3D on the top right, 2D for the sectional view on X-Z, Y-Z and X-Y planes respectively with the processing conditions listed in Table 4.

4.2.3 Influence of processing parameters

As discussed above, the way of the processing parameters needs to be understood in more detail; thus a sensitivity analysis has been implemented with regard to the effect of these parameters on the melt pool shape. With the laser beam proceeding, the workpiece is subject to a thermal cycle, leading to the variation of the fusion zone dimensions which depend on the operating parameters: the spot size, laser power and beam speed. In the calculations which follow, the values of the width and penetration are plotted as a function of the above parameters respectively. As shown in Figure 23 (a), the penetration depth goes up steadily with the increase of laser power from 0 to 2 kw; Figure 23 (b) sees a similar influence of laser power on the width of weld bead; this is because higher laser power can generate more heat input leading to higher temperature and ultimately the expansion of the fusion zone. It is also worth noting that the penetration depth is more sensitive at lower power energy and the rate can decrease gradually with the power increasing; this is because the heat transfer is more sensitive to the power variation at lower power, in other words, a shorter distance is needed for the heat to flow to the fusion area. In Figure 23 (c) and Figure 23 (d), the evolution of laser scanning speed with respect to the fusion profile has been investigated; one can see that there is an obvious shrinkage of the fusion zone with an increase of velocity, and specifically, at low scanning speed, it can cause a considerable increase of the fusion zone dimension; this is due to the elevation of heat input and sufficient time for the heat flow. Figures 23 (e) and 23 (f) reveal that as laser beam diameter increases resulting in lower power concentration, the melt pool width and penetration depth decrease. Interestingly, if the laser beam diameter is large enough, above 4mm, it has nearly the same size as the width of melt pool. Therefore, the pool is found indeed to have a close relationship with the parameters and is especially more sensitive at lower power energy and scanning velocity. This is potentially helpful for the process control when coupled with the microstructure model.

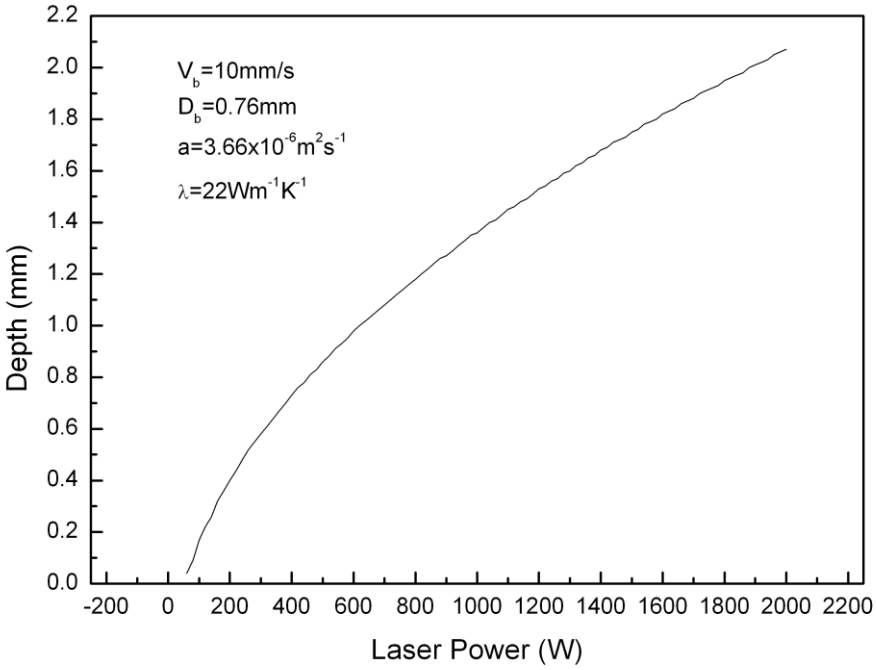
V_b=10mm/s
D_b=0.76mm
a=3.66x10^{-6}m^{2}s^{-1}
λ=22Wm^{-1}K^{-1}
Depth (mm)
Laser Power (W)

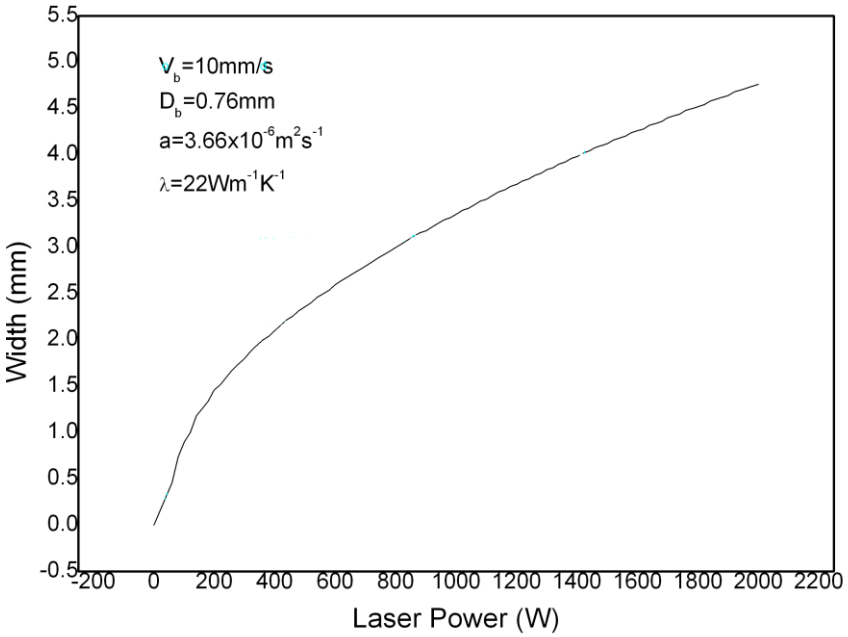
V_b=10mm/s
D_b=0.76mm
a=3.66x10^{-6}m^{2}s^{-1}
λ=22Wm^{-1}K^{-1}
Width (mm)
Laser Power (W)

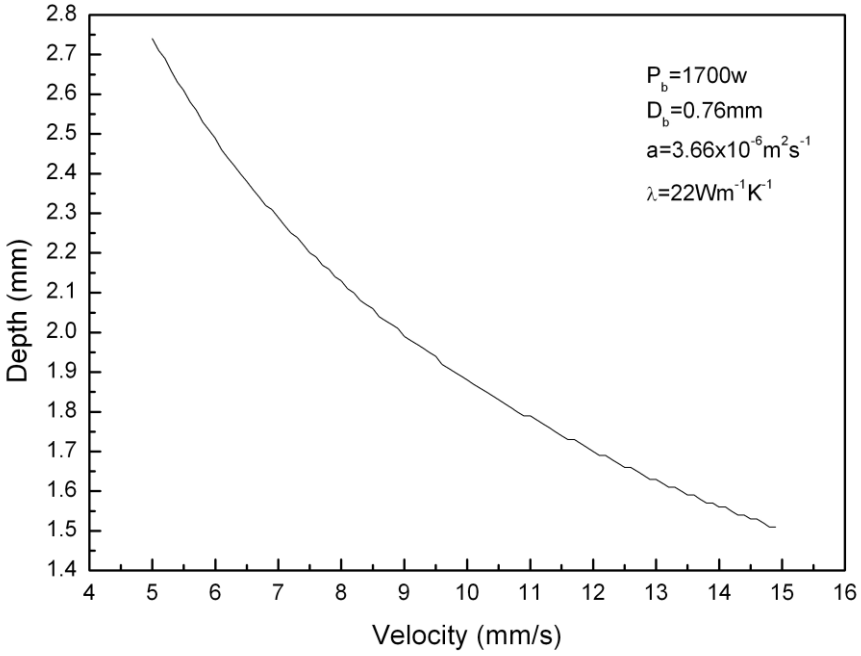
Depth (mm)
Velocity (mm/s)
P_b=1700w
D_b=0.76mm
a=3.66x10^{-6}m^{2}s^{-1}
λ=22Wm^{-1}K^{-1}

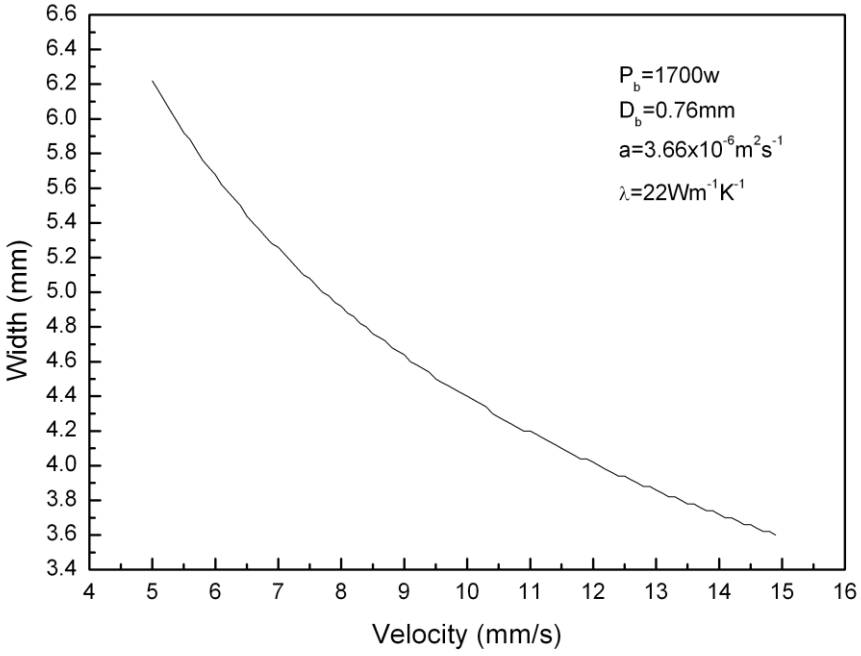
Width (mm)
Velocity (mm/s)
P_b=1700w
D_b=0.76mm
a=3.66x10^{-6}m^{2}s^{-1}
λ=22Wm^{-1}K^{-1}

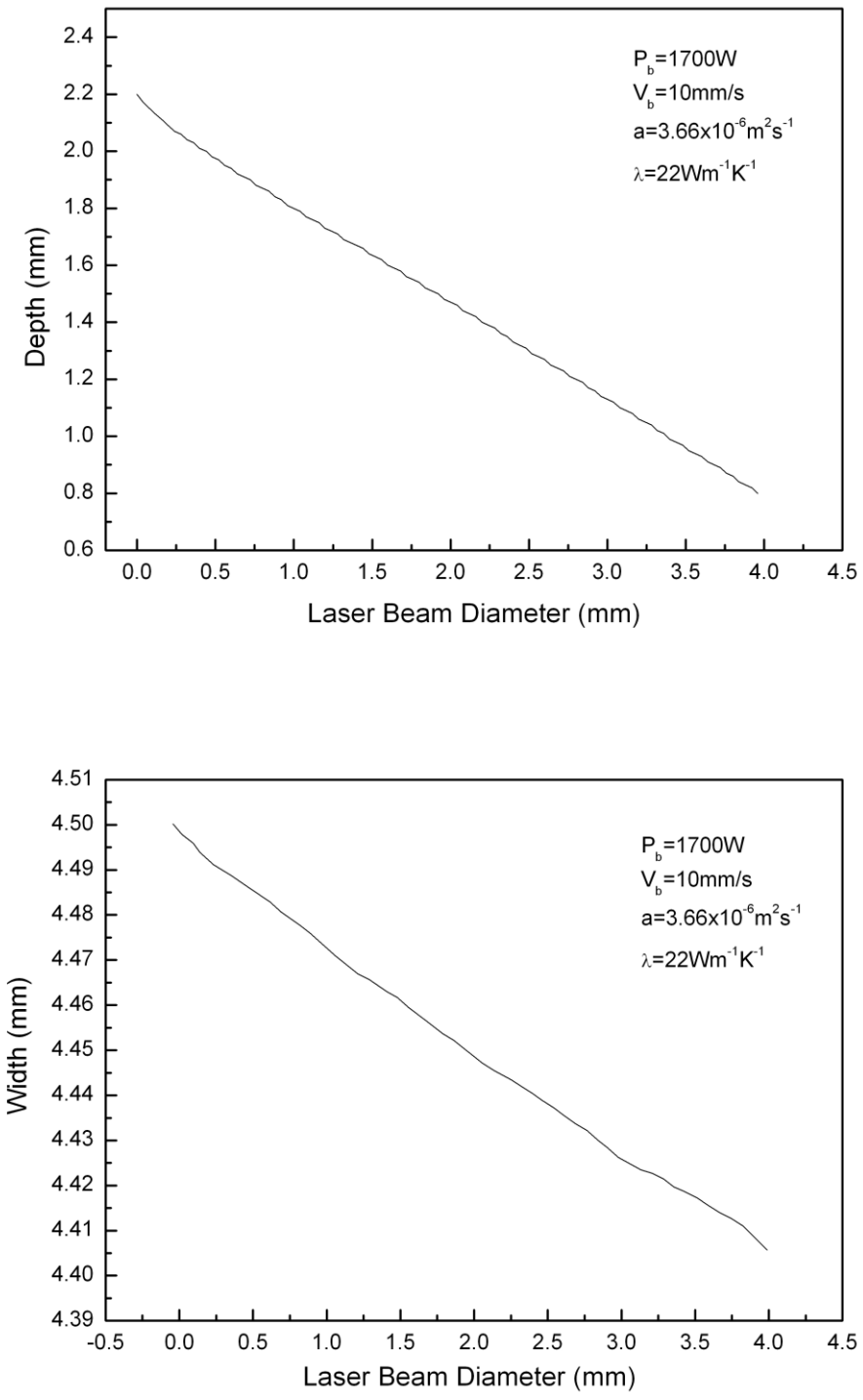

Figure 23 - Influence of processing parameters, *i.e.* laser power, velocity, and beam diameter, on melt pool shape.

4.3 Model of layer geometry

A better understanding of the geometry of the layers is crucial for the process control, as sufficient remelting is desirable for the successful laser repair process; in addition, the prediction of shape of deposit is helpful to allow planning of the deposition path. In this study, spherical cap geometry of deposited material is considered as shown in Figure 24. The volume of material deposited per unit length corresponds to the area A_1. Its magnitude, which determines the number of layers required to fill particular notch geometry, is then given by

$$A_1 = \frac{\pi D^2}{4} \times \frac{F}{v_b} \tag{15}$$

where D is the nozzle diameter, F is powder feed speed (mm/s), and v_b is laser scanning velocity.

Since the width of melt pool, *i.e.* width of the layer, can be determined by the heat source model, and A_1 can be calculated by means of Equation (15), one can readily estimate the layer height so that the number of the total passes can be predicted. The geometry of notch considered in this study is a semicircle with depth of 5 mm and curve radius of 10mm, see in Figure 25; the layer height is 0.84 mm based on the previous calculation, which means that the notch can be filled in after six passes. As 1.21 mm depth of melt pool is predicted in the previous calculation, a remelting depth of 0.37 mm can be expected for the previous layer; therefore it is a necessary condition that this value needs to be bigger than the height of equiaxed region estimated from the microstructure modelling to ensure a sufficient remelting of the previous deposit. And apparently, given the processing conditions, the number of passes can be calculated automatically with the variation of parameters. Figure 26 illustrates the thermal cycles experienced by the point on the fusion boundary of first layer; the temperature is predicted to decrease dramatically during subsequent deposition.

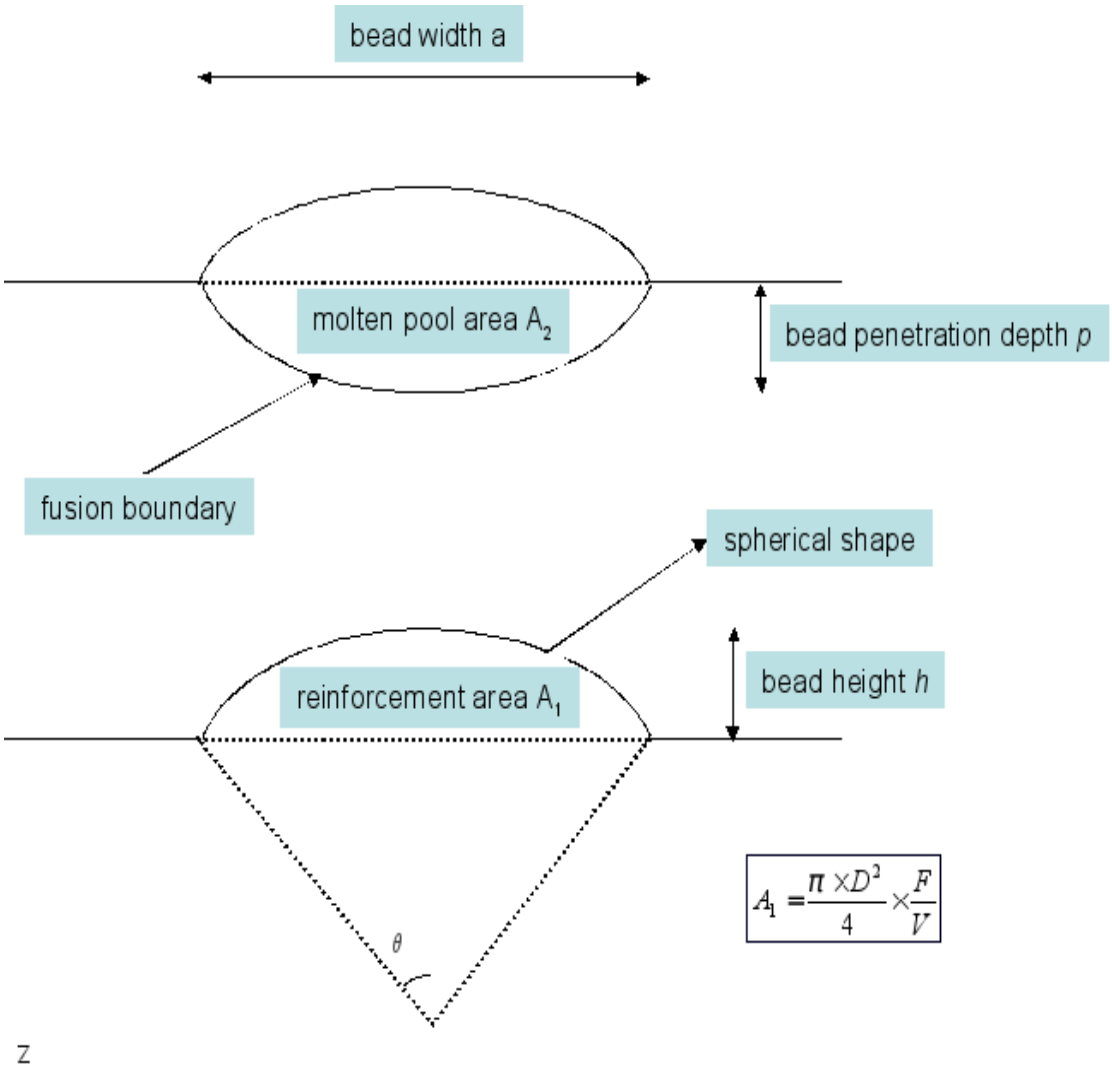

Figure 24 – The spherical cap geometry assumed in this work and the definitions of associated terms.

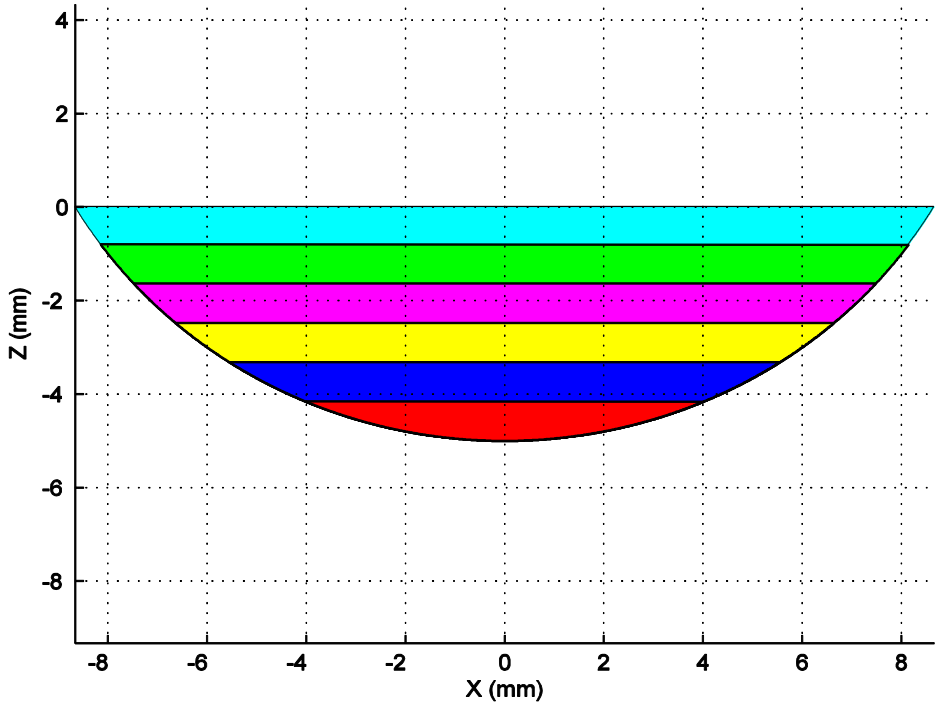

Figure 25 – Geometrical illustration of the filled notch; different colors correspond to distinct layers.

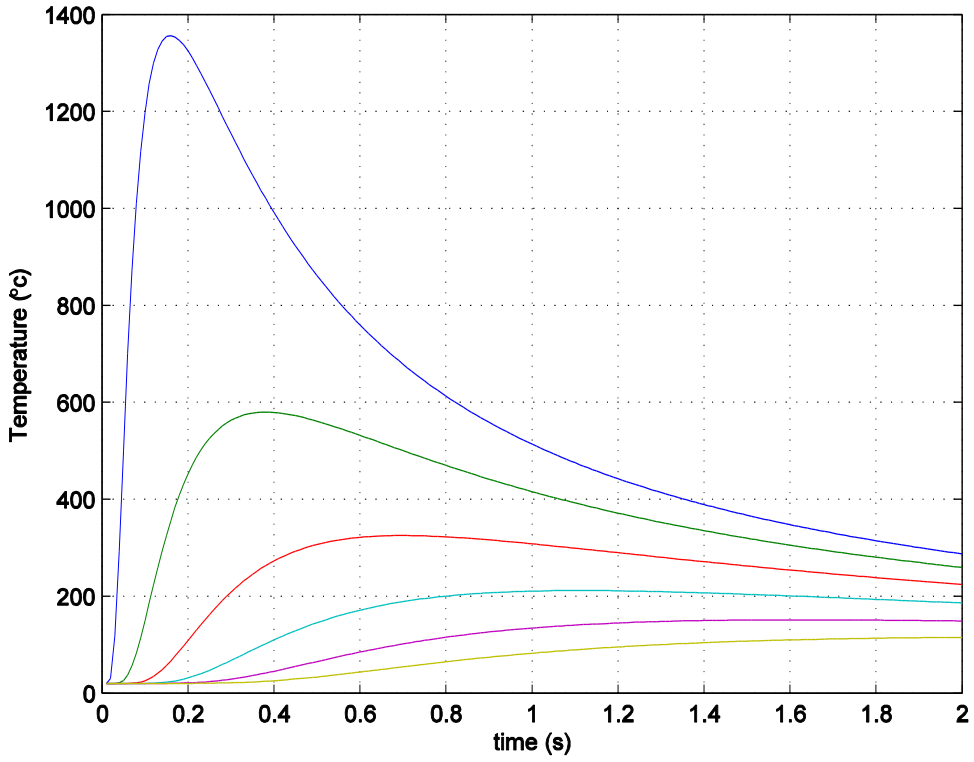

Figure 26 – Thermal cycles experienced by one point on the first layer.

4.4 Microstructure model

4.4.1 The CET model

The formation of equiaxed grains is mainly controlled by the extent of constitutional undercooling in front of the columnar dendrite front. The nucleation and growth of equiaxed grains is avoided as long as the extent of constitutional undercooling is minimal, leading to an epitaxial structure throughout the deposit. The extent has been analytically calculated by Hunt [90] and further developed by Gaumann *et al*; a parameter ϕ representing the volume fraction of equiaxed grains has been introduced using the following equation.

$$\frac{G^n}{V} = \mathrm{a}\left\{\sqrt[3]{\frac{-4\pi N_0}{3ln[1-\emptyset]}}\frac{1}{n+1}\right\}^n \tag{16}$$

$$\emptyset = 1 - \exp\left\{\frac{-4\pi N_0}{3}\left(\frac{1}{(n+1)(G^n/aV)^{1/n}}\right)^3\right\} \tag{17}$$

Where G is the thermal gradient, V is the local solidification velocity. And as determined by Gaumann for CMSX-4, the material constants $\mathrm{a} = 1.25 \times 10^6 sK^{3.4}/m$ and $\mathrm{n} = 3.4$, and the nuclei density $N_0 = 2 \times 10^5/m^3$.

And Hunt proposed that no equiaxed growth occurs when constitutional supercooling is minimal, i.e.,$\emptyset < 0.0066$, producing a fully columnar structure. And a fully equiaxed structure is generated if the volume fraction of equiaxed grains $\emptyset > 0.49$. Thereby the critical value of producing fully columnar structure can be obtained by setting the former value and then the critical condition of CET can be readily calculated based on the G^n/V ratio. Ideally the formation of equiaxed grains should be totally avoided during the deposition process as long as the CET criterion is fully achieved throughout the deposit. However, in the practical work, in order to produce

considerable height of the deposit, there is always an equiaxed region left on the surface of each pass; this is because at the top the solidification is too fast to meet the requirement of fully columnar growth. Therefore, another necessary condition for a successful single crystal repair is to make sure that the previous pass and substrate have been remelted sufficiently.

In terms of the classic laser deposition process, the values of thermal gradient and solidification velocity at the solid–liquid interface of the melt pool have been predicted through some detailed investigation and compared with the CET curve. One can see from Figure 27 that the processing parameters for laser cladding (see in the rectangular box) can be readily changed in order to make sure that the deposits grow epitaxially onto the substrate:

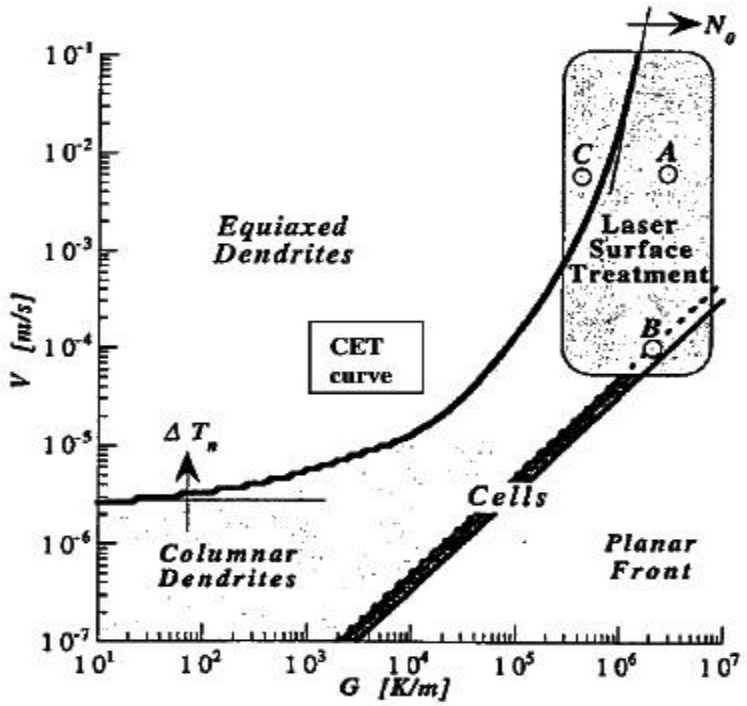

Figure 27 - Plot of solidification rate (*V)* as a function of thermal gradient *(G)* at the solidification interface for CMSX-4; the curve indicates the condition of a CET [91].

Therefore models are established to investigate the relationship between processing parameters with the solidification behavior (*G* and *V*) so that suitable conditions can be given to optimize the complicated process for the generation of epitaxial growth onto the substrate during the experimental work. Figure 28 illustrates the melting-solidification mechanisms encountered during the LMF process in this investigation. The molten pool geometry is presumed to be constant and that solidification occurs initially along the [001] orientation and then goes towards a direction given by the normal to the fusion boundary. One can see the decrease of the thermal gradient within the liquid and the rise of the local solidification rate leading to a CET on the surface of the melt pool. In our calculation the thermal gradient is produced by the thermal field induced by the laser beam within the workpiece using the thermal model in section 4.1.

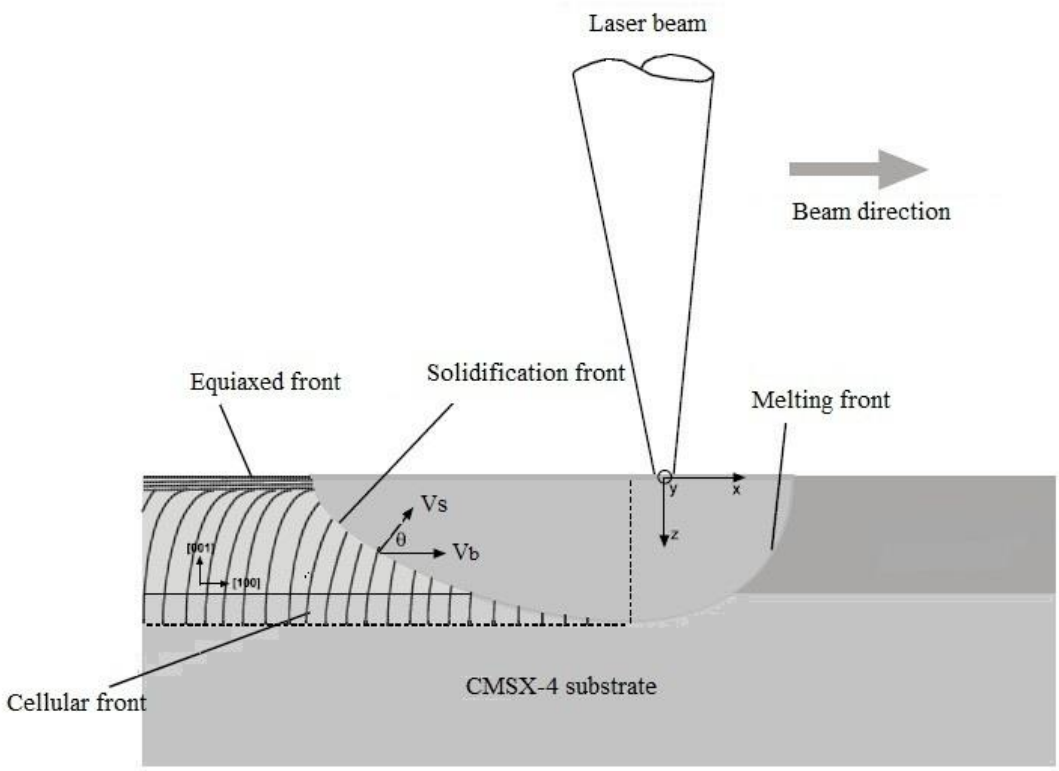

Figure 28 – Schematic illustration of the melting-solidification mechanisms encountered during the laser metal forming process

4.4.2 Solidification condition

Figure 29 (a), (b) and (c) illustrate the calculated thermal gradients at the front part of the molten pool with different laser velocities respectively; the arrow indicates the direction of thermal gradient as well as solidification growth. And it can be found that the thermal gradient may decrease along any temperature contour line from the front part to the rear part of the molten pool. In addition, at low scanning speeds the molten pool can become larger giving rise to low temperature gradients. On the other hand, the solidification rate is dominated by both scanning speed and the molten pool shape; for each specific position, the solidification velocity can be determined according to (also see in Figure 28):

$$V_s = v \times \cos\theta \tag{18}$$

where V_s is solidification rate, v is laser scanning velocity and θ is the angle of the isothermal normal against the direction of beam velocity. Figure 30 (a), (b) and (c) give the estimated shape of fusion line on the symmetry plan (y=0) using various scanning speed with 800 W laser power and 0.76 diameter of spot size respectively and Figure 31 (a), (b) and (c) illustrates the variation of calculated solidification velocity along the fusion line at the rear part of the pool accordingly. One can see that V_s goes up significantly from zero at the bottom of the melt pool to a value close to scanning speed at the rear part of the pool; and it is also worth noting that at higher scanning speeds the pool becomes flatter, therefore V_s increases slowly at the beginning of solidification and is then followed by a sharp rise. Thus the temperature gradient and solidification rate can be calculated along the fusion line in the symmetry plane (y=0), which can be used to compare with the CET curve and Gaumman's model as well in order to predict the equiaxed region and conditions of subsequent remelting.

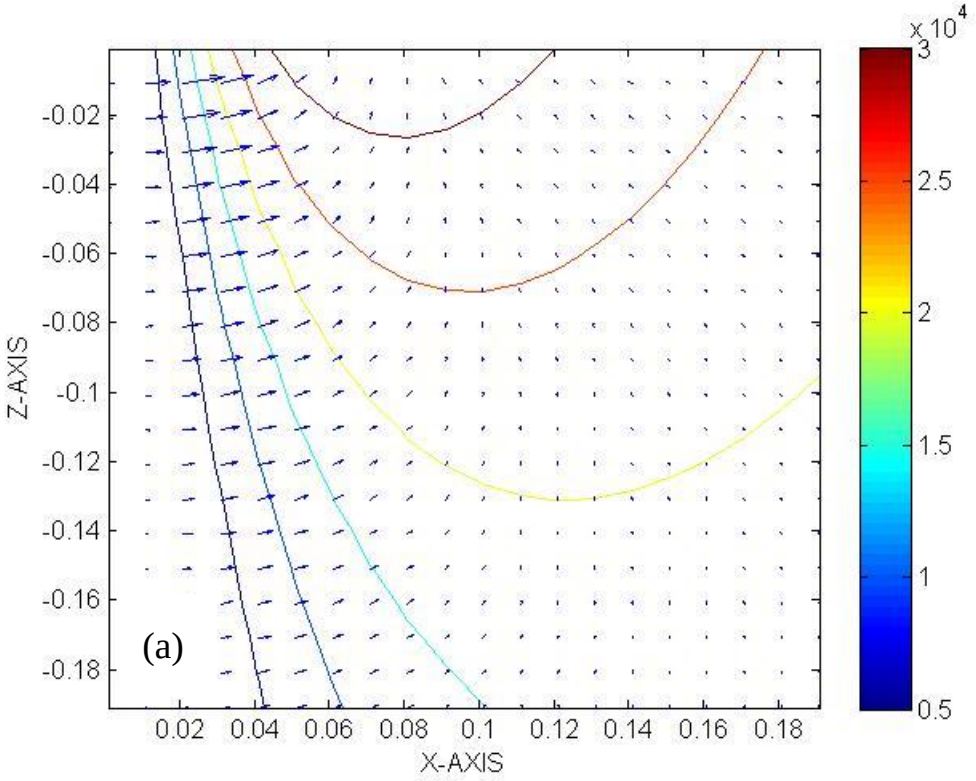
x 10^4
3
2.5
2
1.5
1
0.5
-0.02
-0.04
-0.06
-0.08
-0.1
-0.12
-0.14
-0.16
-0.18
Z-AXIS
0.02
0.04
0.06
0.08
0.1
0.12
0.14
0.16
0.18
X-AXIS
(a)

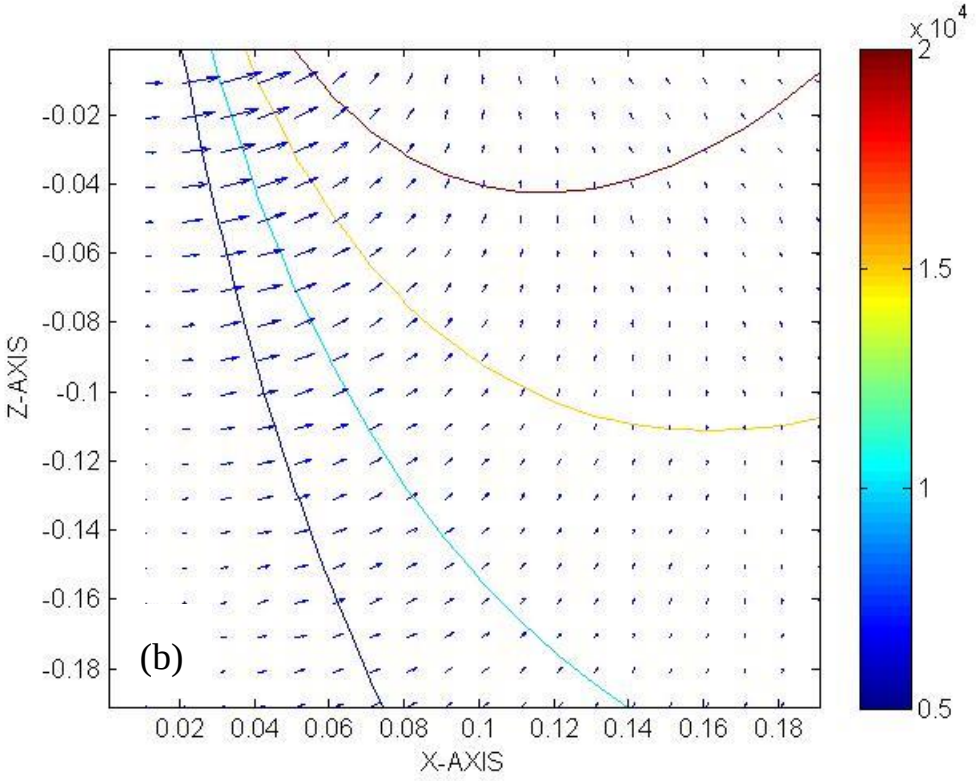
x 10^4
2
1.5
1
0.5
-0.02
-0.04
-0.06
-0.08
-0.1
-0.12
-0.14
-0.16
-0.18
Z-AXIS
0.02
0.04
0.06
0.08
0.1
0.12
0.14
0.16
0.18
X-AXIS
(b)

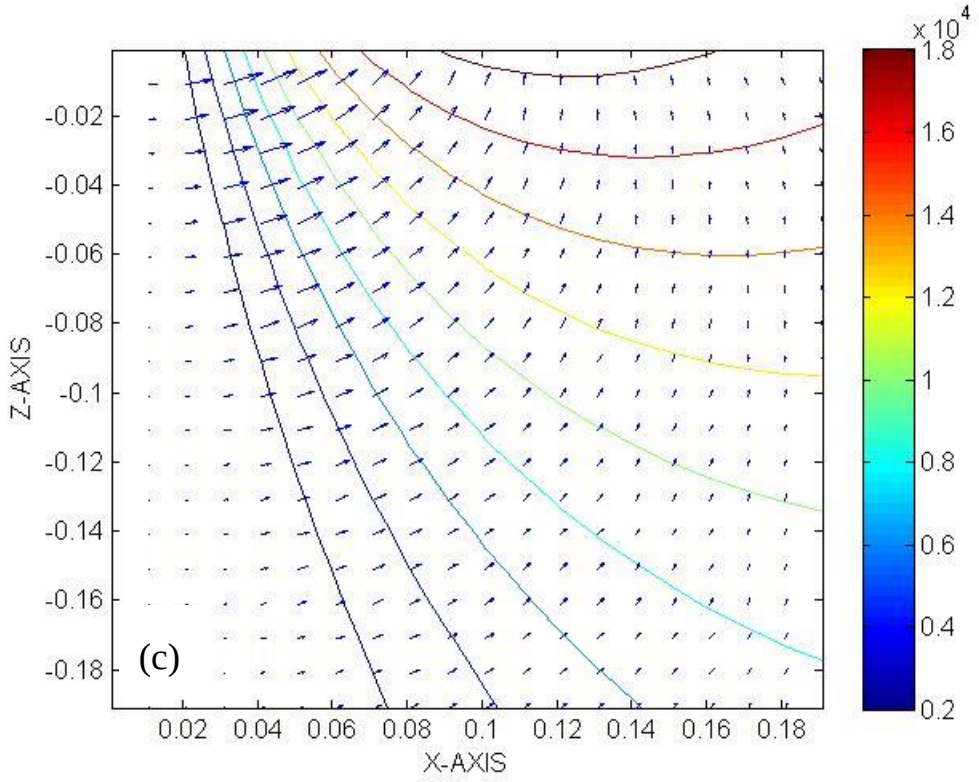

Figure 29 – Distribution of thermal gradients on the symmetry plane (y=0) with various scanning velocity, (a) 5 mm/s, (b) 10mm/s, (c) 15 mm/s. The colored lines correspond to temperature contour and the arrows indicate the gradient direction.

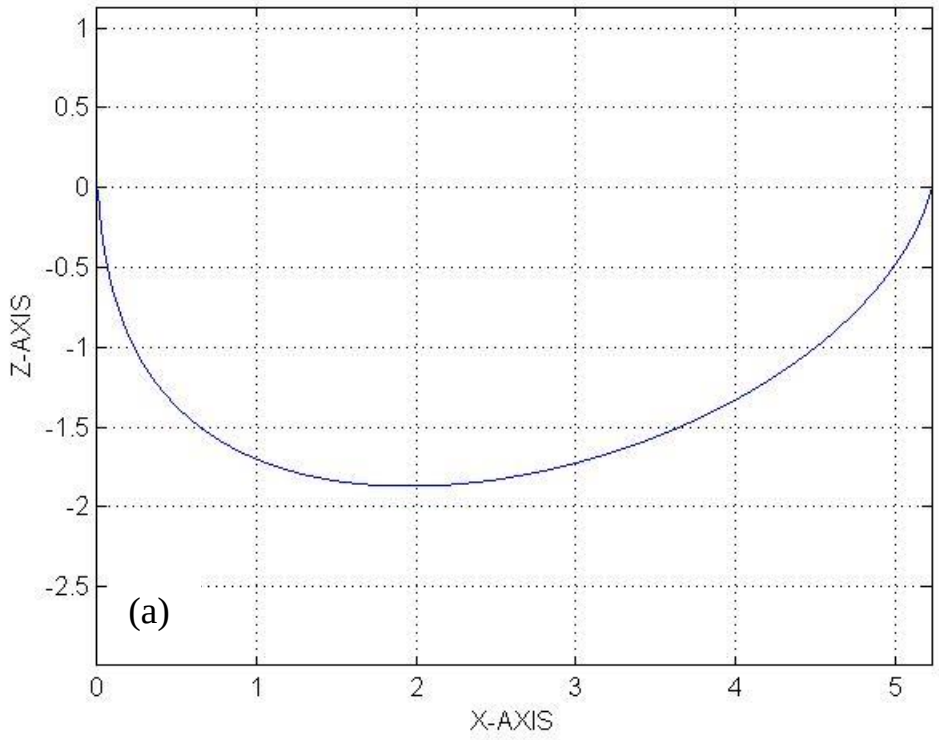

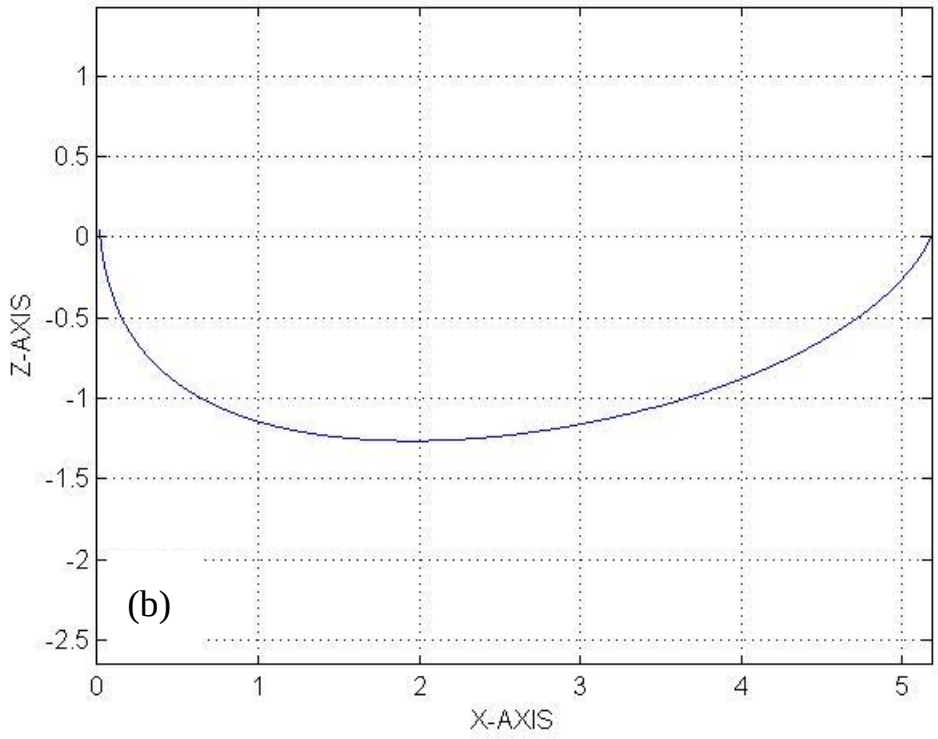

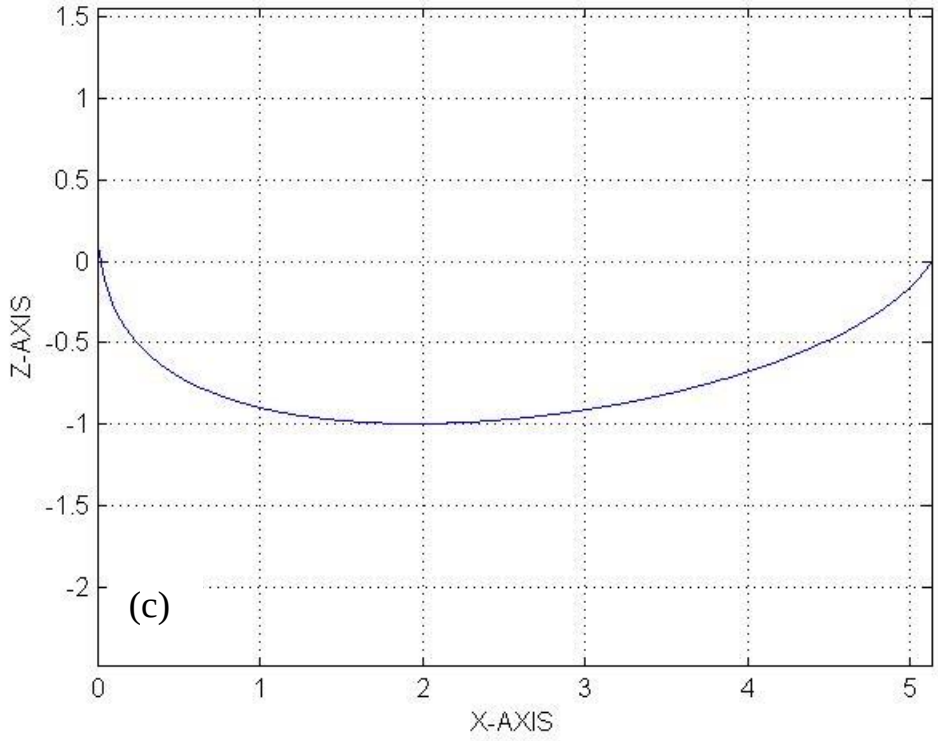

Figure 30 – Calculated melt pool shape along the fusion line on the symmetry plane (y=0) with 800 W of laser power, 0.76 diameter of spot size and various scanning velocities, (a) 5 mm/s, (b) 10 mm/s, (c) 15 mm/s.

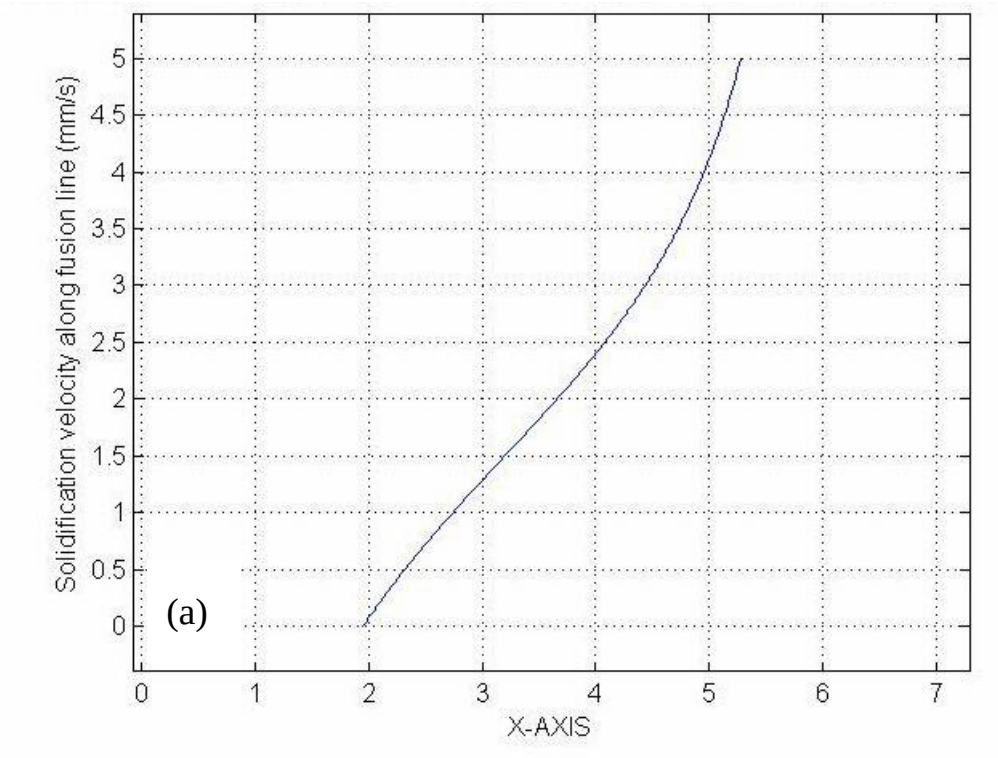
Solidification velocity along fusion line (mm/s)
X-AXIS
(a)

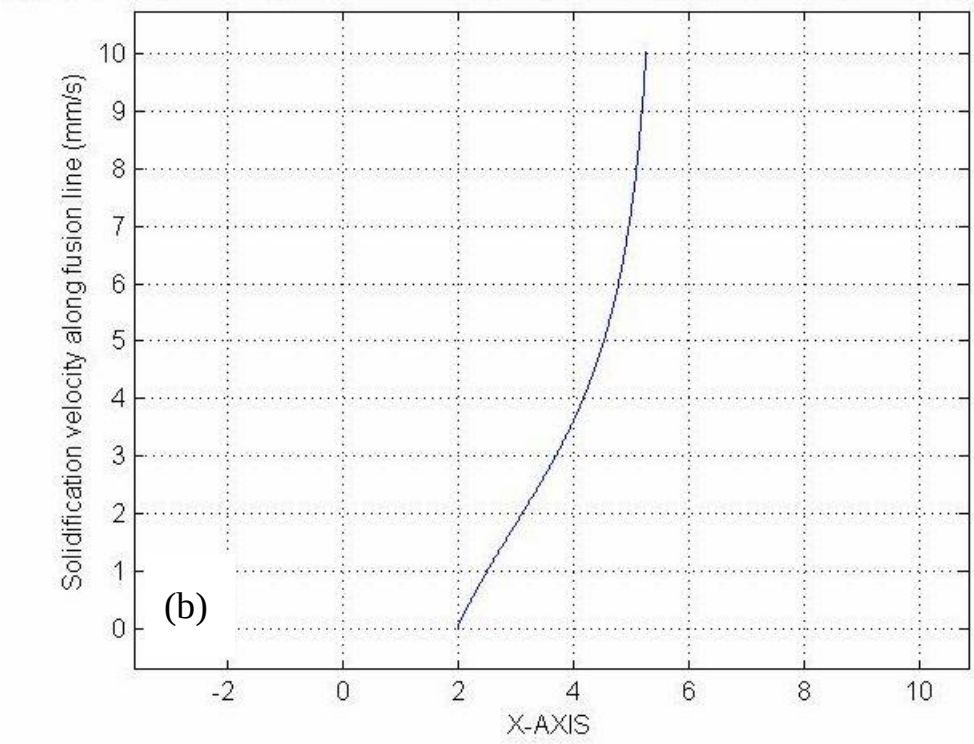
Solidification velocity along fusion line (mm/s)
X-AXIS
(b)

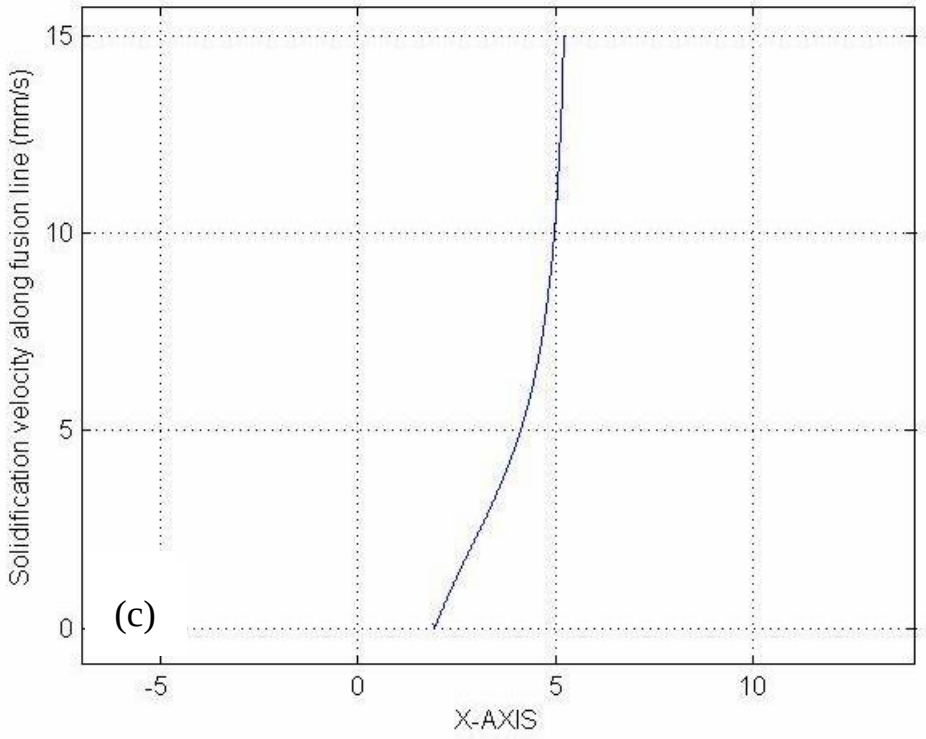

Figure 31 – Variation of solidification velocity along the fusion line on the symmetry plane (y=0) with 800 W of laser power and various scanning velocity, (a) 5 mm/s, (b) 10 mm/s, (c) 15 mm/s.

4.4.3 Modelling procedure

Following the previous models and calculation, a crucial value has been estimated for a successful E-LMF repair process, thus the solidification rate is plotted as a function of $G^{3.4}$ along the fusion line at the rear part of the melt pool as shown in Figure 32. It can be seen that the solidification rate (*V)* is the largest at the surface of the melt pool whereas thermal gradient (*G*) is the smallest and thereby most of times it is difficult to produce epitaxial growth in this region. On the other hand, at the bottom of the pool there is an opposite situation where *V* is the smallest and *G* is the largest so that epitaxial growth occurs more readily; however the deposit cannot grow epitaxially onto the substrate if *G* is not large enough to avoid CET within this region. And in most cases there is a fraction of the pool boundary where columnar microstructure can be produced; therefore the equiaxed region needs to be calculated and remelted through subsequent deposition. Thus the critical position where CET occurs can be

determined using Gaumann's crucial value. By defining the processing parameters as listed in Table 4, the height of equiaxed region within the melt pool can be readily calculated, *i.e.* 0.29 mm in this case. And as predicted using the geometrical model in section 4.3, the depth of subsequent remelting is around 0.37 mm under the same processing conditions, which means a sufficient remelting has been achieved here and hence solidification can occur epitaxially onto the substrate.

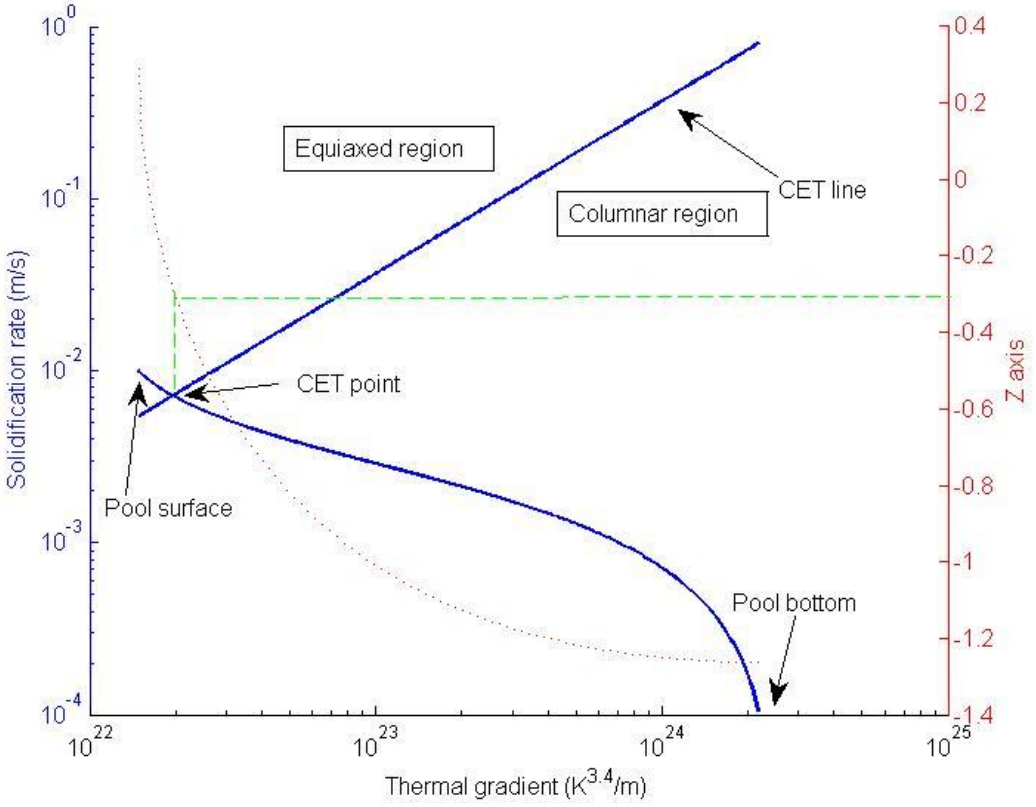

Figure 32 - Variation of the solidification rate as a function of $G^{3.4}$ along fusion line (lower blue curve) with processing conditions listed in Table 4. The upper blue line corresponds to the CET critical condition where $G^{3.4}/V = 2.7 \times 10^{24}$ $(K^{3.4}m^{-4.4}s)$; below the CET line there is a columnar region whereas an equiaxed region can be found above this line. The red dotted line shows that the thermal gradient varies with the molten pool depth along the fusion line (see in right Y axis). The green dashed line indicates the critical position where CET occurs.

4.4.4 Results and discussion

This critical value can also be applied for different laser processing conditions for the purpose of predicting the probability of forming equiaxed grains. Figure 33 (a) and (b) show the influence of laser power on the calculated height of equiaxed region. Combined with Figure 32, it can be found that a decrease in laser power can reduce the possibility of generation of equiaxed grains; in particular given certain laser speed (relative higher speed) and spot size, the equiaxed region is rather limited when the power is as low as 600 W. This is because the molten pool is relatively small and thermal gradients are quite sharp with low power and therefore epitaxial growth can occur readily. Therefore it becomes obvious that the CET might be avoided during the whole process if the power is lower than around 600 W. However at high power the melt pool is so large and hot resulting in a low temperature gradient that epitaxial growth is avoided and a fully equiaxed microstructure can be found if the power is high enough. A percentage of 30% of equiaxed grains is found to be in the generated microstructure when laser power comes to 1000 W (see in Figure 33 (b)). In terms of the influence of beam velocity, it becomes complicated; since with beam velocity increasing, the melt pool becomes smaller resulting in a higher thermal gradient and increase in the solidification rate as well. And it has been found from the calculation that given certain laser power (800 W) at a scanning speed of 3 mm/s, it is the most possible to produce equiaxed grains. This is because the beam velocity produces a main effect on the solidification rate rather than thermal gradient at a low value, *i.e.* lower than 3 mm/s, leading to a decrease of G/V ratio (see in Figure 34 (a) and (b)). However, the beam velocity mainly dominates the thermal gradient at higher value; in other words, the increase in beam velocity can result in a substantial rise in G but a relatively small variation in V. (see in Figure 34 (b), (c) and (d)); therefore the equiaxed region can be gradually reduced with increasing beam velocity. Consequentially, the G/V ratio is increased and hence the region of equiaxed grains is reduced.

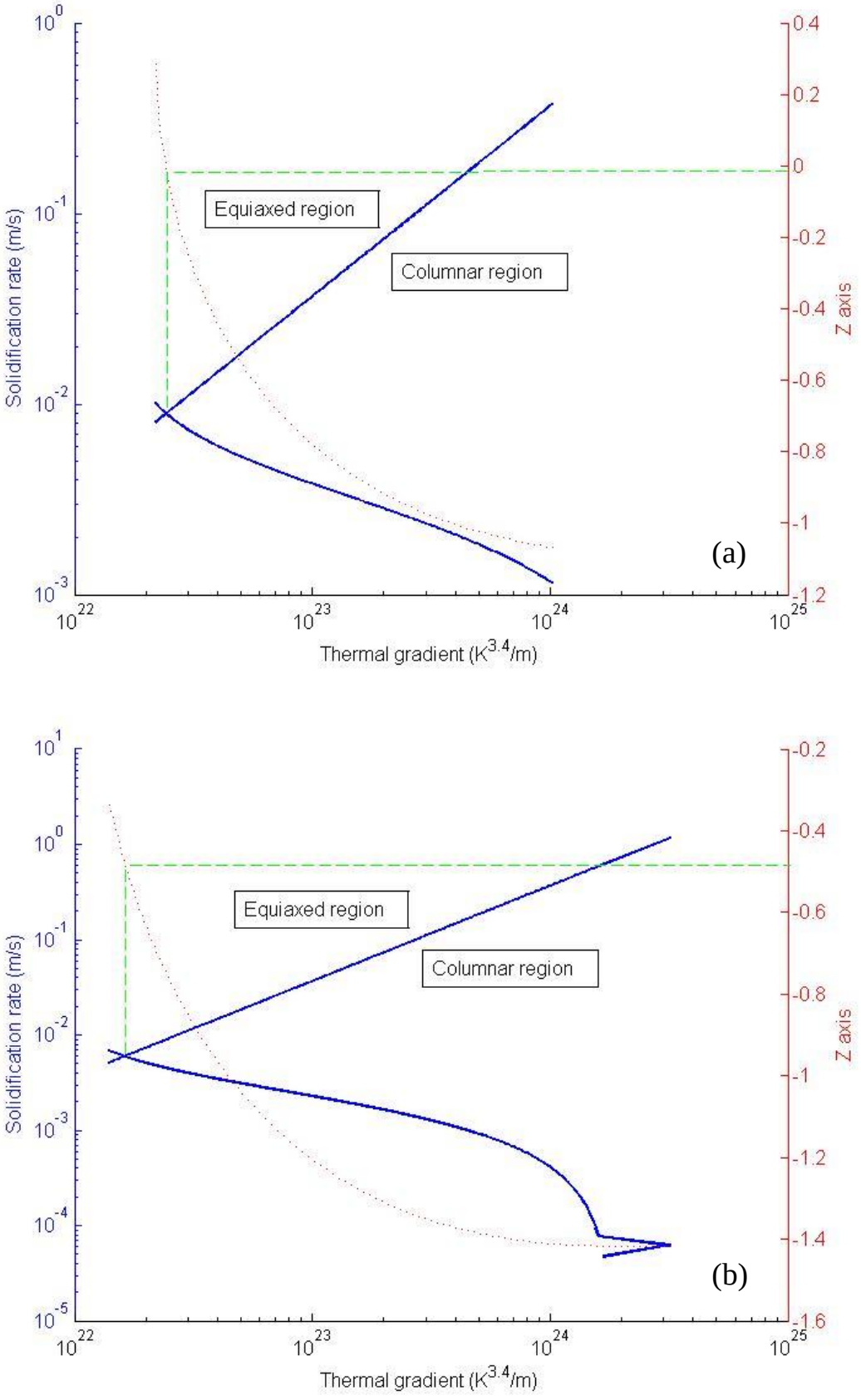

Figure 33 – Influence of laser power on the height of equiaxed region with 10 mm/s laser velocity: (a) 600 W and (b) 1000 W.

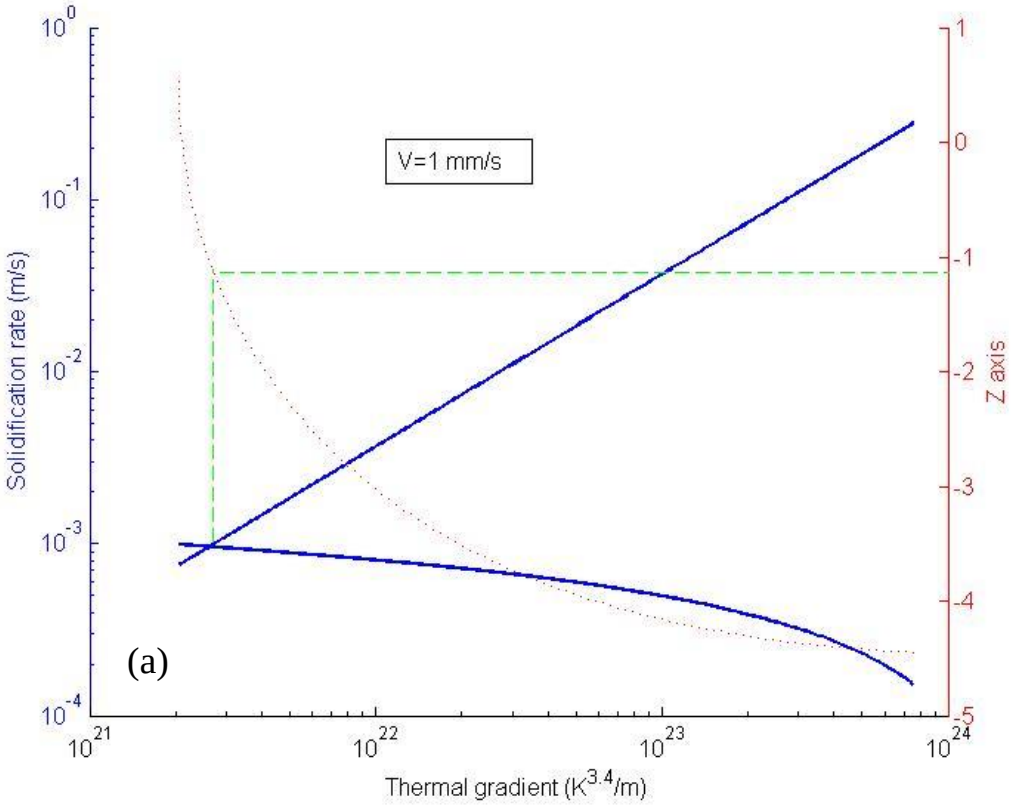
V=1 mm/s
Solidification rate (m/s)
Z axis
Thermal gradient (K^3.4/m)
(a)

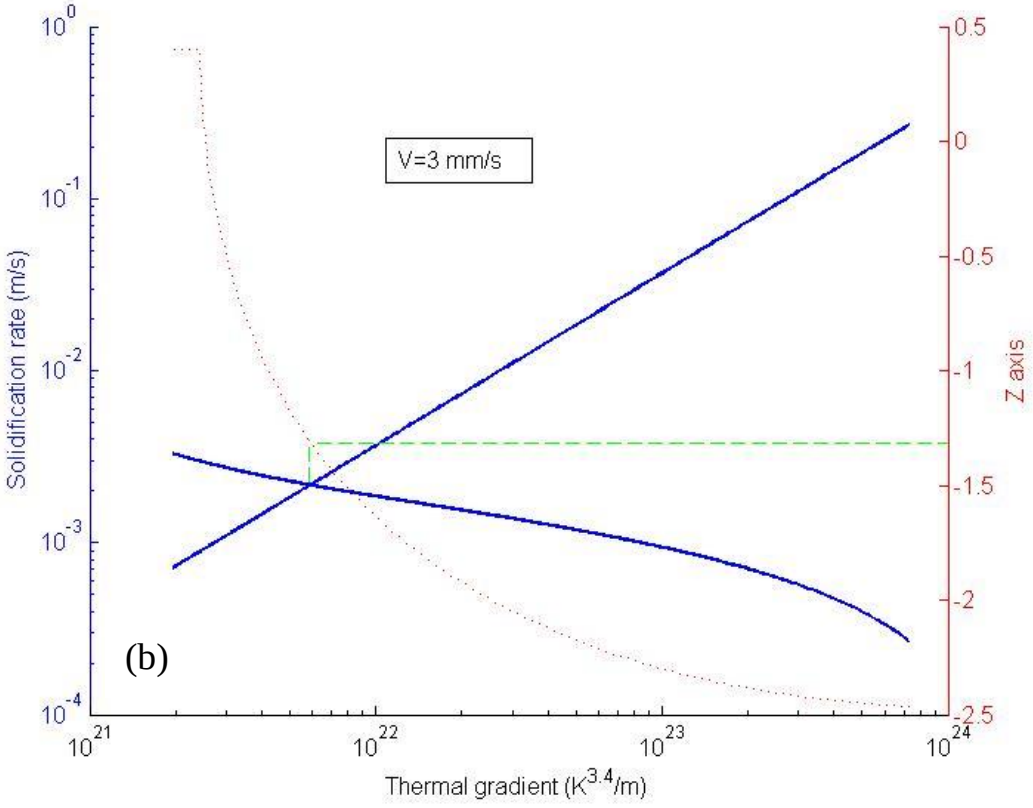
V=3 mm/s
Solidification rate (m/s)
Z axis
Thermal gradient (K^3.4/m)
(b)

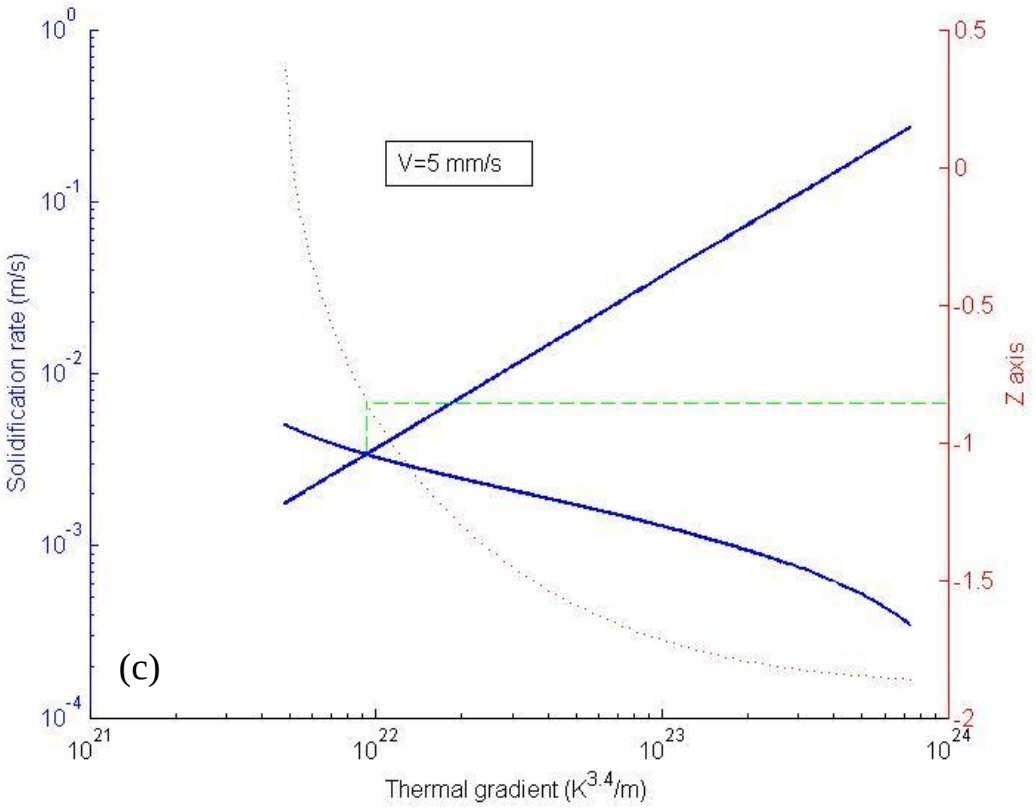

Figure 34 – Effect of beam velocity on the height of equiaxed region with 800 W laser power: (a) 1 mm/s, (b) 3 mm/s, (c) 5 mm/s and (d) 7 mm/s.

4.5 Summary

Coupled with the power powder interaction model developed in chapter 3, the heat transfer within the molten pool during LMF (laser metal forming process) has been studied using a modified Rosenthal model with an emphasis on the impact of processing parameters on the melt pool shape, such as laser energy, scanning speed and spot diameter. As a result, for given processing conditions, a number of parameters during the deposition process can be predicted such as the temperature distribution within the workpiece and the melt pool shape. Results also indicate that the pool indeed has a close relationship with the processing parameters and especially it is more sensitive at lower power energy and scanning velocity. Moreover, combined with the thermal model, a layer geometrical model has been employed to predict the layer width, deposition height as well as the number of passes required for the laser process. In addition, the remelting depth has been estimated which is crucial for the determination if a successful repair can be achieved. Furthermore, the previous two models have been coupled with the improved CET model so that processing parameters are connected with solidification conditions (thermal gradients and solidification velocity) and hence the generated microstructure. Results show that the model can predict the tendency for the generation of equiaxed grains using various processing parameters. Specifically the formation of equiaxed grain can be generally reduced during a laser repair process by using a lower power and high travel speed. Due to the complicated influence of laser speed on solidification, the worst condition for epitaxial growth occurs at a travel velocity of 3 mm/s. Therefore careful process control is a necessity for a successful single crystal repair; and a careful choice of lower power value and suitable beam velocity are the crucial conditions. Finally some processing conditions are given for the optimisation of a LMF process in order to generate an epitaxial deposit onto the substrate during the experimental work. Nevertheless, the model needs to be further developed and experimental work is required to validate and optimise the model.

Chapter 5 Conclusions and Future work

5.1 Conclusions

In this project, an in-house Matlab code for the analytical modeling of the LMF process has been developed. An analytical model has been proposed for better understanding of the mechanism of the interaction between laser beam and powder stream. By means of the model, the laser attenuation by a powder stream was estimated and the laser intensity distribution on the surface of the substrate both prior to and after the powder delivery was presented. The obtained results show that the laser efficiency is related to the powder feed rate, the feeding angle as well as gas flow rate; for example, more attenuation of power can be expected with the increase of powder feed rate and feeding angle and decrease of gas flow rate. Thus the powder preheating temperature will be subsequently influenced. In the meantime, the thermal field of the powder particles when reaching the surface of the substrate was obtained based on the heat equilibrium principle. As the maximum temperature of powder particles is predicted, the calculations can also show a feasibility to estimate whether the powder particles during flight are melted or not under specific conditions. It is considered to be an essential condition to decrease the nucleation possibility of equiaxed grains if powder particles are still kept solid state when arriving at the surface of the substrate. The model proposed in this study is potentially useful for optimisation of the complicated repair process and hence a better control of the subsequent laser induced molten pool. Then coupled with the power powder interaction model developed, the heat transfer within the melt pool during the LMF process using Ar shielding gas has been studied by means of a modified Rosenthal's model with an emphasis on the impact of processing parameters on the melt pool shape, such as laser energy, travelling speed and spot diameter. As a result, for given processing conditions, a number of parameters during the deposition process can be predicted such as the temperature distribution within the workpiece and the melt pool shape. Results also indicate that the pool indeed has a close relationship with the

processing parameters and especially it is more sensitive at lower power energy and scanning velocity. Moreover, combined with the thermal model, a layer geometrical model has been employed to predict the layer width, deposition height as well as the number of passes required for the laser process. In addition, the remelting depth has been estimated which is crucial for the determination if a successful repair can be achieved. Furthermore, the previous two models have been coupled with the CET model so that processing parameters are connected with solidification conditions (thermal gradients and solidification velocity) and hence the generated microstructure. Results show that it is feasible for the model to predict the tendency for the generation of equiaxed grains as well as the fraction of columnar microstructure using various processing parameters. The extent of formation of equiaxed grains is significantly higher with high laser power and low laser scanning speed. Moreover results indicate that at each diameter and power of the laser beam the model is able to predict the limiting value of the beam travelling velocity so as to ensure epitaxial growth. It is also found that accurate process control is a necessity for a successful single crystal repair; and a careful choice of lower power value and suitable beam velocity are the crucial conditions. Finally some processing conditions are given for further optimisation of the repair process in order to produce an epitaxial deposit onto the substrate during the experimental work.

5.2 Future research

In future research, experimental work can be designed to calibrate the model proposed in this study and potentially optimise parameters; This will be in terms of mass absorption, power attenuation, layer deposited thickness, temperature distribution within the substrate and deposited material (if measurable), microstructure produced and chemical composition map caused by the whole process. A high speed camera is needed to view melt pools in the LMF process, and their evolution with incremental layers as well as the geometry of the deposited layers. Thermocouples are required to quantify the temperature distribution. SEM is needed to look at the microstructure and chemical compositions generated in the process. Ultimately the analytical model should be optimised and developed to accurately produce the new processing window for epitaxial repair for turbine blades.

Concerning the modelling work, the analytical model still needs to be improved and developed; for example, fluid flow can be introduced into the model in terms of modeling the melt pool shape and local solidification conditions. Another possible future job is that numerical simulation of laser repair can be developed in order to provide more accurate results. This can be achieved by using relevant FEM software. The complicated relationship between laser beam and powder stream can also be involved in the numerical model starting from the analytical model established in this study. In terms of microstructure modelling, the cellular automaton-finite element (*CAFE)* approach could be employed to predict the complicated mechanisms of nucleation and growth of dendritic grains so as to give a better understanding of the formation of equiaxed grains during the solidification process and for comparison with the analytical CET model.

References

[1] Gandin, Ch.-A., J.-L. Desbiolles, M. Rappaz and Ph. Thévoz, A three-dimensional cellular automaton-finite element model for the prediction of solidification grain structures. *Metallurgical and Materials Transactions A*, 1999, 30A: p. 3153-3165.

[2] M. Gaumann, Epitaxial laser metal forming of a single crystal superalloy, PhD thesis, the Swiss Federal Institute of Technology Lausanne (EPFL), 1999.

[3] 'Superalloys 2008', edited R.C. Reed, K.A. Green, P. Caron, T.P. Gabb, M.G. Fahrmann, E.S. Huron and S.R. Woodard, The Minerals, Metals, Metals, and Materials Society, Warrendale PA, USA (2008).

[4] T. Sims, 'A History of Superalloy Metallurgy for Superalloy Metallurgists', General Electric Company Schenectary, New York 12345.

[5] W. Liu and J. DuPont. Effects of melt-pool geometry on crystal growth and microstructure development in laser surface-melted superalloy single crystals. *Acta Materialia*, 52:4833–4847, 2004.

[6] H. Bhadeshia, Nickel Based Superalloys, Cambridge University, (1995), viewed 28thApril2009.

[7] R. C. Reed, T. Tao and N. Warnken, Alloy-by-design:application to nickel based single crystal superalloys, *Acta Materialia*, Volume 57, Issue 19, November 2009, Pages 5898-5913

[8] E. Sarath K Menon, 'Microstructural Characterization of Nickel-Based Superalloys' UES Inc., 4401 Dayton-Xenia Road, Dayton, OH 45432-1894, USA

[9] M. Donachie and S. Donachie. Superalloys: A Technical Guide. ASM International, 2nd edition, 2002.

[10] W. J. Boesch and J.S. Slaney, 'Preventing Sigma Phase Embrittlement in Nickel-base Superalloys', *Metal Progress 86*, 109-111, (1964).

[11] Y. Murata, S. Miyazaki, M. Morinaga and R. Hashizume, Hot corrosion resistance and high strength nickel-based single crystal and directionally-solidified superalloys developed by the d-electrons concept, in Superalloys 1996, edited R.D. Kissinger, D.J .Anton, A.D. Cetel, M.V. Nathal, T.M. Pollock and D.A. Woodford, (Warrendale, PA, USA: *The Minerals, Metals and Materials Society (TMS)*, (1996),61-70).

[12] J. Vitek, S. A. David, and S. Babu. Welding and weld repair of single crystal gas turbine alloys. *Material Science and Engineering*, TN37831:6096, 2008.

[13] S. David, J.M. Vitek, S.S. Babu, L.A. Boatner, and R.W. Reed. Sci Tecnology Weld Joining, 2:79–88, 1997.

[14] Brown, C.O, E.M. Breinan and B.H. Kear, US Patent 4,323,756. 1982: United State.

[15] Gremaud, M., J.-D. Wagnière, A. Zryd and W. Kurz, Laser Metal Forming :Process Fundamentals. *Surface Engineering*, 1996, 12(3): p. 251-259.

[16] Hofmeister, W., M. Wert, J.A. Philliber, M. Griffith and M. Ensz, Investigating solidification with the laser-engineered net shaping (LENSTM) Process. JOM, 1999. 51(7).

[17] Griffith, M.L., M.E. Schlienger, L.D. Harwell, M.S. Oliver, M.D. Baldwin, M.T. Ensz, M. Essien, J. Brooks, C.V. Robino, J.E. Smurgeresky, W.H. Hofmeister, M.J. Wert and D.V. Nelson, Understanding thermal behavior in the LENS process. *Materals and Design*, 1999. 20: p. 107-113.

[18] Grujicic, M., G. Gao and R.S. Figliola, Computer simulation of the evolutions of solidification microstructure in the LENS rapid fabrication process. *Applied Surface Science*, 2001. 183: p. 43-57.

[19] Schwendner, K.I., R. Banerjee, P.C. Collins, C.A. Brice and H.L. Fraser, Direct laser deposition of alloys from elemental powder blends. *Scripta Materialia*, 2001. 45: p. 1123-1129.

[20] Unocic, R.R. and J.N. Dupont, Composition control in the direct laser-deposition process. *Metallurgical and Materials Transactions B*, 2003. 34B: p. 439-445.

[21] Lewis, Gary K. and Eric Schlienger, Practical considerations and capabilities for laser assisted direct metal deposition. *Materials and Design*, 2000. 21: p. 417-423.

[22] Watkins, K.G. Achieving the potential of direct fabrication with lasers. in International Conferance on Laser Assisted Net Shaping (LANE 2001). 2001. Erlangen: Verlag Bamberg.

[23] Srivastava, D., Microstructural characterization of the γ -TiAl alloy samples

fabricated by direct laser fabrication rapid prototype technique. Bull. *Mater. Sci.*, 2002. 25(7): p.619-633.

[24] Stimper, B., Using laser power cladding to build up worn compressor blade tips, MTU Aero Engines: Munich.

[25] M. Gaumann, C. Benzencon, P. Canalis, and W. Kurz. Single crystal laser deposition of superalloys: processing-microstructure maps. *Acta Materialia*, 49:1051–1062, 2000.

[26] P. Peyre, P. Aubry, R. Fabbro, R. Neveu, and A. Longuet3. Analytical and numerical modeling of the direct metal deposition laser process, *Journal of Physics D: Applied physics*, 41, 2008.

[27] H. Qi and J. Mazumder, Numerical simulation of heat transfer and fluid flow in coaxial laser cladding process for direct metal deposition. *Journal of applied physics*, 100:024903–11, 2006.

[28] W.P. Liu and J.N. DuPont, Fabricability of sx nickel-base alloy deposits by direct laser deposition, *Metallurgical and Materials Transactions A*, 36:3397–3406, 2005.

[29] H. Qi, M. Azer, and P. Singh, Adaptive toolpath deposition method for laser net shape manufacturing and repair of turbine compressor airfoils, *The International Journal of Advanced Manufacturing Technology*, 2009.

[30] M. Gaumann, S. Henry, F. Cleton, J. D. Wagniere, and W. Kurz. Epitaxial laser metal forming: analysis of microstructure formation. *Material Science and Engineering*, A271:232–241, 1999.

[31] J. Drezet, S. Pellerin, C. Bezenon, and S. Mokadem, Modelling the marangoni convection in laser heat treatment. *Journal of Physics*, 120:299–306, 2004.

[32] S. Roy S. Kumara. Development of a theoretical process map for laser cladding using two dimensional conduction heat transfer model. *Computational Materials Science*, 41:457–466, 2008.

[33] Y. Huang, G. Liang, J. Su, and Li J. Interaction between laser beam and powder stream in the process of laser cladding with powder feeding. *Material Science and Engineering*, 13:47–56, 2005.

[34] U. Oliveria, V. Ocelik, and J. Hosson, Analysis of coaxial laser cladding processing conditions. *Surface and Coatings Tecnology*, 197:127–136, 2005.

[35] A. Pinkerton, M. Karadge, W. Syed, and L. Li. Thermal and microstructural aspects of the laser direct metal deposition of waspaloy, *Journal of Laser Applications*, 18, number3, 2006.

[36] Steen, W.M., V.M. Weerasinghe and P. Monson, in High Power Lasers and Their Industrial Applications, D. Schuöcker, Editor. 1986, SPIE: Bellingham, WA. p. 226-234.

[37] Kar, A. and J. Mazumder, One-dimensional diffusion model for extended solid solution in laser cladding. *Journal of Applied Physics*, 1987. 61(7): p. 2645-2655.

[38] Deus, A.M. and J. Mazumder. Two-dimensional thermo-mechanical finite element model for laser cladding, 1996, Orlando, Florida: Laser Institute of America.

[39] Hoadley, A.F.A. and M. Rappaz, A thermal model of laser cladding by powder injection. *Metallurgical and Materials Transactions B*, 1992. 23B: p. 631-642.

[40] Ollier, B., N. Pirch, E.W. Kreutz and H. Schlüter, in Laser treatment of materials, B.L. Mordike, Editor. 1992, DGM: Oberursel. p. 687-692.

[41] Vilar, R., Laser alloying and laser cladding. *Materials Science Forum*, 1999. 301: p.229-252.

[42] Roósz, A., I. Teleszky and F.Boros, Solidification of Al-6Zn-2Mg alloy after laser remelting. *Materials Science and Engineering*, 1993. A173: p. 351 - 355.

[43] El-Batahgy, A.-M., Effect of laser welding parameters on fusion zone shape and solidification structure of austenitic stainless steels. *Materials Letters*, 1997. 32: p. 155 - 163.

[44] Kim, Jae-Do and Yun Peng, Melt pool shape and dilution of laser caldding with wire feeding. *Journal of Materials Processing Technology*, 2000. 104: p. 284-293.

[45] Schanwald, L.P. Two powder stream diagnostics for laser deposition processes. in *ICALEO' 95*. 1995.

[46] Griffith, M.L., M.E. Schlienger, L.D. Harwell, M.S. Oliver, M.D. Baldwin, M.T. Ensz, M. Essien, J. Brooks, C.V. Robino, J.E. Smurgeresky, W.H. Hofmeister, M.J. Wert and D.V. Nelson, Understanding thermal behavior in the LENS process. *Materals and Design*, 1999, 20: p. 107-113.

[47] Lim, L.C., Q. Ming and Z.D. Chen, Microstructures of laser-clad nickel based hardfacing alloys. *Surface and coatings Technology*, 1998, 106: p. 183-192.

[48] P.S. Mohanty, and J. Mazumder, Solidification behavior and microstructural evolution during laser beam-material interaction. *Metall. Mater. Trans. B*, 1998, 29B: p. 1269- 1279.

[49] W.P. Liu and J.N. DuPont, Fabricability of sx nickel-base alloy deposits by direct laser deposition, *Metallurgical and Materials Transactions A*, 36:3397–3406, 2005.

[50] S. Mokadem, C. Bezencon, A. Hauert, A. Jacot, and W. Kurz, Laser repair of superalloy single crystals with varying substrate orientations, *Metallurgical and Materials Transactions A*, 38:1500–1510, 2007.

[51] J. D. Hunt, Steady state columnar and equiaxed growth of dendrites and eutectic, *Material Science and Engineering*, 65:75–83, 1984.

[52] M. Gaumann, R. Trivedi, and W. Kurz, Nucleation ahead of the advancing interface in directional solidification. *Material science and engineering*, A226-228:763–769, 1997.

[53] M. Gaumann, C. Benzencon, P. Canalis, and W. Kurz. Single crystal laser deposition of superalloys: processing-microstructure maps. *Acta Materialia*, 49:1051–1062, 2000.

[54] Gandin, A and M. Rappaz, A coupled finite element-cellular automaton model for the prediction of dendritic grain structures in solidification processes, *Acta Materiala*, 1994. 42(7): p. 2233-2246.

[55] Vandyoussefi, M. and A.L. Greer, Application of cellular automaton-finite element model to the grain refinement of directionally solidified Al-4.15 wt.% Mg alloys, *Acta Materiala*, 2002, 50: p. 1693-1705.

[56] S. Roy and S. Kumara. Development of theoretical process maps to study the role of powder preheating in laser cladding. *Computational Materials Science*, 37:425–433, 2006.

[57] Y. Fu, A. Loredo, B. Martin, and A. Vannes, A theoretical model for laser and powder particles interaction during laser cladding. *Journal of Materials Processing Technology*, 128:106–112, 2002.

[58] E. Toyserkani, A. Khajepour, and S.F. Corbin. 3D finite element modeling of laser cladding by powder deposition: Effects of laser pulse shaping on the process. *Journal of Optics and Lasers in Engineering*, 41(6):849–867, 2004.

[59] Gremaud, M., J.D. Wagnière, A. Zryd and W. Kurz, Laser Metal Forming: Process Fundamentals. *Surface Engineering*, 1996, 12(3): p. 251-259.

[60] Picasso, M, C.F. Marsden, J.-D. Wagnière, A. Frenk and M. Rappaz, A simple but realistic model for laser cladding, *Metallurgical and Materials Transactions B*, 1994. 25: p.281-291.

[61] Weerasinghe, V.M. and W.M. Steen, Laser surface cladding, in Laser surface treatments of metals, C.W. Draper and P. Mazzoldi, Editors. 1986, Martinus Nijhof: Dordrecht. p. 360-387.

[62] Lin. J, Numerical simulation of the focused powder streams in coaxial laser cladding *J. Mater. Process.Technol*, 105:17-23, 2000.

[63] Hu. X, Chen. Z, Wu. X, Nonferrous Metals 7 136-9.

[64] Astafieva. L, Babenko. V, quant. Spectrosc. Radiat. Transfer. 63 459-68.

[65] Ashish. T, Chris. L and Henk. L, Acta, 388 183-97.

[66] Zhang. Q, Liu. W, Yang. S and Zhong. M, laser Technol, 26 170-3.

[67] Pinkerton. A. J and Li. L. Modelling powder concentration distribution from a coaxial deposition nozzle for laser-based rapid tooling, *Trans. ASME J. Manuf. Sci. Eng.* 126 33-41.

[68] Pinkerton A J and Li L 2002 A verified model of the behaviour of the axial powder stream concentration from a coaxial laser cladding nozzle *Proc. 21st Int. Cong. on Applications of Lasers and Electro-optics (Scottsdale, AZ, USA)* (Orlando: Laser Institute of America) CD

[69] Rosenthal, D, Mathematical theory of heat distribution during welding and cutting, *Welding Journal*, 1941. 20(5): p. 220s-234s.

[70] Mazumder, J. and W.M. Steen, Heat transfer model for cw laser material processing, *Journal of Applied Physics*, 1980. 51(2): p. 941-947.

[71] Kasuya. T and N. Shimoda, Stefan problem for a finite liquid phase and its application to laser or electron beam welding, *Journal of Applied Physics*, 1997. 82(8):

p. 3672.

[72] Houldcroft, P. T., Dilution and uniformity in aluminum alloy weld beads, *British Welding Journal*, 1954. 1: p. 468.

[73] Pumphrey, W.I., Weld metal dilution effects in the metal arc welding of Al-Mg-Si alloys, *British Welding Journal*, 1955. 2: p. 93.

[74] Kou, S. and Y. H. Wang, Weld pool convection and its effect, *Welding Journal*, 1986, 65(3): p. 63-70.

[75] Chan, C.L., J. Mazumder and M.M. Chen, Effect of surface tension gradient driven convection in a laser melt pool: Three-dimensional perturbation model, *Journal of Applied Physics*, 1988. 64(11): p. 6166-6174.

[76] T. Debroy, in *Mathematical modelling of weld phenomina 2*, ed. H. Cerjak. The Institute of Materials, Cambridge, 1995, p. 3.

[77] C. Limmaneevichitr and S. Kou, Welding research supplement, May 2000, p. 126-135 and August 2000, p. 231-237.

[78] Chande, T. and J. Mazumder, Estimating effects of processing conditions and variable properties upon pool shape, cooling rates, and absorption coefficient in laser welding, *Journal of Applied Physics*, 1984. 56(7): p. 1981-1986.

[79] Chan, C.L., J. Mazumder and M.M. Chen, Effect of surface tension gradient driven convection in a laser melt pool: Three-dimensional perturbation model, *Journal of Applied Physics*, 1988. 64(11): p. 6166-6174.

[80] Babu. V, S. A. Korpela and N. Ramanan, Flow and temperature fields in a weld pool formed by a moving laser, *Journal of Applied Physics*, 1990. 9: p. 3990-3998.

[81] Picasso. M and A.F.A. Hoadley, The influence of convection in the laser cladding process, Numerical methods in thermal problems, 1991. 7(VII): p. 199-210.

[82] Grugel, R.N. and Y. Zhou, Primary dendrite spacing and the effect of off-axis heat flow, *Metallurgical Transactions*, 1989. 20 A: p. 969 - 972.

[83] Beckermann, C. and C.Y. Wang, Equiaxed dendritic solidification with convection: PartIII, *Metallurgical and Materials Transactions A*, 1996. 27: p. 2784-2795.

[84] Gao, J.W. and C.Y. Wang, An experimental investigation into the effects of grain transport on columnar to equiaxed transition during dendritic alloy solidification,

Journal of Heat transfert, 1999. 121: p. 430-437.

[85] Li, M., T. Mori and H. Iwasaki, Effect of solute convection on the primary arm spacings of Pb-Sn binary alloys during upward directional solidification, *Materials Science and engineering A*, 1999. 265: p. 217-223.

[86] Jean-Marie Drezet1, Sébastien Pellerin1, Cyrille Bezençon, Sélim Mokadem, Modelling the Marangoni convection in laser heat treatment, 2nd international conference Thermal Process Modelling and Computer Simulation, Nancy, Journal of Physics, 2003.

[87] D. Rosenthal. *Trans.Am.Soc.Metals,* 68:849, 1946.

[88] M.F. Ashby and K.E. Easterling, A first report on diagrams for grain growth in welds, *Acta Metall & Mater*, 30:1969 to 1978, 1982.

[89] J.C. Ion, K.E. Easterling, and M.F. Ashby, A second report on diagrams of microstructure and hardness for heat-affected zones in welds, *Acta Metallurgy*, 32, No. 11:1949–1962, 1984.

[90] Hunt. J. D, Steady state columnar and equiaxed growth of dendrites and eutectic, *Material Science and Engineering*, 1984, A65, 75–83.

[91] Boettinger, D. and Kurz, W. Solidification microstructures: recent developments, future directions. *Acta Mater*, 2000, 48, 43–70.